Universidad de Chile
Facultad de Ciencias Físicas y Matemáticas
Departamento de Ingeniería Civil

Nonlinear and nonhydrostatic dynamics of basin-scale waves in stratified rotating lakes

Tesis para optar al grado de Doctor en Ciencias de la Ingeniería Mención Fluidodinámica

Alberto Patricio de la Fuente Stranger

Profesores Guías:
Yarko Niño Campos

Miembros de la Comisión:
Jörg Imberger
José Rutllant Costa
Roman Stocker
Rodrigo Cienfuegos Carrasco
Claudio Falcón Beas

SANTIAGO DE CHILE
ENERO 2009

RESUMEN DE TESIS
PARA OPTAR AL GRADO DE DOCTOR EN CIENCIAS DE LA INGENIERÍA
POR: ALBERTO DE LA FUENTE STRANGER
FECHA: 30/01/2009
PROF. GUIA: YARKO NIÑO

Nonlinear and nonhydrostatic dynamics of basin-scale waves in stratified rotating lakes

A escala diaria, el viento es el principal agente externo que entrega la energía suficiente a un lago estratificado para generar el movimiento del fluido y mezclar la columna de agua. Bajo este escenario, la dinámica tridimensional del flujo puede ser correctamente representada mediante dos o más capas verticalmente acopladas, simplificación que ha permitido identificar una serie de fenómenos propios de flujos estratificados. Sin embargo, la característica multiescala de estos flujos limita su apropiada representación numérica o abstracción teórica, existiendo pocos trabajos científicos que abarquen toda la gama de escalas involucradas: desde las ondas de gran escala excitadas por el viento, hasta las pequeñas escalas dominadas por fenómenos nohidrostáticos.

El objetivo de esta tesis es investigar la evolución nolineal y nohidrostática de las ondas internas en lagos estratificados cuya dinámica está afectada por la rotación terrestre. El trabajo se centró en estudiar el flujo en dos capas de lagos estratificados, combinando resultados de modelos numéricos específicamente diseñados para esta tesis, con un enfoque pseudo-espectral y mediciones en terreno. Como primera medida se estudió el caso simplificado de una cubeta circular de fondo plano, para posteriormente estudiar la dinámica de un lago real, el Lago Constance ubicado en la frontera entre Suiza y Alemania, para el que se cuenta con una base de datos proveniente de cadenas de termistores y estaciones meteorológicas.

El análisis de la cubeta circular permitió identificar que la dinámica de cada una de las ondas continuamente forzadas por el viento puede asemejarse a un sistema oscilatorio de primer orden. La incorporación de los términos nolineales y nohidrostáticos eventualmente modifica esta dinámica oscilatoria, cuando la escala de tiempo de éstos es inferior a la escala de tiempo característica a la cual ocurren los intercambios de energía entre el cuerpo de agua y el viento. Adicionalmente, la manera en que evolucionan libremente las ondas de gran escala es dependiente de la onda en cuestión. Las ondas Kelvin evolucionan de igual forma a seiches en lagos pequeños, formándose un frente vertical donde las aceleraciones verticales dominan el flujo y excitan ondas tipo solitones pseudo-permanentes. Por el contrario, la evolución de la onda Poincaré está caracterizada por la radiación periódica de su energía hacia otros modos y su posterior restitución al modo original. Finalmente, la dinámica conjunta de las ondas Kelvin y Poincaré explica además, la excitación de ondas de menor escala.

Estas características generales fueron también identificadas en el estudio del Lago Constance, cuya dinámica está gobernada por la rotación terrestre y los fenómenos nolineales y nohidrostáticos. Se mostró que la principal onda excitada por el viento es la onda Kelvin, que evoluciona de igual forma a la descrita para la cubeta circular. Adicionalmente, se identificó que la interacción entre ondas Kelvin y Poincaré excita trenes de ondas que atraviesan todo el cuerpo de agua, y que la interacción entre ondas excitadas por el viento permite energizar las ondas topográficas o geostróficas, que no necesariamente son excitadas directamente por el viento.

Se concluye que la principal consecuencia de la dinámica nolineal y nohidrostática en lagos estratificados es que rompe con la coherencia espacial en toda la cubeta dada por procesos lineales, de manera que el flujo se caracteriza por la existencia de una serie de fenómenos locales de, por ejemplo, frentes verticales y alta velocidad del flujo. Consecuentemente, los fenómenos nolineales y nohidrostáticos fomentan localmente los procesos de mezcla vertical de la columna de agua, tales como: inestabilidades interfaciales dadas por altas velocidades del flujo y excitación de ondas nohidrostáticas de carácter permanente o cuasi-permanente que rompen al llegar a la orilla. Sin embargo, en términos de disipación de la energía, se postula a raíz de los resultados obtenidos en el lago Constance, que ésta se explica principalmente en la fricción con el fondo, la que responde también a aumentos localizados en la velocidad del flujo.

Summary

At a daily scale, wind is the main external agent that provides enough energy as to induce water flow and vertical mixing in stratified lakes. Under theses circumstances, the three-dimensional dynamics of the lake can be correctly represented through considering two or more vertically coupled layers, which has allowed for the identification of a wide range of phenomena that characterize stratified flows. However, the multiscale feature of these flows limits their numerical representation or theoretical abstraction, thus presently existing only few scientific works covering the whole range of scales involved, from the wind-excited waves down to the smaller nonhydrostatic scales.

The main objective of this thesis is to investigate the nonlinear and nonhydrostatic evolution of internal waves in stratified lakes whose dynamics is modified by Earth rotation. This work focused on studying the two-layer dynamics of stratified lakes, by combining simulations, carried out with numerical models developed for this research, with pseudo-spectral analysis and field measurements. First, the study of the simple case of a circular flat-bottom basin was conducted, and then the results were applied to study the dynamics of a real lake, Lake Constance, placed at the border between Switzerland and Germany, for which a data base coming from four LDS (thermistor chains and meteorological stations) is available.

The circular basin analysis showed that the wind-forced dynamics of each basin-scale wave could be represented as a first order oscillatory system. Inclusion of nonlinear and nonhydrostatic terms may modify this oscillatory behaviour, when the time scale of these terms is smaller than the time scale at which the surface energy exchange between the lake and the wind occurs. Furthermore, the free evolution of the basin-scale waves is dependent on the type of wave. Kelvin waves follow a quite similar dynamics than that of standing seiches in small lakes, forming a vertical front where the vertical accelerations dominate the flow, thus exciting quasi-permanent solitary-type waves. In contrast, Poincaré evolution showed the periodic back and forward radiation of the energy between the parent wave and other modes. Finally, the coupled Kelvin-Poincaré dynamics explained, also, the excitation of smaller waves.

These general features were also identified in Lake Constance, whose fluid dynamics is governed by the Earth rotation and nonlinear and nonhydrostatic phenomena. It was showed that Kelvin wave is the main wind-excited wave, evolving in the same way as that described for the circular basin. Furthermore, high-frequency wave trains that travel across the whole lake were related with the Kelvin-Poincaré interaction, and it was showed that the interaction between pairs of wind-excited waves energizes topographic or geostrophic waves, which are not necessarily directly excited by the wind. It is concluded that the nonlinear and nonhydrostatic dynamics breaks the whole basin coherence described for linear waves, so the flow is characterized by several localized events of, for instance, vertical fronts and high flow velocity. Consequently, nonlinear and nonhydrostatic dynamics also induces localized mixing events due to high shear and solitary-type wave excitation that finally breaks in the shore. However, in terms of energy, it is postulated that energy dissipation is mainly explained by bottom friction, which is also modified by local increases of the flow velocity.

Ctrl+Alt+Del

Agradecimientos (*Acknowledgments*)

El buen término de este doctorado se debe principalmente al apoyo económico de las siguientes instituciones: Facultad de Ciencias Físicas y Matemáticas, Universidad de Chile, a través de dos becas Facultad otorgada para los dos primeros años de estudio. Centro de Ecología Aplicada quienes me dieron las suficientes libertades para trabajar y estudiar durante los primeros años del doctorado. Ministerio de Educación, Gobierno de Chile, a través de la beca de término de doctorado MECESUP proyecto UCH-0310, para los dos últimos años de estudios, y la beca de pasantía por tres meses en Australia. A proyecto Fondecyt número 1080617. Centre for Water Research, University of Western Australia, a través de una beca para la extensión de mi pasantía por tres meses más en Australia, y la entrega gratuita de mediciones de terreno del Lago Constance. (*This PhD was economically supported by the following institutions: Facultad de Ciencias Físicas y Matemáticas, Universidad de Chile, under two scholarships for the first years. Centro de Ecología Aplicada, that gave me the freedom to simultaneously study and work during the fists years of my PhD. Project Fondecyt number 1080617. Ministerio de Educación, Gobierno de Chile, under the scholarship granted for the last two years of my PhD by MECESUP project UCH-0310, and funding to visit Australia. Centre for Water Research under funds granted for extending my visit to Australia, as well as Constance Lake field data.*)

Agradezco especialmente a mis profes guías, Yarko y Jörg, los que tuvieron la paciencia para aguantarme, guiarme y pelear contra mi spanglish. Me gustaría agradecer especialmente a Kenji, a quien rescato como el personaje que conocí durante el doctorado, ya que aprendí mucho de él como persona e investigador. Agradezco además, a los profesores de la comisión examinadora: José Rutllant, Roman Stocker, Rodrigo Cienfuegos y Claudio Falcón; así como también, a los revisores anónimos de los artículos sometidos a revistas científicas. (*I gratefully thanks to my advisors, Yarko and Jörg, for their patience when dealing with myself, guiding me and fighting against my spanglish. Particularly, I would like to thanks Kenji, who is "the one" that I meet during the PhD, since I learnt a lot from him as person and scientist. I would also thank to the evaluator commission: José Rutllant, Roman Stocker, Rodrigo Cienfuegos y Claudio Falcón; as well as the anonymous reviewers of scientific publications.*

Agradezco además a todos quienes me acompañaron durante este tiempo, tanto dentro del doctorado en la Facultad y en el Departamento de Ingeniería Civil, como en el CEA, Centre for Water Research de Australia, y Laboratoire Magma et Volcanes de Clermont-Ferrand.(*I would like to thank to all of my partners at the PhD program, the Civil Engineering Department, CEA, Centre for Water Research and Laboratoire Magma et Volcanes at Clermont-Ferrand*)

Agradezco a mis papás, hermano y hermanas, con quienes siempre ha sido un agrado juntarme a hablar tonteras y despegarme de las ecuaciones y modelos. Por último, agradezco enormemente a mi nueva familia Carolina. Gracias por todo.(*I also wish to thank to my parents, my brother and sisters, with whom it's always being a pleasure to talk nonsense, for unplugging myself from equations and models. Finally, I specially thank to my new family Carolina. Thanks a lot.*)

Salud (*Cheers*)

Beto

Contents

Introduction

An overview of lakes dynamics[†]

Lake dynamics is usually studied by considering closed reservoirs that exchange momentum and energy with the atmosphere, neglecting the contribution of inflows and outflows. In this context, the atmospheric timescales govern those of the lake dynamics, through heat and momentum exchanges at the surface of the lake, producing seasonal stratification, daily mixing events, and water circulation.

Heat exchanges at the surface of the lake depend on the latitude, being it possible to establish a first classification of lakes based on their location. In equatorial regions, solar radiation does not present important seasonal changes and tropical lakes are governed by the diurnal cycle without seasonal changes. As the latitude increases toward the poles, the average temperature decreases and the seasonal solar radiation produces thermal stratification of the water column in warm seasons, about 9 months per year, and well-mixed conditions during winter. Finally, at high latitudes where the average temperature is low and has large seasonal changes, thermal stratification occurs twice per year, in winter and in summer. In terms of the total energy of the lake, stratified conditions have less total potential energy than well-mixed conditions. This means that in order to induce the vertical mixing of the water column, that is, to increase the potential energy, additional external sources of energy are required: mechanic or caloric energy in winter stratified lakes, and only mechanic energy in summer stratified lakes, as the superficial heating tends to increase the vertical stratification of the water density.

Within daily timescales, exchanges of mechanical energy between the lake and the atmosphere govern the transport processes. For instance, the largest fraction of the wind mechanical energy is quickly dissipated at the surface layer, through surface wave generation, turbulence in the surface layer, and eventually, shear instabilities at the density interface that partially reverse the stratification; while the remaining small fraction of the wind energy interacts with the basin-scale waves, through work exchanges between the wind and average flow velocity in the surface layer. The energy transferred to the system is finally dissipated, as internal waves may trigger mixing events in the lake due to bottom and interfacial shear where the velocity gradients are large enough for the flow to become unstable, or through solitary-type waves generated from nonhydrostatic processes that finally break in shallow areas, dissipating their energy and inducing localized vertical mixing events. The excitation and degeneration of the basin-scale waves is a key issue to investigate in the field of lake dynamics, since it governs horizontal mass and heat redistributions after the wind recedes, and thus the ecological processes within the lake.

[†]Recommended literature: Mortimer (1952); Spigel & Imberger (1980); Imberger & Hamblin (1982); Imberger (1985); Monismith (1985); Imberger & Patterson (1990); Münnich *et al.* (1992); Wüest *et al.* (2000); Antenucci & Imberger (2001); Wüest & Lorke (2003); Shimizu *et al.* (2007).

A traditional approach for studying the excitation and degeneration of the basin-scale waves in lakes considers the vertical stratification as made up by several vertically averaged layers that interact with each other. For each layer in the inviscid approach, that is without internal mixing or friction, changes in the local, instantaneous layer thickness are due to the divergence of horizontal volumetric fluxes; and local changes in the horizontal momentum are due to momentum advection, Coriolis acceleration, horizontal pressure gradient, and the tilted interfaces that transfer vertical momentum (fluid pressure at the interfaces) to horizontal momentum.

The study of the linearized equations governing the dynamics of multilayer systems has provided sound explanations for the main horizontal mass and energy transport within stratified lakes, energy exchanges between the lake and the wind, and whole basin energy damping given by bottom friction. On the other hand, studies that have focused on nonlinear and nonhydrostatic analyses of simple cases have established the key features that govern the flow in smaller scales of two-layer stratified flows characterized by the buoyancy frequency. However, no previous studies have analyzed the nonlinear dynamics of the basin-scale waves in rotating lakes in order to understand energy transfer among the different scales of the flow down to the smaller scales of stratified flows locked at the buoyancy frequency. This is the main overarching theme of this thesis.

Objectives

The main objective of this thesis was to investigate the nonlinear and nonhydrostatic evolution, excitation and degeneration of basin-scale waves in rotating two-layer lakes. With this aim, two specific objectives were defined:

1. To investigate, with the help of mathematical and numerical models, the evolution of basin-scale waves in circular, flat bottom, rotating basins. The aim is to identify the main processes involved in the evolution of basin-scale waves in rotating basins, and the influence of the earth rotation timescale and the nonlinear processes timescale, with respect to the inherent timescale of the lake.

2. To investigate, with the help of mathematical and numerical models and field data, the evolution of basin scale waves in actual lakes. The aim is to define whether the analysis for circular basins explains the nonlinear and nonhydrostatic dynamics of actual wind-forced lakes. Lake Constance was chosen for this purpose. This lake is located at the border between Germany and Switzerland and a database coming from four LDS (Lake Diagnostic System: thermistor chains and meteorological stations deployed in the lake) is available. Field data was donated for this thesis by the Centre for Water Research. Field measurements were used to validate two-layer models that describe the nonlinear interaction between the basin-scale waves and the nonlinear and nonhydrostatic dynamics of the flow.

To carry out the research needed to accomplish the declared objectives, two numerical models were developed for this thesis:

3 The model *by n-layers* and its reduced version *b2l* for the two-layer dynamics. This model is able to represent multilayer, nonlinear and weakly nonhydrostatic processes in stratified lakes. Particularly, the reduced version *b2l* is also able to solve the two-layer governing equations in a very large numerical mesh, in a reasonable computational time (10% of the real time), with small numerical diffusion (about 3% of the total energy per day).

4 The model *LinMod* for solving the nonlinear interaction among basin-scale waves in Lake Constance.

Outline

This document is based on two scientific articles, one already published in Limnology and Oceanography (2008, **53**: 2738 - 2748), and the other one under consideration in the same journal. Each publication represents a particular chapter of this thesis. The numerical model is described in the two appendixes that contain information about the models published in different international conferences.

In Chapter 2, the evolution of basin scale waves in circular, flat bottom, rotating basins is discussed; the analysis is centred in identifying the nonlinear and weakly nonhydrostatic processes that govern the evolution of basin-scale waves in a simple-shape basin, for which the analytic solution of the linear problem is available. In order to generalise the results presented in Chapter 2, three dimensionless numbers were used to describe the flow: the Wedderburn number, Burger number and the steepening formation time. The first dimensionless number defines how intense the wind is with respect to the lake. The second dimensionless number defines the relative importance of the Earth rotation on the internal basin-scale waves. Finally, the third dimensionless number characterizes the time when the dynamics becomes nonlinear, with respect to the internal basin-scale waves timescale. In Chapter 3 the key features identified in Chapter 2 are discussed in the case of a real lake. Lake Constance was chosen, because both Earth rotation as well as nonlinear processes govern the basin-scale dynamics of this lake. Besides validating with field measurements the flow dynamics identified in Chapter 2, the interpretation of field measurements under the optics of the numerical results, forced the reanalysis of the energy path in stratified rotating lakes established in the previous chapter, suggesting that, even for a highly nonlinear flow, the energy dissipation in the lake is mainly due to bottom friction, while nonlinearities of the flow induce mostly localized vertical mixing and rather small energy dissipation compared with the corresponding input from the wind.

Finally, in Chapter 4 the main results and conclusions are summarized.

References

Antenucci, J. & Imberger, J. 2001 Energetics of long internal gravity waves in large lakes. *Limnol. Oceanogr.* **46**, 1760 – 1773.

Imberger, J. 1985 The diurnal mixed layer. *Limnol. Oceanogr.* **30**, 737 – 770.

Imberger, J. & Hamblin, P. 1982 Dynamics of lakes, reservoirs, and cooling ponds. *Annu. Rev. Fluid Mech.* **14**, 153 – 187.

Imberger, J. & Patterson, J. 1990 Physical limnology. *Adv. Appl. Mech.* **27**, 303–475.

Monismith, S.G. 1985 Wind-forced motion in stratified lakes and their effect on mixed-layer shear. *Limnol. Oceanogr.* **30**, 771 – 783.

Mortimer, C.H. 1952 Water movement in lakes during summer stratification; evidence from the distribution of temperature in windermere. *Phil. Trans. R. Soc. Lond. B* **236**, 355 – 398.

Münnich, M, Wüest, A. & Imboden, D.M. 1992 Observations of the second vertical mode of the internal seiche in an alpine lake. *Limnol. Oceanogr.* **37**, 1705 – 1719.

Shimizu, K., Imberger, J. & Kumagai, M. 2007 Horizontal structure and excitation of primary motion in a strongly stratified lake. *Limnol. Oceanogr.* **52**, 2641 – 2655.

Spigel, R. & Imberger, J. 1980 The classification of mixed-layer dynamics in lakes of small to medium size. *J. Phys. Oceanogr.* **10**, 1104 – 1121.

Wüest, A. & Lorke, A. 2003 Small-scale hydrodynamics in lakes. *Annu. Rev. Fluid Mech.* **35**, 373–412.

Wüest, A., Piepke, G. & Van Senden, D. 2000 Turbulent kinetic energy balance as a tool for estimating vertical diffusivity in wind-forced stratified waters. *Limnol. Oceanogr.* **45**, 1388 – 1400.

The evolution of internal waves in a rotating, stratified, circular basin and the influence of weakly nonlinear and nonhydrostatic accelerations[†]

Abstract

The evolution of internal waves in a two-layer rotating circular lake was studied under nonlinear and weak nonhydrostatic effects. Inclusion of nonlinear acceleration allowed the waves to steepen at the rear of the crest in deep lakes, forming a front with time. The nonhydrostatic acceleration is shown to counteract this wave steeping, leading to wave dispersion and when the two effects are in balance, solitary-type waves may form. It is shown that a Kelvin wave evolves by imparting energy primarily to sub-modes of the parent cyclonic wave by steepening and to solitary-type waves. By contrast, a Poincaré wave is shown to evolve without shedding much of its energy to other waves, and only a small fraction of the wave energy goes to other sub-modes and this is not lost from the parent wave, but rather is periodically transferred back into the parent wave. When both Kelvin and Poincaré waves were present simultaneously in the water body, then an interaction was observed, when both waves were in phase, which gave rise to additional wave components.

Introduction

A common conceptual model, used to study motion in stratified lakes (Fischer *et al.*, 1979), is to simplify the stratification into two, three, or more layers; this provides a good approximation to the basin-scale internal waves modes up to the number of fluid layers (Mortimer, 1952; Monismith, 1985; Münnich *et al.*, 1992). With this assumption, the energy imparted by the wind enters the surface layer and is then progressively distributed into the layers below as the baroclinic pressure field sets up motions in the lower layers (Imberger, 1998; Wüest & Lorke, 2003).

The interfacial response due to a surface shear stress, in a non-rotating water body, was described by Spigel & Imberger (1980), who extended the earlier analytic solution developed by Heaps & Ramsbottom (1966). These authors showed that, along the fetch, the steady state equilibrium could be described by a constant interfacial slope $\partial_x \eta_2 = \bar{h}_1 (LW)^{-1}$, where the minus sign was attached as the slope is in the opposite direction to the imposed wind stress and η_2 is the interfacial displacement with respect to the unforced equilibrium, L is

[†]de la Fuente, A., Shimizu, K., Imberger, J. and Niño, Y. 2008. The evolution of internal waves in a rotating, stratified, circular basin and the influence of weakly nonlinear and nonhydrostatic accelerations. *Limnol. Oceanogr.* **53**: 2738 - 2748

the length of the basin, $\bar{h}_1$ is the equilibrium top layer thickness, ∂_x is the partial differential operator with respect to x, and:

$$W = \frac{g'\bar{h}_1^2}{u_*^2 L}, \tag{1.1}$$

is the Wedderburn number. In Eq. 1.1, $g' = g(\rho_2 - \rho_1)\rho_o^{-1}$ is the reduced gravity, ρ_1 and ρ_2 are the layer densities, ρ_o is the reference density, g is the acceleration due to gravity and u_* is the shear velocity at the water surface. From this it follows immediately that the maximum non-dimensional displacement ($\eta_{2max}/\bar{h}_1$), is equal to $(2W)^{-1}$; $W = 0.5$ is thus the condition for full upwelling of the bottom water (Thompson & Imberger, 1980; Imberger & Hamblin, 1982). The interfacial set up is achieved via internal waves initiated at both the upwind and downwind boundaries propagating towards the interior, arriving at the centre of the lake one quarter of an internal period T_i later (Mortimer, 1952; Spigel & Imberger, 1980):

$$T_i = \frac{2L}{c_o}, \tag{1.2}$$

where

$$c_o = \sqrt{g'\frac{\bar{h}_1\bar{h}_2}{\bar{h}_1 + \bar{h}_2}} \tag{1.3}$$

is the internal wave celerity and $\bar{h}_2$ is the equilibrium bottom layer thickness (Mortimer, 1952). Under the linear theory assumption, these waves keep propagating back and forth across the length of the lake with a period T_i. For motions initiated from an initial interface displacement, it is convenient to define the Wedderburn number by: (Horn *et al.*, 2001)

$$W = \frac{\bar{h}_1}{2\eta_o} \tag{1.4}$$

where η_o is the initial maximum displacement.

For a lake that is large enough so that the time a wave takes to propagate across the basin ($T_i/2$), is similar to or longer than the time it takes for the lake to turn through $360^o(2f)^{-1}$ (f is the Coriolis parmeter), the waves will obviously be strongly influenced by the Earth's rotation; the ratio of these two times is generally known as the Burger Number (Gill, 1982; Antenucci *et al.*, 2000):

$$S = \frac{4}{fT_i}. \tag{1.5}$$

Two major classes of waves are possible for such rotating basins. First, Kelvin or cyclonic waves, where the force balance in the direction of propagation remains the same as for non-rotating waves; the motion is essentially unidirectional and the Coriolis acceleration, induced by this unidirectional motion, is balanced by an oscillating transverse pressure gradient. Second, Poincaré or anticyclonic waves, where the Coriolis acceleration induces a motion normal to the pressure gradient, which causes anticyclonic rotation of the interface displacement and fluid velocity with nearly circular particle paths. For a particular basin geometry, horizontal modes may be decomposed into multiple fundamental modes oscillating in harmony side by side (Gómez-Giraldo *et al.*, 2006); in simple terms those modes are excited that match the spatial and temporal distribution of the imposed wind stress (Csanady, 1973; Gómez-Giraldo *et al.*, 2006; Shimizu *et al.*, 2007).

The influence of the nonlinear inertia acceleration has been investigated, in some detail, in the absence of rotation. Advective acceleration leads to steepening of an initial basin-scale wave (Ripa, 1982; Horn *et al.*, 2001; Boegman *et al.*, 2005*a*) over a characteristic time T_s, defined by Horn *et al.* (2001) as

$$T_s = \frac{L}{\alpha \eta_o}, \tag{1.6}$$

where

$$\alpha = \frac{3}{2} c_o \frac{\bar{h}_2 - \bar{h}_1}{\bar{h}_1 \bar{h}_2}. \tag{1.7}$$

Steepening is followed by convective overturning (Fedorov & Melville, 1995) and degeneration into solitons (Grimshaw *et al.*, 1998; Horn *et al.*, 2001; Boegman *et al.*, 2003). The nonlinear acceleration also causes transfer of energy to higher basin-scale modes (Maxworthy, 1984; Melville *et al.*, 1989; Fedorov & Melville, 2000) and energy transfers to and from background currents (Clark & Imberger, 1996; Riley & Lelong, 2000).

Studies in an infinite domain have not shown whether waves of permanent form, such as solitons in non-rotating case, exist for the rotating case (Grimshaw *et al.*, 1998; Helfrich, 2007). Periodic growth of solitary-type waves and their subsequent destruction in a rotating stratified fluid have been discussed by Grimshaw *et al.* (1998) and Helfrich (2007). Previously, steepening of Kelvin waves in a rotating straight channel had been shown by Bennett (1973) and Fedorov & Melville (1995) and Renouard *et al.* (1986) had also demonstrated the formation of solitary-type waves with a stable longitudinal shape described by a $sech^2$ profile.

However, the degeneration of basin-scale waves in a rotating enclosed basin does not appear to have been investigated.

The main objective of the present study is to improve the understanding of the nonlinear steepening and nonhydrostatic wave dispersion on the propagation of basin-scale internal waves in a two-layer, stratified, rotating enclosed circular basin. A circular basin was chosen as analytic solutions for the linear regime are available. The characteristic numbers, such as W, T_i, S, and T_s, are combined to provide a parameter space in which to discuss the analytical and numerical results for the cases of a spatially uniform, suddenly-imposed wind forcing and the free evolution of the Kelvin and/or Poincaré waves.

The paper is organized as follows. First, the analytic solution for a circular basin with a two-layer stratification, re-derived by Stocker & Imberger (2003), is revisited in order to understand the general features of the solution and to display scaling that captures the motion. Then, the n-layer model, used in this study, (de la Fuente *et al.*, 2006) (Appendix A) is briefly described. This is followed by the derivation of the solution for a suddenly imposed wind on an n-layer fluid in a circular basin and the free evolution from initial interface displacement. The condition that defines the formation of solitary-type waves and transfer of energy from initial basin-scale waves to sub-modes and solitary-type waves is then presented.

Linear approximation and scaling

Modal decomposition of the linear momentum and mass equations for an n-layer system, in a rotational frame of reference reduce to a set of n-linear, independent vertical modal equations, the solution of which are described by equations equivalent to the shallow water equations for a homogeneous basin (Csanady, 1968; Monismith, 1985; Antenucci & Imberger, 2001). For a circular homogeneous basin with a two-layer stratification, forced by a suddenly-imposed, spatially uniform shear stress, Stocker & Imberger (2003) showed that the flow velocities and vertical displacements of the interface were linear functions of the inverse of the Wedderburn number. Therefore, it is advantageous to scale the vertical interfacial displacements η_2 and layer-averaged horizontal velocities u_i so that:

$$\eta_2^* = 2W\frac{\eta_2}{\bar{h}_1} \quad ; \quad u_i^* = 2W\frac{u_i}{c_o} \tag{1.8}$$

where the star denotes non-dimensional variables, W is the Wedderburn number with $L = 2r_o$ for circular basins (Eq. 1.1), and the radius and time are non-dimensionalized with respect to the radius of the basin r_o and the internal wave period T_i (Eq. 1.2 with $L = 2r_o$). This scaling allows the forcing to be removed from the equations leaving only the Burger Number and the ratios of layer thicknesses as parameters.

The maximum interfacial displacements were computed using this analytic solution for different values of S and the time t^* and this is shown in **Fig. 1.1**. When the Burger number S is

large, both the Kelvin and Poincaré waves have the same wave shape and angular frequency, but they rotate in opposite directions. Superposition of such matching waves, results in a fundamental standing internal wave mode, as previously discovered by Antenucci & Imberger (2001)Antenucci and Imberger (2001); the maximum displacements are produced first at $t^* = 0.42T_i$, when the radial Kelvin and Poincaré waves are in phase for the first time; this occurs periodically every $0.84T_i$. For medium rotation ($S \approx 0.5$), Kelvin and Poincaré waves have similar amplitudes and still produce the first local maximum when they become in phase at about $t = T_i/2$ (see **Fig. 1.1**); however, this maximum displacement does not occur at the upwind end because the troughs of the two waves are displaced progressively as S decreases due to the difference of their natural periods. In the limit of small Burger numbers, the Kelvin wave dominates the response and the timescales of the problems given by the period of the fundamental mode Kelvin wave, T_k, which can easily been computed using the polynomial fit presented by Antenucci & Imberger (2001). For winds that have a duration longer than T_i or T_k, the amplitudes show a periodic behavior with maximum amplitudes itself oscillating because natural angular frequencies of the modes do not occur in multiples of the fundamental mode frequency.

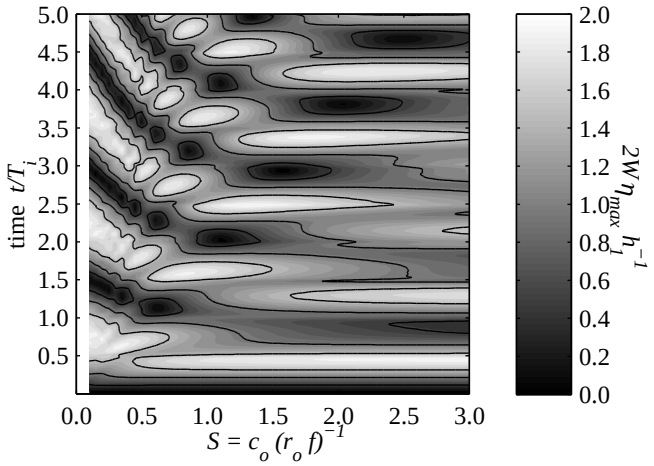

Figure 1.1: Maximum interfacial displacement as a function of the time and Burger number (S). The displacement was non-dimensionalized as in Eq. 1.8 and the time by the internal period T_i.

In **Fig. 1.2**, we show the total non-dimensional energy of all the wave components, partitioned into kinetic and available potential energy and work done by wind. The non-dimensionalization used for the different energy bins was derived from the scaling introduced in Eq. 1.8 such that:

$$TKE^* = \frac{2W}{c_o \rho_o u_*^2 \Omega L} TKE, \quad TPE^* = \frac{2W}{c_o \rho_o u_*^2 \Omega L} TPE, \quad TE^* = \frac{2W}{c_o \rho_o u_*^2 \Omega L} TE \tag{1.9a}$$

$$Work^* = \frac{2W}{c_o \rho_o u_*^2} \int_\Omega \vec{\tau}_s \cdot \vec{u}_1 \, d\Omega \tag{1.9b}$$

where TKE^*, TPE^*, and TE^* are respectively the kinetic, available potential, and total energy integrated over the basin, $Work^*$ is the work done by wind over the surface, and Ω is the surface area.

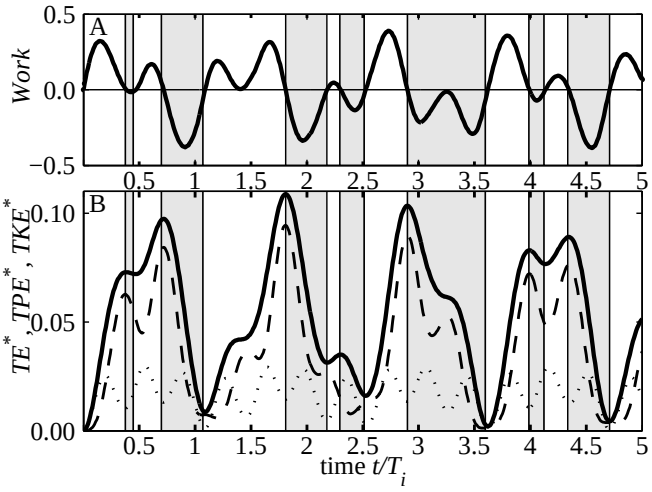

Figure 1.2: (A) Time series of non-dimensional surface rate of work by or to the wind. (B) The non-dimensionl total energy of lake, TE^* (solid line), and its partitioning between total kinetic energy, TKE^*, and total available potential energy, TPE^* (dotted and dashed lines, respectively) for $S = 0.5$. Shaded areas show periods when wind takes energy from the lake. The rate of working and energies were non-dimensionlized as in Eq. 1.9

For wind durations shorter than $T_i/2$ or $T_k/2$, the wind does work on the lake, exciting the internal waves. The supplied energy is primarily transferred to available potential energy (about 75% of the total energy for weak rotation and 50% for strong rotation). On the other hand, during the second half of the period, the existing waves do work on the wind, because the direction of the wind now opposes that of the surface velocity associated with the wave. The wind thus periodically energizes and cancels the internal seiches. The transfer to available potential energy is less efficient under strong rotation as the solution, for that limit, is a pure Kelvin wave, which has an equi-partitioning between kinetic and available potential energy, whereas in the limit of weak rotation, the solution approaches that for a non-rotating internal seiche that has the property that the energy is maximum when all the energy is either all potential or all kinetic energy.

Governing equations and numerical scheme

The standard shallow water equations with the Boussinesq approximation and with the assumption of hydrostatic pressure may be derived for an n-layer stratification by vertically integrating the full equations of motion between $z = z_{i+1}$ to z_i, where z is the vertical coordinate, and z_{i+1} and z_i correspond to the bottom and upper interfaces that define the ith layer (Baines, 1998). The three governing equations, for each layer, may be written as:

$$\frac{\partial U_i}{\partial t} + \frac{\partial F_i^x}{\partial x} + \frac{\partial F_i^y}{\partial y} = H_i \tag{1.10}$$

where

$$U_i = [h_i, u_i h_i, v_i h_i]^T \tag{1.11a}$$

$$F_i^x = \begin{pmatrix} u_i h_i \\ u_i u_i h_i \\ u_i v_i h_i \end{pmatrix} \quad , \quad F_i^y = \begin{pmatrix} v_i h_i \\ v_i u_i h_i \\ v_i v_i h_i \end{pmatrix}, \tag{1.11b}$$

and

$$H_i = \begin{pmatrix} 0 \\ -h_i g \sum_{j=1}^{i} \epsilon_j \frac{\partial z_j}{\partial x} + \frac{\tau_i^x}{\rho_o} - \frac{\tau_{i+1}^x}{\rho_o} + f v_i h_i \\ -h_i g \sum_{j=1}^{i} \epsilon_j \frac{\partial z_j}{\partial y} + \frac{\tau_i^y}{\rho_o} - \frac{\tau_{i+1}^y}{\rho_o} - f u_i h_i \end{pmatrix}, \tag{1.11c}$$

where ρ_i, u_i, and v_i are the layer-averaged density and velocities in x and y directions, respectively, τ_i^x and τ_{i+1}^x are the upper and bottom interfacial shear stresses in the x direction, and $\rho_o \epsilon_i = (\rho_i - \rho_{i-1})$ for $i > 1$ and $\rho_o \epsilon_1 = \rho_1$ for $i = 1$.

These equations were solved using the MUSCL-Hancock method for hyperbolic equations of an n-layer system (Bradford *et al.*, 1997; Loose *et al.*, 2005) (see Appendix B for the details). Benchmarks that validate the numerical scheme were presented by de la Fuente *et al.* (2006) (Appendix A). As the equations assume an inviscid fluid, shear stresses were only considered at the water surface and at the side walls it was assumed that no fluid crosses, but slip was allowed.

The weak nonhydrostatic effects were included using the model proposed by Brandt *et al.* (1997), who kept the terms of the order $\mu^2 = h^2 L^{-2}$, but neglected the terms of the order $\epsilon = a h^{-1}$, where a is the wave amplitude scale and h and L are the layer thickness and basin scale, respectively. With this simplification, the nonhydrostatic terms in the momentum equations for each layer may be included as follows:

$$\frac{\partial \vec{u}_i h_i}{\partial t} = B_i \nabla \left(\frac{\partial}{\partial t} \left(\nabla \cdot \vec{u}_i h_i \right) \right) + A, \tag{1.12}$$

where

$$B_i = \begin{cases} \frac{h_1^2}{6} & i = 1 \\ \frac{h_2^2}{3} + \frac{h_1 h_2}{2} & i = 2 \end{cases}, \tag{1.13}$$

and A is the vector containing all the F_i and H_i terms of (1.11a)B-C. The nonhydrostatic terms of (1.12) were solved numerically using the method described in the Appendix B. The above approximation includes the assumption that h_1 and h_2 are constant in the conservation of volume calculations ((1.12)) (Tomasson & Melville, 1992). However, as explained in the Appendix B, the final scheme adopted here uses $h_i + \eta$ in place of h_i, as it simplified the numerical scheme. The model results were then compared to the experimental data from Horn *et al.* (2001) for waves steeping in a non-rotating rectangular channel; the model successfully reproduced the essential features such as number and shape of solitary waves, and timing of their emergence (**Fig. 1.3**). Although the amplitudes of solitary waves and the propagation velocity showed some deviations from the experimental data due to neglect of viscous damping (Horn *et al.*, 2002), they do not pose severe limitations for our analyses as we focus on the inviscid dynamics.

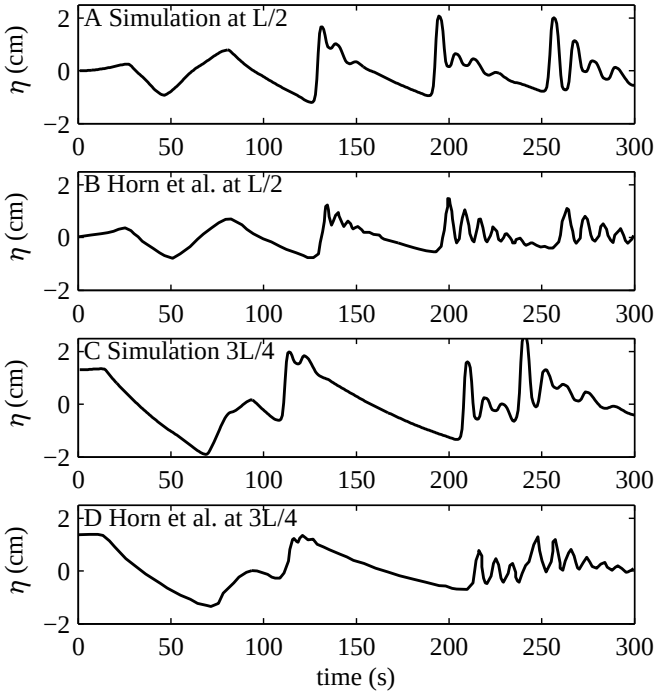

Figure 1.3: Comparison of interfacial displacement between simulation and experimental results in a two-layer, non-rotating channel of length L. (A, C) Simulations, and (B, D) experiments by Horn *et al.* (2001). The waves were generated by initial linear tilt and resulting interfacial displacement was measured at $L/2$ and $3L/4$.

Interaction of internal waves and the imposed wind stress forcing the motion

The model, once validated, was applied to the case of a suddenly imposed wind over a circular basin containing a two-layer stratification. The effects of the weak nonlinearity and the inclusion of weak nonhydrostatic accelerations may be seen in **Fig. 1.4**, where this model

solution is compared to the linear solution for the case $S = 0.5$, $W = g'\bar{h}_1^2(u_*^2 2r_o)^{-1} = 1.83$, and $\bar{h}_1/\bar{h}_2 = 1.0$; the forcing was strong enough to induce nearly full upwelling at the first overshoot at $t \sim T_i/2$. The trend of the kinetic, available potential, and total energy were similar to the linear solution, although the non-linearities allowed the wind to impart slight more total energy to the motion (**Fig. 1.4A**) which is also reflected in the non-dimensional interface displacement; energy losses, due to numerical dissipation, were found to be less than 10% of the total energy, for the duration of the simulation (**Fig. 1.4A**). Throughout this paper we assume that the kinetic energy due to the vertical velocity is two orders of magnitude smaller than the potential energy plus kinetic energy due to horizontal velocities, and may thus be neglected.

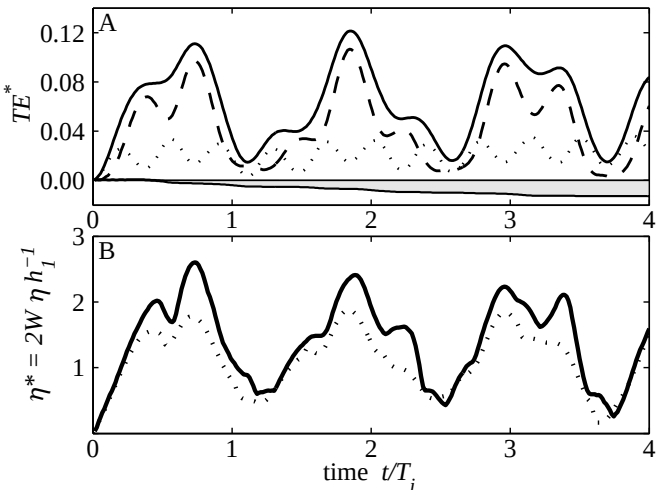

Figure 1.4: Comparison between simulation and analytic results for $S = 0.5$, $W = 2.3$ and $\bar{h}_1 = \bar{h}_2$. (A) Time series for the total energy and its partitioning between kinetic and available potential energies. Shaded area shows the estimated numerical dissipation of the simulation. (B) Linear (solid line) and nonlinear (dotted line) time series of the maximum interfacial displacement.

The well-known effect of the layer depth ratio on the nonlinear steepening (Horn *et al.*, 2001) is shown in **Fig. 1.5** where the interfacial displacements, at the upwind end and at the centre of the basin, are shown for the depth ratio $\bar{h}_1/\bar{h}_2 = 1.0$ and $\bar{h}_1/\bar{h}_2 = 0.1$, and the same Burger and Wedderburn numbers as before. When the layer thicknesses were equal, the inclusion of the non-linear and nonhydrostatic terms amplified the interfacial displacements, compared to those from the linear solution, almost symmetrically. However, for the small depth ratio, $\bar{h}_1/\bar{h}_2 = 0.1$, the waves steepened more at the rear of the crest (Choi & Camassa, 1999). Further, at the centre for the basin, an almost stationary interface oscillation was observed to appear with a period of about $T_i/3$, (**Fig. 1.5B**); the amplitude of this displacement was much less for simulation with $\bar{h}_1/\bar{h}_2 = 1.0$ than for $\bar{h}_1/\bar{h}_2 = 0.1$.

The expected generation of solitary-type waves, due to steepening of the Kelvin wave, is not observed seen in **Fig. 1.5A**; the interaction between the wind and the waves modulated the total energy as discussed above. The steepening timescale, Eq. 1.6, defines when the nonlinear effects become important for free oscillations with constant energy in time (Horn *et al.*,

2001)(Horn et al. 2001). The suddenly imposed wind problem analysed here, however, imposes temporal changes of the total energy with the timescale characterized by T_i or $T > k$. The ratio between these two timescales:

$$\frac{T_s}{T_i} = \frac{1}{3\eta_o}\frac{\bar{h}_1\bar{h}_2}{\bar{h}_2 - \bar{h}_1}, \tag{1.14}$$

should indicate whether there is enough time to produce steepening before the energy available for steepening is extracted by the wind. To test this hypothesis, simulations were carried out for $S = 0.5$ and $T_s/T_i = 0.40$, 0.48, 0.88, and 1.29 and the results are shown in **Fig. 1.6**. The first case considers $\bar{h}_1/\bar{h}_2 = 0.05$ and $W = 1.83$, the second and fourth cases were run with $\bar{h}_1/\bar{h}_2 = 0.1$ and $W = 1.83$ and 3.66, respectively, while the third case was conducted with $W = 1.83$ and $\bar{h}_1/\bar{h}_2 = 0.55$. In order to calculate T_s/T_i, η_o was taken as the maximum interfacial displacement at $t \approx T_i/2$. Note that the smaller ratios T_s/T_i are closer to the smaller possible value of 0.3 for the limit $\bar{h}_1 << \bar{h}_2$ and $\eta_o \to \bar{h}_1$. **Fig. 1.6H** shows the total energy as a function of time, indicating three maxima at approximately $t/T_i = 0.75$, 1.8 and 2.9, respectively.

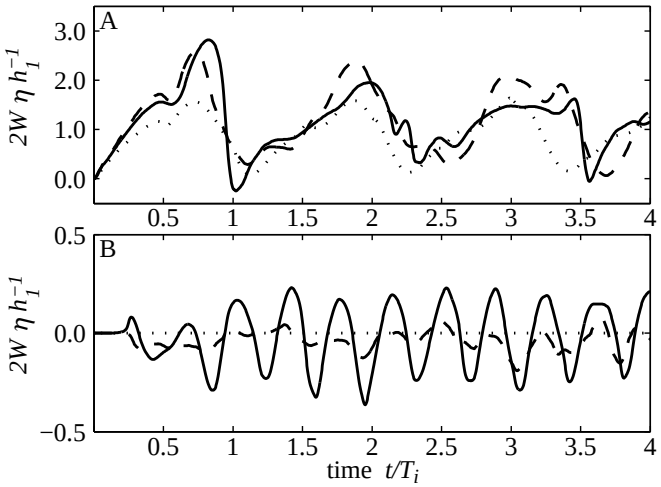

Figure 1.5: Time series of non-dimensional interfacial displacement for linear case (dotted line), and nonlinear and weak nonhydrostatic cases for $\bar{h}_1/\bar{h}_2 = 1$ (dashed line) and $\bar{h}_1/\bar{h}_2 = 0.1$ (solid line). (A) At the upwind end and (B) at the center of the basin. $S = 0.5$ and $W = 1.83$.

The three runs where $T_s < T_i$ (darkest lines) show steepening of the rotating internal waves that were modulated by energy extraction by the wind. The results for $T_s/T_i = 0.40$ and 0.48 (dotted and dashed lines) show the energy peaking after the second maximum in total energy (**Fig. 1.6E**), but this recedes as the wind drains the energy from the basin-scale wave before solitary-type waves can form (**Fig. 1.6F**). The magnitude of the steepening in **Fig. 1.6E** is larger for $T_s/T_i = 0.40$ than $T_s/T_i = 0.48$. A similar behaviour was observed for $T_s/T_i = 0.88$ (solid dark line), while the results for $T_s > T_i$ (light solid line) did not show any steepening at all.

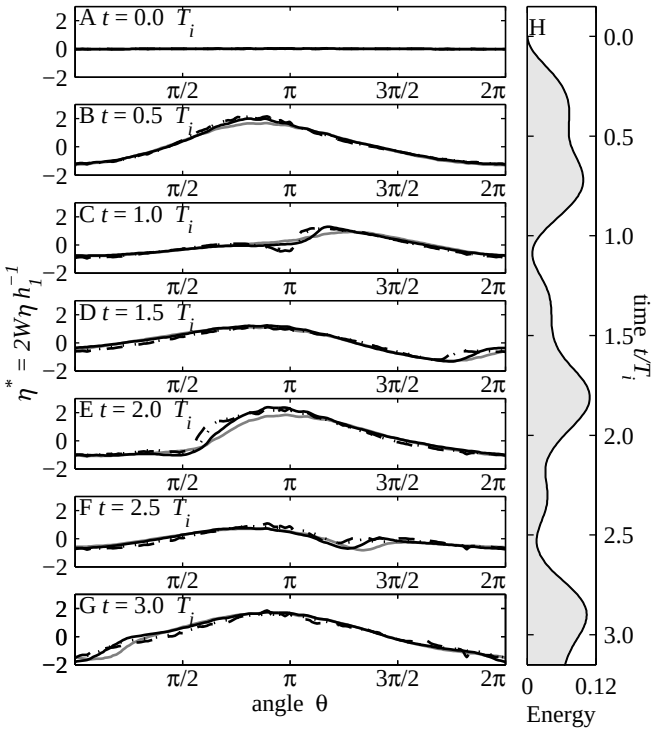

Figure 1.6: (A-G) Azimuthal profiles of the interfacial displacement for simulations of the spatially uniform suddenly imposed wind problem in a circular basin for ratios $T_s/T_i = 0.40$, 0.48, 0.88 (dashed, dotted and solid dark lines, respectively), and 1.29 (light solid line) from $t = 0$ to $t = 3T_i$ with $0.5T_i$ interval. (H) The time series of the total energy shown in **Fig. 1.2**, oriented along the vertical direction from top ($t = 0$) to bottom ($t = 3T_i$).

Free evolution of individual Kelvin and Poincaré waves

The evolution of the monochromatic Kelvin and Poincaré wave was also analysed with the model by initialising the simulations using the velocity and displacement field from the linear solutions (Eq. 1.12). The interface displacements from simulations for the initial Kelvin wave case, with an amplitude equivalent to a Wedderburn number $W = \bar{h}_1(2\eta_o)^{-1} = 0.6$, $\bar{h}_1/\bar{h}_2$, three Burger numbers are shown in **Figs. 1.7** and **1.8**. The steepening of the rear of the crest of the linear wave commences at approximately $t = T_s$ ($t' = 1.0$); degeneration into a train of solitary-type waves followed shortly after this time in all the cases. When the nonhydrostatic term was switched off, the initial basin-scale wave kept steepening until it formed a steep front, confirming the well-known fact that the formation of solitary-type waves requires the pressure dispersion term (**Figs. 1.8A** and **1.8B**). For a given value of S, the following features, similar to solitary waves in non-rotating flows (Grimshaw *et al.*, 1998; Ostrovsky & Stepanyants, 2005; Helfrich & Melville, 2006) were used to identified the presence of the solitary-type waves: (1) The azimuthal scale (wave length) increased with the Wedderburn number, as in non-rotating cases where larger solitons have shorter wave lengths (compare for example, **Fig. 1.8A**, **C**, and **E**). (2) The azimuthal shape of the solitary-type waves closely follows the $sech^2$ profile for smaller ratios $\bar{h}_1/\bar{h}_2$, but turned into

tanh profiles for relatively deeper surface layers (e.g., compare solid and dashed lines in **Fig. 1.8B** with $sech^2$ and *tanh* profiles in **Fig. 1.8B**, respectively). This is well-known and follows when higher order terms are included in the KdV equation (Lee & Beardsley, 1974; Ostrovsky & Stepanyants, 2005; Helfrich & Melville, 2006). (3) As is known from KdV theory, when the second order terms are included (Lee & Beardsley, 1974), the amplitude is limited leading to a maximum amplitude. This amplitude is proportional to the magnitude of the initial perturbation and is a function of (**Fig. 1.8G**). Note that, although these waves are not true solitons described by the permanent $sech^2$ shape, they retained their form over simulated time ($3T_s$), large compared to the travel time across a lake, and they may break at the coast and dissipate the energy.

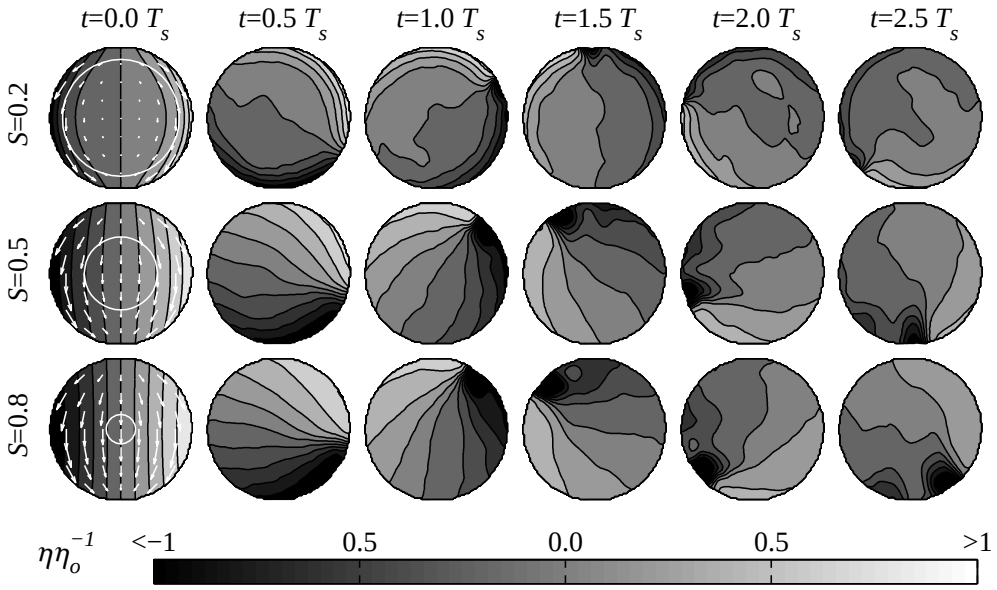

Figure 1.7: Evolution of the interfacial displacement with the nonhydrostatic terms for an initial monochromatic Kelvin wave for $W = \bar{h}_1(2\eta_o)^{-1} = 0.6$. White circle on initial conditions shows the Rossby radius measured from the shore, and white arrows are the layer-averaged velocity in the upper layer. The waves rotate anti-clockwise, as in the northern hemisphere. $t' = t/T_s$.

On the other hand, the results differed from the non-rotating case as the effects of the Earth's rotation modified the maximum amplitude of these solitary-type waves (**Fig. 1.8G**), where smaller S (strong rotation) is associated with smaller amplitudes.

Interestingly, the evolution of an initial Poincaré wave showed significant difference from the Kelvin wave cases (**Fig. 1.9**). Nonlinear steepening produced fronts steeper than those for the Kelvin wave. However, this did not lead to subsequent degeneration into solitary-type waves as described for the Kelvin waves (compare **Figs. 1.7** and **1.9**). The fronts appeared and disappeared periodically, which modulated the wave structure but did not change the amplitude and basic structure of the initial Poincaré wave significantly (see subsequent section). The inclusion of the nonlinear terms was necessary for the steepening, but the results were almost insensitive to the inclusion of the nonhydrostatic term.

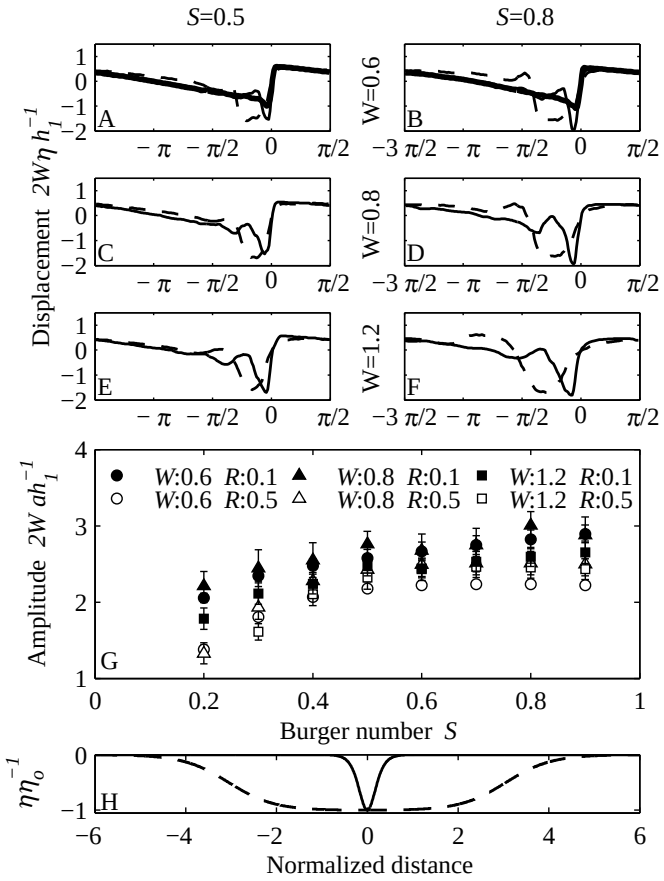

Figure 1.8: (A-F) The azimuthal profiles of the interfacial displacement at $t = 1.5$ and $r = r_o$ for $W = \bar{h}_1(2\eta_o)^{-1} = 0.6$, 0.8 and 1.2, and ratio $\bar{h}_1/\bar{h}_2 = 0.1$ (solid line) and 1.0 (dashed line), and $S = 0.5$ (first column) and 0.8 (right column). Thick lines in (A) and (B) shows the hydrostatic solution. (G) Temporal average amplitude of solitary-type waves a as a function of S for $W = \bar{h}_1(2\eta_o)^{-1} = 0.6$, 0.8, and 1.2, and $\bar{h}_1/\bar{h}_2 = 0.1$ and 0.5. Note that the vertical axis is the amplitude normalized by initial perturbation displacement since $2Wa\bar{h}_1 = a/\eta_o$. (H) $sech^2$ shape of the first order KdV equation (solid line) and *tanh* shape of second order KdV equation (dashed line).

Redistribution of energy

The energy contained in the steepened waves and solitary-type waves may be analysed by fitting the analytical homogeneous solution for the linear problem (i.e., normal modes) as a function of time as in Shimizu *et al.* (2007); this is equivalent to using an energy spectrum to capture the energy fluxes between different wave numbers (Maxworthy, 1984; Melville *et al.*, 1989; Fedorov & Melville, 2000). Mathematically, it is possible to express every wave in a convergent series of linear modes (Shimizu *et al.*, 2007). However, in order that the series expansion retains its physical meaning, the series was terminated when the length scale reduces to that of the solitary-type waves. As seen from **Fig. 1.7**, as the solitary-type waves steepened, their amplitude increased and their length scale decreases; clearly this means that the series fit will need to be terminated so that the basin-scale waves and the solitary-type

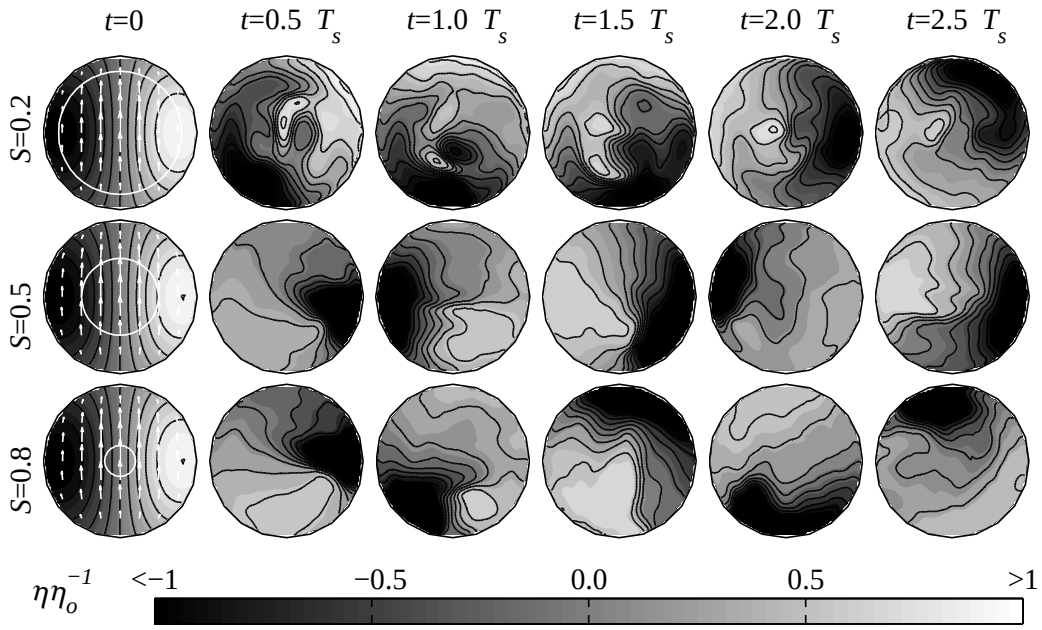

Figure 1.9: Same as **Fig. 1.7** but for an initial monochromatic Poincare wave.

waves remain separate.

As a first step, consider the estimate of the amount of energy contained in such solitary-type waves. The energy, per soliton and per unit of width (radius) along r was obtained from the theoretical solution of the KdV equation (Boegman *et al.*, 2005*b*) as a function of the soliton amplitude. This energy was then summed over the observed train of solitons obtained in the simulation. The energy per soliton (TEs) is given by:

$$\begin{aligned} TEs &= c_o(\rho_2 - \rho_1)g \int_0^{r_o} \int_{-\infty}^{\infty} \eta_2(a(r),t)^2 \, dt \, dr \\ \eta(a(r),t) &= a(r) \, sech\left(\frac{c_o t}{\lambda}\right)^2 \quad ; \quad \lambda^2 = 12\frac{(\bar{h}_1\bar{h}_2)^2}{(\bar{h}_2 - \bar{h}_1)a(r)} \end{aligned} \tag{1.15}$$

where the amplitude $a(r)$ was obtained from the simulation results. The series expansion was then terminated at the number of modes that contained the residual energy equal to that in the train of solitons at a time equal to three steepening times; this required 4 higher azimuthal sub-modes of the Kelvin wave.

Based on the above criteria, the first 10 radial, first 4 azimuthal modes of cyclonic and anticyclonic waves were fitted. The energies contained in the modes were grouped into four classes: leading wave (Kelvin or Poincaré), high azimuthal sub-modes of the leading wave

(denoted in **Fig. 1.10** as K s-mod and P s-mod., respectively), other modes (denoted as other in **Fig. 1.10**), and the non-fitted energy, that corresponded to the residual energy. The energy contained in the solitary-type waves was also calculated using Eq. 1.15. **Fig. 1.10** shows a typical time series of the total energy evolution, normalized by the total energy among the different categories for $W = 0.6$, $\bar{h}_1/\bar{h}_2 = 0.1$, and $S = 0.5$ for an initial Kelvin wave case (**Fig. 1.10A**), and $S = 0.2$, 0.5, and 0.8 for an initial Poincaré wave case (**Fig. 1.10B-D**, respectively). The energy evolution for the initial Kelvin wave was insensitive to S.

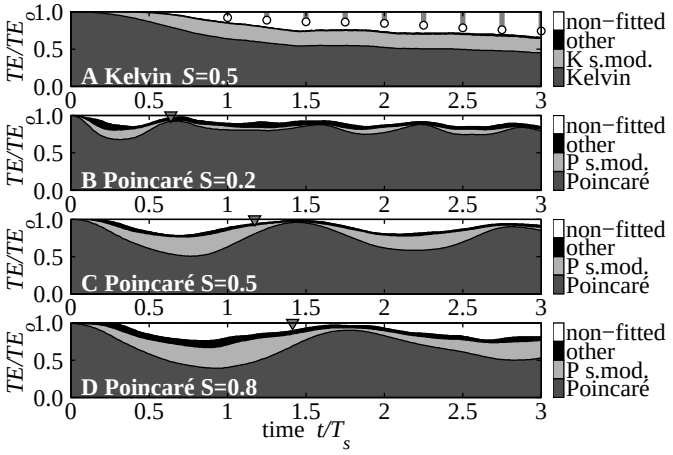

Figure 1.10: Time series of fitted modal energy non-dimensionlized by the total energy of the simulation: (A) an initial Kelvin wave case with $S = 0.5$, and (B-D) an initial Poincaré wave cases with $S = 0.2$, 0.5, and 0.8, respectively. Dark grey corresponds to the leading wave (Poincaré or Kelvin), light grey the higher azimuthal modes of the leading wave, black the energy contained in other basin-scale modes (radial and azimuthal), and white the other components that approximately corresponds to solitary-type waves. White dots in upper panel corresponds to the estimated energy of the solitons (see text) measured as is seen in the grey bars. Triangles in panels B-D indicate the period of the leading Poincaré waves.

For the initial Kelvin wave case, the energy contained in the leading wave was mainly transferred to the sub-modes and the residual energy corresponding to energy contained in solitary-type waves (**Fig. 1.10A**). At $t = 3T_s$, the sub-modes and solitary-type waves had about 20% and 30% of the total energy, respectively (**Fig. 1.10A**). By contrast, for the initial Poincaré wave case (**Fig. 1.10B**, **C** , **D**), the energy was transferred into sub-modes, and then the transferred energy was observed to periodically return to the parent wave forming a limit cycle. The period of that interaction was about 1.2 times the natural period of the Poincaré wave for all the runs. The maximum energy transfer increases with the magnitude of S, being equal to about 30% of the total energy for $S = 0.2$, 50% of the total energy for $S = 0.5$ and 65% of the total energy for $S = 0.8$, indicating that rotation suppresses steepening of a Poincaré wave.

Coupling of free Kelvin and Poincaré waves

The nonlinear interactions between basin-scale waves was analysed by initialising the simulation with the displacement and velocity field described by the linear superposition of a Kelvin and a Poincaré waves that were in phase. Their relative amplitudes were determined from the linear solution of the suddenly imposed wind problem at $t = (T_K - T_P)(T_K T_P)^{-1}$, where T_K and T_P are the periods of Kelvin and Poincaré waves, respectively. Time series of the interfacial displacements at the upwind end and at the center of the basin are shown in **Fig. 1.11A** for the cases, $S = 0.5$, $W = 0.6$ and $\bar{h}_1/\bar{h}_2$. The energy decomposition into the leading Kelvin and Poincaré waves, and the higher azimuthal Kelvin modes are shown in **Fig. 1.11B**.

The steepening and subsequent degeneration of the Kelvin wave into solitary-type waves was similar to the monochromatic Kelvin wave case (**Fig. 1.11A**); however, at the center of the basin, a standing oscillation with a period $T_{KP} = (T_K - T_P)(T_K T_P)^{-1}$ (see triangles in the upper axis in **Fig. 1.11A**) was excited when both the leading waves were in phase. The excitation of this oscillation, at the center of the basin, explains that the oscillation observed at the center of the basin in the suddenly imposed problem, was due to nonlinear interaction of the Kelvin and Poincaré waves excited by the wind and not by the wind forcing itself.

The energy decomposition into modes shows the previously described pattern, i.e., the energy in Kelvin waves were transferred to its sub-azimuthal modes and degenerated into to solitary-type waves, while the energy contained in Poincaré waves remained available for a longer time. Nonlinear interaction between both waves transferred energy to the standing wave with a period of T_{KP}, which was then not recycled back to the Poincaré or Kelvin waves.

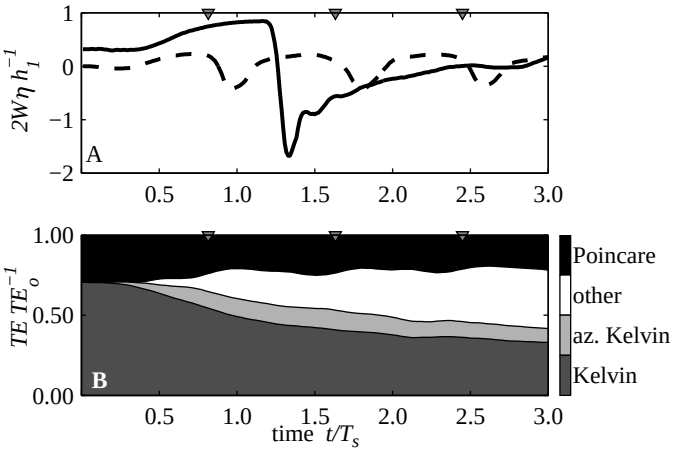

Figure 1.11: (A) Time series of dimensionless interfacial displacement at the upwind end (solid line) and at the center of the basin (dashed line). (B) Time series of fitted modal energy nondimensionlized by the total energy of the simulation for $S = 0.5$, $W = \bar{h}_1(2\eta_o)^{-1} = 0.6$ and $\bar{h}_1/\bar{h}_2$. Triangles in upper axis mark T_{KP} period

Triad nonlinear interaction was thought to explain the excitation of the T_{KP} standing wave (Phillips, 1966). This nonlinear interaction occurs when three wave components satisfy the

relationships $\omega_1 \pm \omega_2 \pm \omega_3 = 0$ and $k_1 \pm k_2 \pm k_3 = 0$, where ω_1, ω_2, and ω_3, are frequencies of the three waves and k_1, k_2, and k_3 are the corresponding wave numbers, the energy can be transferred among the wave components (Phillips, 1966; Hammack & Henderson, 1993). For the first order problem, the governing equations for the lower layer are:

$$\begin{aligned}
&\frac{\partial \eta_2^{(1)}}{\partial t} + h_2 \frac{\partial u_2^{(1)}}{\partial x} + h_2 \frac{\partial v_2^{(1)}}{\partial y} = -\eta_2^{(0)} \left(\frac{\partial u_2^{(0)}}{\partial x} + \frac{\partial v_2^{(0)}}{\partial y} \right) \\
&\frac{\partial u_2^{(1)}}{\partial t} + \epsilon_1 g \frac{\partial \eta_1^{(1)}}{\partial x} + \epsilon_2 g \frac{\partial \eta_2^{(1)}}{\partial x} - f v_2^{(1)} = -u_2^{(0)} \frac{\partial u_2^{(0)}}{\partial x} - v_2^{(0)} \frac{\partial u_2^{(0)}}{\partial y} \\
&\frac{\partial v_2^{(1)}}{\partial t} + \epsilon_1 g \frac{\partial \eta_1^{(1)}}{\partial y} + \epsilon_2 g \frac{\partial \eta_2^{(1)}}{\partial y} + f u_2^{(1)} = -u_2^{(0)} \frac{\partial v_2^{(0)}}{\partial x} - v_2^{(0)} \frac{\partial v_2^{(0)}}{\partial y}
\end{aligned} \tag{1.16}$$

where the super index (0) and (1) denote the leading waves and first order perturbation that describe weak nonlinear effects. It is clear that the set of governing equations for the first order approximation is the same as the linear case (the left hand side of (1.16)), but forced by the nonlinear interaction of the linear solution (the right hand side of (1.16)). The Kelvin-Poincaré interaction is at frequencies $\omega = [2\omega_K, 2\omega_P, \omega_K - \omega_P, \omega_K + \omega_P]$, where ω_K and ω_P are the natural frequencies of Kelvin and Poincaré waves, respectively. As the basin is circular (so that natural frequencies do not occur in multiples of the fundamental frequency) and natural frequencies of the system remain the same as the linear waves, these forcing frequencies do not match with any of the natural frequencies. Therefore, the triad interaction is unlikely to be the excitation mechanism of the wave with a period of T_{KP}, even though the frequency relationship holds.

Another explanation investigated is that the observed oscillation, in the centre of the basin, is simply a forced displacement and governed by (1.16). To show this, in **Fig. 1.12** we plot the temporal average of the energy (within $t = 0$ and $t = 3T_s$) contained in the fitted modes, against the frequency with both variables being obtained from the modal decomposition shown in **Figs. 1.10A**, **1.10C**, and **1.11B**. The horizontal axis of **Fig. 1.12** is the frequency ω, of fitted linear mode, normalized by f and divided by the azimuthal order n. The division by the modal number highlights whether the higher azimuthal modes are locked to the Kelvin, Poincaré, or the forcing frequencies, $\omega_{KP} = \omega_K - \omega_P$ and $\omega_{PK} = \omega_K + \omega_P$. A mode is locked by another one when both angular velocities are equal. For example, the frequency of an azimuthal mode 2 locked by the Kelvin wave, has twice the Kelvin wave frequency and is its sub-harmonic. It is seen from **Fig. 1.12** that the observed frequencies of the azimuthal modes 2 waves are almost equal to the forcing frequency, explaining why, in **Fig. 1.12**, the frequencies ω_K, ω_P, $\omega_{KP}/2$ and $\omega_{PK}/2$ are marked as forcing frequencies.

For a monochromatic Kelvin wave, the case shown in **Fig. 1.12A**, we see that the azimuthal sub-harmonics of the leading Kelvin wave are locked by the leading Kelvin wave as the parent waves steepens; through this representation it is clear that all frequencies belong to the parent

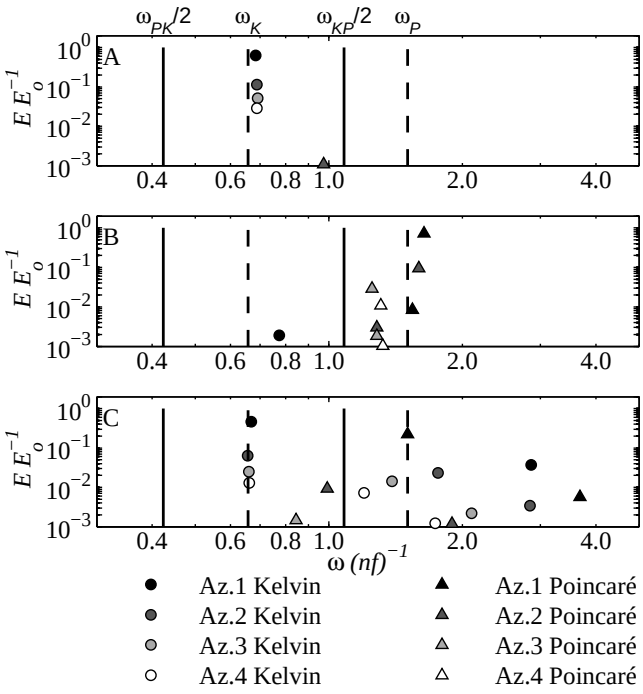

Figure 1.12: Temporal average of the fitted energies of an initial Kelvin wave (**Fig. 1.10A**), an initial Poincaré wave (**Fig. 1.10C**) and an initial super-position of both waves (**Fig. 1.11B**), all for $S = 0.5$, as a function of the computed frequencies on the fitting. Circles denote cyclonic waves and triangles anticyclonic waves, and shading indicates azimuthal modes. Marked frequencies are for pure Kelvin and Poincaré waves (ω_K and ω_P, respectively), and $\omega_{KP}/2 = (\omega_K - \omega_P)/2$ and $\omega_{PK}/2 = (\omega_K + \omega_P)/2$.

wave and its sub-harmonics. A similar result was obtained for the monochromatic Poincaré wave, the results for which are shown in **Fig. 1.12B** with $S = 0.5$; the frequencies of the first two anticyclonic radial modes and their respectively azimuthal sub-modes again belong to or are near to the leading Poincaré wave. A linear combination of Kelvin and Poincaré waves gave rise to sub-harmonics of both the parent Kelvin and Poincaré waves as seen in (**Fig. 1.12C**), but also energy was observed at other frequencies. The exact nature of these waves remains uncertain. The fact that the observed frequencies were not distinctively different from the natural frequencies suggests that the remaining energy, as represented by these non sub-harmonic waves, was merely the manifestation of the nonlinear departure of the interface displacements and thus an artefact of the modal least squares fitting.

Discussion

Helfrich (2007) showed that an initial perturbation of the form of solitons in a non-rotating fluid first degenerates by radiating longer inertia-gravity waves that re-steepen and to form new solitary-type waves that decay and remerge periodically. These observations are some-

what similar to what was described above for Poincare waves. For Kelvin waves our results are even more similar to those for a non rotating fluid as shown by Renouard *et al.* (1986) who observed degeneration of Kelvin waves into solitary-type waves that had $sech^2$ profile in a rotating channel; the effect of rotation only modifying the transverse interface gradient and not influencing the degeneration processes.

In previous research, two major groups of mechanism for the damping of the basin-scale internal waves have been identified: shear stress at the benthic boundary layer (Wüest *et al.*, 2000; Marti & Imberger, 2006) and nonlinear energy transfer into the high frequency waves, that radiate towards the boundary where they break on a sloping bottom (Horn *et al.*, 2001; Boegman *et al.*, 2003, 2005*a*). Interior dissipation due to, for instance, shear instabilities, is small relative to these effects and can be neglected (Wüest *et al.*, 2000).

The mechanisms of degeneration into high frequency waves have been investigated for non-rotating basins (Horn *et al.*, 2001) where the magnitude of the perturbation, W, and the ratio $\bar{h}_1/\bar{h}_2$ were used as the parameters to characterizes the degeneration processes. Different studies conjectured that rotation would reduce the relative importance of the formation of solitary waves. Solitary waves of permanent form as obtained for non rotating flows (Grimshaw *et al.*, 1998; Ostrovsky & Stepanyants, 2005; Helfrich & Melville, 2006) were unknown for rotating flows. However, field measurements have clearly shown the presence of solitary-type high frequency waves in rotating lakes whose feature can be explained based on the non-rotating theory (Boegman *et al.*, 2003; Appt *et al.*, 2004). The degeneration processes described in this paper provides an explanation for their presence, showing that, for timescales less than $3T_s$, the evolution of the Kelvin wave can be likened to a non-rotating long wave. A graphic example of such waves, arising from Kelvin waves is described in Appt *et al.* (2004) from observations in Upper Lake Constance.

The inclusion of both nonlinear and nonhydrostatic accelerations, when describing the response of a stratified rotating lake, has shown that Kelvin waves quickly lose their energy to sub-azimuthal modes and solitary-type waves. By contrast, Poincaré waves do not lose much energy to other modes or high frequency waves, but rather exhibit a limit cycle behaviour where energy is transferred back and forth between the parent wave and its azimuthal sub harmonics. If a Kelvin and Poincaré wave co-exist in a lake they become coupled and give rise to the same azimuthal sub-harmonics, but in addition energy is also drained into distortion of the interface due to nonlinearities.

References

Antenucci, J. & Imberger, J. 2001 Energetics of long internal gravity waves in large lakes. *Limnol. Oceanogr.* **46**, 1760 – 1773.

Antenucci, J., Imberger, J. & Saggio, A. 2000 Seasonal evolution of the basin-scale internal wave field in a large stratified lake. *Limnol. Oceanogr.* **45**, 1621 – 1638.

Appt, J., Imberger, J. & Kobus, H. 2004 Basin-scale motion in stratified upper lake constance. *Limnol. Oceanogr.* **49**, 919 – 933.

Baines, P. G. 1998 *Topographic effects in stratified flows*. Cambridge University Press.

Bennett, J. 1973 A theory of large amplitude kelvin wave. *J. Phys. Oceanogr.* **3**, 57 – 60.

Boegman, L., Imberger, J., Ivey, G. & Antenucci, J. 2003 High-frequency internal waves in large stratified lakes. *Limnol. Oceanogr.* **48**, 895 – 919.

Boegman, L., Ivey, G. & Imberger, J. 2005*a* The degradation of internal waves in lakes with sloping topography. *Limnol. Oceanogr.* **50**, 1620 – 1637.

Boegman, L., Ivey, G. & Imberger, J. 2005*b* The energetics of large-scale internal wave degeneration in lakes. *J. Fluid. Mech.* **531**, 159 – 180.

Bradford, S., Katopodes, N. & Parker, G. 1997 Characteristic analysis of turbid underflows. *J. Hydr. Eng.* **123**, 420 – 431.

Brandt, P., Rubino, A., Alpers, W. & Backhaus, J. O. 1997 Internal waves in the stair of messina studied by numerical model and synthetic aperture radar images from the ers 1/2 satellites. *J. Phys. Oceanogr.* **27**, 648 – 663.

Choi, W. & Camassa, R. 1999 Fully nonlinear internal waves in two-fluid system. *J. Fluid. Mech.* **396**, 1 – 36.

Clark, S. R. & Imberger, J. 1996 Nonlinear effects in the unsteady, critical withdrawal of a stratified fluid. *Dynam. Atmos. Oceans* **24**, 163 – 171.

Csanady, G.T. 1968 Motions in a model great lake due to suddenly imposed wind. *J. Geophys. Res.* **73**, 6435–6447.

Csanady, G.T. 1973 Transverse internal seiches in large oblong lake and marginal seas. *J. Phys. Oceanogr.* **3**, 439 – 447.

Fedorov, A. & Melville, W. K. 1995 Propagation and breaking of nonlinear kelvin wave. *J. Phys. Oceanogr.* **25**, 2518 – 2531.

Fedorov, A. & Melville, W. K. 2000 Kelvin front on the equatorial thermocline. *J. Phys. Oceanogr.* **30**, 1692 – 1705.

Fischer, H., List, R., Imberger, J. & Brooks, N. 1979 *Mixing in Island and Coastal Waters*. Academic Press.

de la Fuente, A., Niño, Y., Muñoz, R. & Frederick, R. 2006 By n-layers, a 2d multilayers model for natural stratified flows. VI International Symposium on Stratified Flows.

Gill, A.E. 1982 *Atmosphere-Ocean Dynamics*. Academic Press.

Gómez-Giraldo, E. A., Imberger, J. & Antenucci, J. 2006 Spatial structure of the dominant basin-scale internal waves in lake kenneret. *Limnol. Oceanogr.* **51**, 229 – 246.

Grimshaw, R. H. J., Ostrovsky, L. A., Shrira, V. I. & Stepanyants, Y. A. 1998 Long nonlinear surface and internal gravity waves in a rotating ocean. *Survey in Geophysics* **19**, 289 – 338.

Hammack, J. L. & Henderson, D. M. 1993 Resonant interactions among surface water waves. *Annu. Rev. Fluid Mech.* **25**, 55 – 97.

Heaps, N. S. & Ramsbottom, A. E. 1966 Wind effects in the water in a narrow two layered lake. *Phil. Trans. R. Soc. Lond. A* **259**, 391–439.

Helfrich, K. 2007 Decay and return of inertial solitary waves with rotation. *Phys. Fluids.* **19**, 026601, doi: 10.1063/1.2472509.

Helfrich, K. & Melville, W. K. 2006 Long nonlinear internal waves. *Annu. Rev. Fluid Mech.* **38**, 395 – 425.

Horn, D.A., Imberger, J. & Ivey, G. 2001 The degradation of large-scale interfacial gravity waves in lakes. *J. Fluid. Mech.* **434**, 181 – 207.

Horn, D.A., Imberger, J., Ivey, G. & Redekopp, L.G. 2002 A weakly nonlinear model for long internal waves in closed basins. *J. Fluid. Mech.* **467**, 269 – 287.

Imberger, J. 1998 *Flux path in a stratified lake: A review.*. 1 - 17 in J. Imberger [ed]. Physical processes in Lakes and Oceans. American Geophysical Union.

Imberger, J. & Hamblin, P. 1982 Dynamics of lakes, reservoirs, and cooling ponds. *Annu. Rev. Fluid Mech.* **14**, 153 – 187.

Lee, C-Y & Beardsley, R. C. 1974 The generation of long nonlinear internal waves in a weakly stratified shear flow. *J. Geophys. Res.* **79**, 453–462.

Loose, B., Niño, Y. & Escauriaza, C. 2005 Finite volume modeling of variable density shallow-water equations for a well-mixed estyary: application to the río maipo estuary in central chile. *J. Hydr. Res.* **43**, 339 – 350.

Marti, C. J. & Imberger, J. 2006 Dynamics of the benthic boundary layer in a strong forced stratified lake. *Hydrobiologia* **568**, 217 – 233.

Maxworthy, R. 1984 Experiments in solitary internal kelvin waves. *J. Fluid. Mech.* **129**, 365 – 383.

Melville, W. K., Tomasson, G. G. & Renouard, D. P. 1989 On the stability of kelvin waves. *J. Fluid. Mech.* **206**, 1 – 23.

Monismith, S.G. 1985 Wind-forced motion in stratified lakes and their effect on mixed-layer shear. *Limnol. Oceanogr.* **30**, 771 – 783.

Mortimer, C.H. 1952 Water movement in lakes during summer stratification; evidence from the distribution of temperature in windermere. *Phil. Trans. R. Soc. Lond. B* **236**, 355 – 398.

Münnich, M, Wüest, A. & Imboden, D.M. 1992 Observations of the second vertical mode of the internal seiche in an alpine lake. *Limnol. Oceanogr.* **37**, 1705 – 1719.

Ostrovsky, L. A. & Stepanyants, Y. A. 2005 Internal solitons in laboratory experiments: Comparison with theoretical models. *Chaos* **15**, 1 – 28.

Phillips, O. M. 1966 The dynamics of the upper ocean. .

Renouard, D. P., Chabert, D. & X., Zhang 1986 An experimental study of strongly nonlinear waves in a rotating system. *J. Fluid. Mech.* **177**, 381 – 394.

Riley, J. J. & Lelong, M. P. 2000 Fluid motion in the presence of strong stable stratification. *Annu. Rev. Fluid Mech.* **32**, 613 – 657.

Ripa, P. 1982 Nonlinear wave-wave interactions in a one-layer reduced-gravity model on the equatorial β plane. *J. Phys. Oceanogr.* **12**, 97 – 111.

Shimizu, K., Imberger, J. & Kumagai, M. 2007 Horizontal structure and excitation of primary motion in a strongly stratified lake. *Limnol. Oceanogr.* **52**, 2641 – 2655.

Spigel, R. & Imberger, J. 1980 The classification of mixed-layer dynamics in lakes of small to medium size. *J. Phys. Oceanogr.* **10**, 1104 – 1121.

Stocker, R. & Imberger, J. 2003 Energy partitioning and horizontal dispersion in a stratified rotating lake. *J. Phys. Oceanogr.* **33**, 512 – 529.

Thompson, R. & Imberger, J. 1980 Response of a numerical model of a stratified lake to wind stress. IIth International Symposium of Stratified Flows.

Tomasson, G. G. & Melville, W. K. 1992 Geostrophic adjustment in a channel: nonlinear and dispersive effects. *J. Fluid. Mech.* **241**, 23–57.

Wüest, A. & Lorke, A. 2003 Small-scale hydrodynamics in lakes. *Annu. Rev. Fluid Mech.* **35**, 373–412.

Wüest, A., Piepke, G. & Van Senden, D. 2000 Turbulent kinetic energy balance as a tool for estimating vertical diffusivity in wind-forced stratified waters. *Limnol. Oceanogr.* **45**, 1388 – 1400.

Nonlinear and nonhydrostatic evolution of basin-scale waves in large deep lakes[†]

Abstract

The nonlinear and nonhydrostatic excitation and degeneration of basin-scale waves in deep and large lakes was studied through combination of nonlinear modal analysis and numerical resolution of the whole spectrum of internal waves in a two-layer fluid. The analytical and numerical results were validated against water temperature measurements in Lake Constance. The interaction among basin-scale waves was characterized by including nonlinear terms in the linear modal equations in order to quantify the energy transferred from the wind-excited scales down to the smaller dissipative scales. Numerical resolution of the wind induced nonlinear and nonhydrostatic two-layer flow in Lake Constance complemented the modal analysis and provided an accurate picture of the energy paths in deep and large lakes. Kelvin wave was found to be the main wind-excited basin-scale wave mode in Lake Constance, and its steepening and subsequent excitation of solitary-type waves was explained on the basis of the nonlinear excitation of higher frequency gravitational waves that draw the main surge. It was also found a rich wave activity with more than one steepened region occurred in the lake, each one leading to the excitation of solitary-type waves that interact with each other and with the bathymetry. Moreover, nonlinear interaction between pairs of wind-excited waves also excites geostrophic gyres that are not necessarily excited by the homogeneous wind blowing, and Poincaré-Kelvin wave interaction was identified to be a source of fast excitation of solitary-type waves. In spite of the large solitary-type wave activity in Lake Constance, the low amount of energy contained in these waves indicates that bottom friction is, above all, the main energy sink in this system. In contrast to the whole basin coherence associated with linear waves, nonlinear and nonhydrostatic dynamics creates localized regions in the lake where damping and mixing mechanisms may act very efficiently.

Introduction

Early studies in lakes dynamics showed that the three-dimensional basin-scale hydrodynamic problem could be simplified using a multi-layer model (Mortimer, 1952), the solution of which may be obtained as a superposition of different vertical and horizontal modes (Csanady, 1968). Horn *et al.* (1986) showed that the wind direction, magnitude, duration, and relative phase with respect to pre-existing surface waves in water bodies determine the wind-wave energy

[†]de la Fuente, A., Shimizu, K., Imberger, J. and Niño, Y. Nonlinear and nonhydrostatic evolution of basin-scale waves in large deep lakes. *Submitted to Limnol. Oceanogr.*

exchange. The subsequent dynamics of each wind-excited wave has been formulated by Shimizu *et al.* (2007).

Once the basin-scale internal waves are excited, different mechanisms act to dissipate these motions (Wüest *et al.*, 2000; Wüest & Lorke, 2003; Boegman *et al.*, 2003). The dominant of these mechanisms is dissipation in the benthic boundary layer (Wüest *et al.*, 2000; Marti & Imberger, 2006; Shimizu & Imberger, 2008). Often, nonlinear steepening of the basin-scale waves leads to high-frequency waves or solitary-type waves where momentum advection and nonhydrostatic pressure gradient are in balance. Permanent or quasi-permanent waves may form that propagate a long distance before finally breaking on the bottom slope of the lake (Helfrich & Melville, 1986; Boegman *et al.*, 2005*a*). Whenever the basin-scale internal waves form regions of high shear, shear instabilities may form that dissipate the energy mostly locally where they are formed (Thorpe & Hall, 1974; Gómez-Giraldo *et al.*, 2008).

Horn *et al.* (2001) showed that the magnitude of the perturbation, $\eta_o \bar{h}_1^{-1}$, and the aspect ratio of the stratification, $\bar{h}_1 H^{-1}$, determine together the primary mechanism accounting for the bulk of the energy dissipation: benthic boundary layer turbulence, non linear steepening or shear instabilities. Here η_o denotes the maximum interfacial displacement, $\bar{h}_1$ and $\bar{h}_2$ are the average upper and lower layer thickness, respectively, and $H = \bar{h}_1 + \bar{h}_2$. η_o can be estimated based on the Wedderburn number, W, (Thompson & Imberger, 1980; Imberger & Hamblin, 1982) as,

$$W = \frac{g' \bar{h}_1^2}{u_*^2 L} \approx \frac{\bar{h}_1}{2\eta_o} \tag{2.1}$$

where $g' = (\rho_2 - \rho_1)\, \rho_o^{-1}$ is the reduced gravity, with g the gravitational acceleration, ρ_1 and ρ_2 the upper and lower layer average water density, respectively, and ρ_o $kg\, m^{-3}$ a reference water density. u_* is the surface shear velocity induced by the wind, and L is defined, for a generic basin (Shintani *et al.* unpubl), as twice the distance between the upwind end and the centre of gravity of the tilted interface.

In a shallow large lake Shimizu *et al.* (2007) scaled the timescale of the linear damping in the benthic boundary layer with the period of the basin-scale waves, estimating the dumping timescale up to 10 times greater than the basin-scale periods. On the other hand, the timescale for the emergence of nonlinearities is given by the steepening formation time, T_s (Horn *et al.*, 2001). The ratio between and the internal period (T_i, Mortimer, 1952) can thus be used for estimating which damping mechanism predominates. This ratio is defined by: (Boegman *et al.*, 2005*a*; de la Fuente *et al.*, 2008)

$$\frac{T_s}{T_i} = \frac{1}{3\eta_o} \frac{\bar{h}_1 \bar{h}_2}{\bar{h}_2 - \bar{h}_1} \approx \frac{2}{3} W \frac{\bar{h}_2}{\bar{h}_2 - \bar{h}_1}. \tag{2.2}$$

In deep lakes where $T_s < T_i$, nonlinear phenomena govern the flow dynamics and different

linear basin-scale waves interact (see Boegman *et al.*, 2005*b*; de la Fuente *et al.*, 2008). The rear steepening of basin-scale waves for $\bar{h}_1\bar{h}_2^{-1} < 1$ maybe interpreted though a spectral analysis as the excitation of shorter gravitational waves (Phillips, 1966; Melville *et al.*, 1989), or by the hyperbolic nature of the governing equations where the wave celerity depends on the interface displacement (Farmer, 1978; Baines, 1998; Toro, 1997). Although both spectral and hyperbolic approaches explain the down scale energy transfer, the physics is incomplete without including the nonhydrostatic accelerations that lock the smaller scale flows at the Brunt-Väisälä or buoyancy frequency (Miles, 1980; Grimshaw & Smyth, 1986; Melville & Helfrich, 1987).

Lake Constance is a good candidate to study the nonlinear and nonhydrostatic dynamics of basin-scale waves as its aspect ration $\bar{h}_1 H^{-1} = 0.08$ ($\bar{h}_1 = 20\,m$, and $H = 256\,m$, Appt *et al.*, 2004). Indeed, different studies have shown the importance of nonlinear processes in Lake Constance. Appt *et al.* (2004) reported results from measurements in 2001, where they observed the excitation of a Kelvin wave, rotating anticlockwise with a period of about 90 h, and a 12 h period Poincaré wave with energy two or three orders of magnitude less than the Kelvin wave, rotating clockwise. They also showed the occurrence of strong upwelling near the north-east perimeter of the lake (see **Fig. 2.1A**) that developed into a surge. Based on the same measurements, Gómez-Giraldo (2007) described the presence of four types of high-frequency waves in Lake Constance: i) waves excited by shear instabilities due to wind Antenucci & Imberger (2001*b*); Gómez-Giraldo *et al.* (2008), ii) waves generated over the Mainau Sill by elevated shear stresses induced by basin-scale waves, iii) waves generated at the crest of steepened basin scale waves, and iv) waves related to the internal surge or bore excited by the upwelling. Lorke *et al.* (2006) had previously documented high frequency waves associated with an upwelling surge in the lake. High frequency waves associated with the straining over the Mainau Sill have been the focus of a number of other studies (Kocsis *et al.*, 1998; Vlasenko & Hutter, 2002).

The aim of the current research is to improve the understanding of the energy transfer from the largest wind-excited waves down to the solitary-type waves. Data from a number of Lake Diagnostic Systems (LDSs Appt *et al.*, 2004) deployed in Lake Constance, obtained during a wind event in 2003 were analysed and strong nonlinear steepening was observed. The nonlinear and nonhydrostatic excitation and degeneration of basin-scale waves in Lake Constance was studied through combination of nonlinear modal analysis and numerical resolution of the whole spectrum of internal waves in a two-layer fluid.

This paper is organized as follows: in Section 2 we present and discuss the field measurements, in Section 3 the methodology of analysis is presented subdivided in basin-scale and high-frequency waves. The basin-scale waves were analysed by extending the modal analysis presented by Shimizu *et al.* (2007) and Shimizu & Imberger (2008), to account for the nonlinear interaction among basin-scale waves, while the high-frequency analysis was conducted by solving the set of 2-layer shallow water equations including nonhydrostatic accelerations. The results of these analyses are presented in Section 4. In the discussion, presented in Section 5, we focus on how the different dumping mechanisms act together in Lake Constance to explain the dissipation of the wind-given energy.

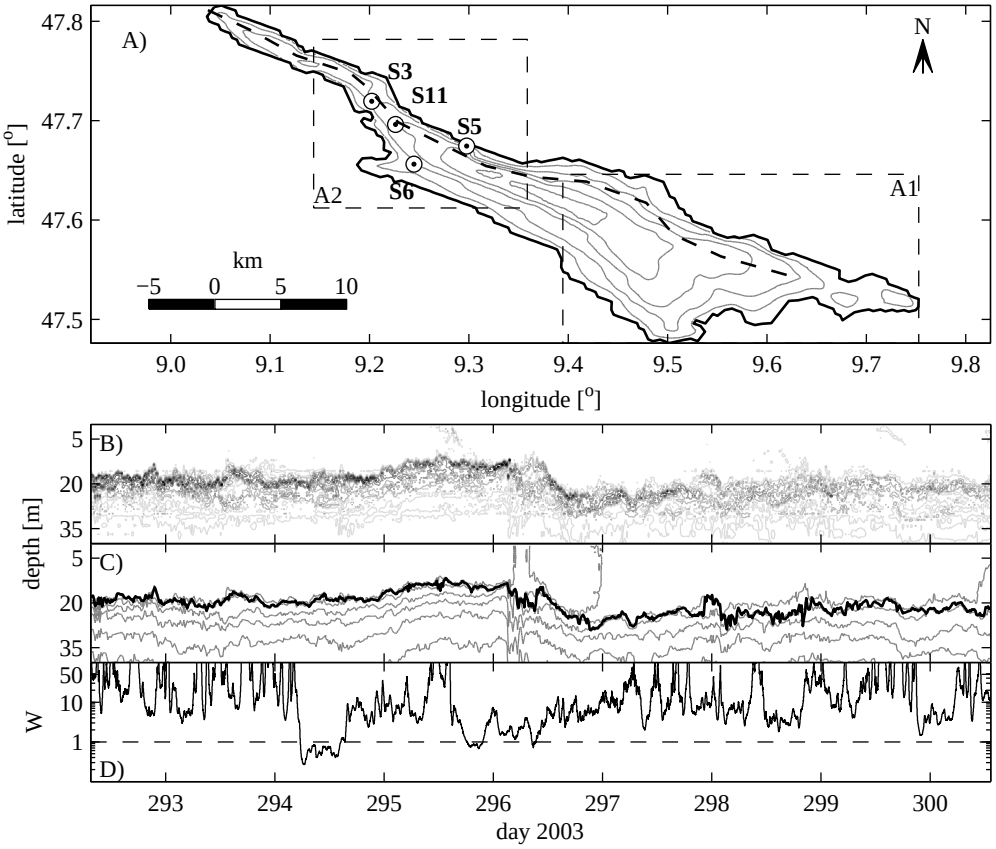

Figure 2.1: (A) Lake Constance bathymetry and placement of LDS. Dashed box A1 and A2 are zoomed areas used within the research. (B, C, D) example of calculous of layer average properties of the stratification based on S11 measurements: (B) Computed vertical profiles of the Brunt-Väisälä frequency. (C) Isotherms between 6 and 11^oC every 1^oC (light lines) and interface location computed by searching the maximum of then Brunt-Väisälä frequency (dark line). (D) Timeseries of the Wedderburn number based on layer average properties ($\bar{h}_1 = 20\ m$ and $\Delta\rho = 0.5655\ kgm^{-3}$) and wind record in S11.

Methods

Field measurements

Lake Constance (9.4^oE, 47.6^oN) is a large, deep Alpine Lake, located on the border between Switzerland and Germany. It is about 60 km long and 15 km wide and the longitudinal axis is oriented along the $NW - SE$ (**Fig. 2.1A**). Lake Constance consists of two connected basins separated by the Mainau Sill; Lake Überlingen, located in the northern end of the lake, with 147 m and 84 m maximum and mean depth, respectively, and Upper Lake Constance, the larger basin, with 252 and 101 m maximum and mean depth, respectively (see Appt *et al.* 2004 or Peeters *et al.* 2007 for further details).

Four LDS (see Appt *et al.* 2004 for a description of the Lake Diagnostic System installation

in Lake Constance) were placed in an area surrounding the Mainau Sill in autumn 2003 (days 292 to 300 of the year). The locations of three of the LDS corresponded to the locations of the 2001 campaign (S3, S5, and S6; Appt *et al.* 2004; **Fig. 2.1A**), while the fourth LDS (S11) was placed at a location designed to capture the evolution of the surge that was observed to enter Lake Überlingen. The thermistor chains on the 4 LDS were 100 m long with a sampling interval of 10 s and a thermistor spacing of 0.75 m in the upper 30 m that gradually increased up to 15 m near the bottom.

The temperature data from the thermistor chain at S11 was used to compute the Brunt-Väisälä frequency, N, as a function of time (**Fig. 2.1B**); N is defined by (e.g. Fischer *et al.*, 1979)

$$N^2 = -\frac{g}{\rho_o}\frac{\partial \rho}{\partial z}, \tag{2.3}$$

where z is an upward vertical axis. The interface, for a two layer approximation, was defined by the depth of maximum N (**Fig. 2.1C**). The upper and lower layer densities were calculated as the depth averaged density for each layer. The density variation was very small, and showed the effect of the surface cooling as autumn progressed and $\Delta\rho$ decreased, with time, at a rate of about 3% per day. The temporal average of and of the upper layer thickness, and the cooling rate (in terms of $\Delta\rho$) are summarized in **Table 1** for each station.

The theoretical analysis was carried out invoking a two layer approximation with a constant density anomaly $\Delta\rho$ of 0.5655 kgm^{-3} and a surface layer depth $\bar{h}_1 = 20$ m (see **Table 1**).

LSD	$\Delta\rho$	h_1	$\partial_t(\Delta\rho)$
	kgm^{-3}	m	$kgm^{-3}d^{-1}$
S3	0.5862	19.75	0.023
S5	0.5281	19.97	0.015
S6	0.5921	23.05	0.021
S11	0.5818	20.32	0.022

Table 1: Summary of temporal average of layer properties

The relative magnitude of the wind forcing to the stabilizing force provided by the stratification can be accounted for by the Wedderburn number based on Shintani *etal.* (unpubl) and this is shown in **Fig. 2.1D**. The first major wind event of the field campaign occurred on day 294, when a 12 h long wind event, of about 10 ms^{-1} magnitude at 10 m above the lake surface, lowered the Wedderburn number to a value of about 0.4, low enough to suggest severe upwelling (a similar event was documented by Appt *et al.* 2004). A large excursion of the interface, with amplitude of about 15 m, was observed late in day 294 at S5 in response to the low Wedderburn number (**Fig. 2.2B**). Once the wind stopped (see **Fig. 2.2A**), a Kelvin wave was generated from the interface response, which rotated anticlockwise and which was

again observed at S11 and S3 (times (2) **Fig. 2.2C** and (3) in **Fig. 2.2D**) with a decreased amplitude, but with a much steepened rear slope. Finally, the Kelvin wave was recorded again at S3 and S11 (times (4) and (5) in **Fig. 2.2D** and **C**, respectively), and at station S6 (time (6) in **Fig. 2.2E**). This evolution of the Kelvin wave is similar to that described by de la Fuente *et al.* (2008) for a rotating wave in a circular-flat bottom basin.

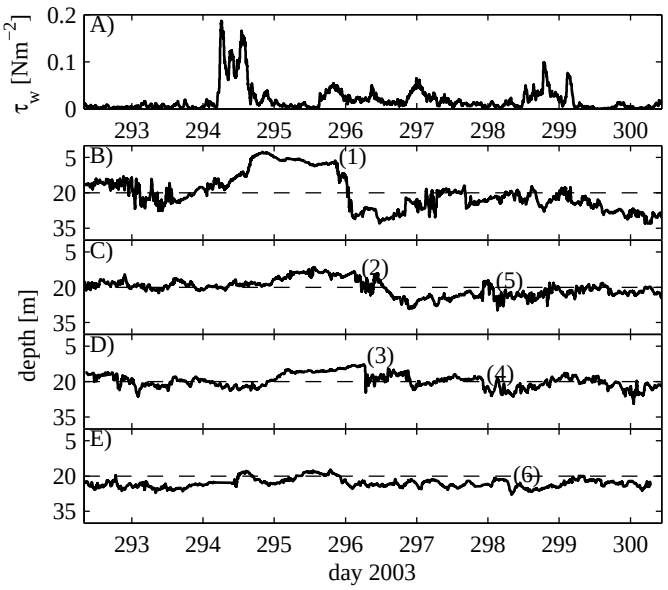

Figure 2.2: (A) Timeseries of the surface shear stress, and (B-E) Timeseries of the interface location for S5, S11, S3 and S6, respectively.

Fig. 2.2B also shows the oscillations of the interface with the period of $\sim$12 h due to Poincaré waves and higher azimuthal mode Kelvin waves, as shown later in this paper. The amplitude of these oscillations (about 2 m) was; however, much smaller than the amplitude of the basin scale Kelvin wave. In addition, a spectral analysis showed interface oscillations due to the Poincaré waves in stations S11, S3 and S6 (not shown here).

Equations for nonlinear interaction among basin-scale waves

*Modal equations**

To extend the modal analysis presented by Shimizu *et al.* (2007) and Shimizu & Imberger (2008) Shimizu et al. (2007) and Shimizu and Imberger (2008) to the nonlinear case, the two-layer governing equations for the primitive variables ($\boldsymbol{\xi} = [\eta_1, \eta_2, \mathbf{u}_1, \mathbf{u}_2]^T$) and the volume flux variables ($\mathbf{q} = [\epsilon_1 g\eta_1, \epsilon_2 g\eta_2, h_1\mathbf{u}_1, h_2\mathbf{u}_2]^T$), were solved allowing for coupling. The surface and interface displacements are denoted by η_1 and η_2, respectively and $h_1 = \bar{h}_1 + \eta_1 - \eta_2$

*Note about authorship: The theoretical background of the nonlinear modal analysis presented in this section belongs to Kenji Shimizu. However, the scaling and perturbation analyses, as well as the application to Lake Constance were entirely developed by the author of this thesis.

and $h_2 = \bar{h}_2 + \eta_2$ are the local instantaneous upper and lower layer thickness, respectively. Notice that $\bar{h}_2(\mathbf{x})$ is a function of the space as it depends on the lake bathymetry. The vector $\mathbf{u}_j = (u_j, v_j)$ denotes the upper ($j = 1$) and lower layer ($j = 2$) flow velocities in a Cartesian coordinate system, and $\epsilon_1 = \rho_1 \rho_o^{-1}$, $\epsilon_2 = \Delta\rho \rho_o^{-1}$.

By working with $\mathbf{q}$ and $\boldsymbol{\xi}$ the total energy, E, is automatically correctly computed since:

$$E = \frac{\rho_o}{2} \int_A \mathbf{q} \cdot \boldsymbol{\xi} \, dA, \tag{2.4}$$

where A denotes the surface area of the lake. The governing equations for both sets of variables may be written as:

$$\frac{\partial \boldsymbol{\xi}}{\partial t} + i \left(\mathbf{L}_\xi + \mathbf{N}_\xi \left(\boldsymbol{\xi} \right) \right) \boldsymbol{\xi} = \mathbf{f}_\xi \tag{2.5a}$$

and

$$\frac{\partial \mathbf{q}}{\partial t} + i \left(\mathbf{L}_q + \mathbf{N}_q \left(\boldsymbol{\xi} \right) \right) \mathbf{q} = \mathbf{f}_q, \tag{2.5b}$$

where $\mathbf{L}_\xi$ and $\mathbf{L}_q$ are linear operators defined by:

$$\mathbf{L}_\xi = \begin{bmatrix} 0 & 0 & \nabla \cdot \bar{h}_1 & \nabla \cdot \bar{h}_2 \\ 0 & 0 & 0 & \nabla \cdot \bar{h}_2 \\ \nabla \epsilon_1 g & 0 & 2\boldsymbol{\Omega} \times & 0 \\ \nabla \epsilon_1 g & \nabla \epsilon_2 g & 0 & 2\boldsymbol{\Omega} \times \end{bmatrix} ; \mathbf{L}_q = \begin{bmatrix} 0 & 0 & \epsilon_1 g \nabla \cdot & \epsilon_1 g \nabla \cdot \\ 0 & 0 & 0 & \epsilon_2 g \nabla \cdot \\ \bar{h}_1 \nabla & 0 & 2\boldsymbol{\Omega} \times & 0 \\ \bar{h}_2 \nabla & \bar{h}_2 \nabla & 0 & 2\boldsymbol{\Omega} \times \end{bmatrix}, \tag{2.6}$$

where $i = \sqrt{-1}$, $\nabla \left[\partial_x, \partial_y \right]^T$ denotes the horizontal gradient operator, $\boldsymbol{\Omega} = [0, 0, f/2]$ denotes the local vertical angular velocity due to the Earth rotation, f is the parameter of Coriolis or inertial frequency, and $\mathbf{f}_\xi$ and $\mathbf{f}_q$, in Eq. 2.5, are vectors containing the external volume and momentum sources, equal to:

$$\mathbf{f}_\xi = \left[0, 0, \frac{\mathbf{u}_* |\mathbf{u}_*|}{h_1}, 0 \right]^T ; \mathbf{f}_q = \left[0, 0, \mathbf{u}_* |\mathbf{u}_*|, 0 \right]^T, \tag{2.7}$$

for the inviscid wind-forced problem without vertical mixing. $\mathbf{u}_*$ denotes the wind induced surface shear velocity vector.

$\mathbf{N}_\xi \left(\boldsymbol{\xi} \right)$ and $\mathbf{N}_q \left(\boldsymbol{\xi} \right)$, in Eq. 2.5, are nonlinear operators that are linearly dependent on $\boldsymbol{\xi}$, and are defined by:

$$\mathbf{N}_{\xi}\left(\boldsymbol{\xi}\right) = i \begin{bmatrix} 0 & 0 & \nabla\cdot\left(\eta_1-\eta_2\right) & \nabla\cdot\eta_2 \\ 0 & 0 & 0 & \nabla\cdot\eta_2 \\ 0 & 0 & \mathbf{u}_1\cdot\nabla & 0 \\ 0 & 0 & 0 & \mathbf{u}_2\cdot\nabla \end{bmatrix}, \tag{2.8a}$$

and

$$\mathbf{N}_{q}\left(\boldsymbol{\xi}\right) = i \begin{bmatrix} 0 & 0 & 0 & 0 \\ 0 & 0 & 0 & 0 \\ \left(\eta_1-\eta_2\right)\nabla & 0 & \left(\nabla\cdot\mathbf{u}_1\right) & 0 \\ \eta_2\nabla & \eta_2\nabla & 0 & \left(\nabla\cdot\mathbf{u}_2\right) \end{bmatrix}. \tag{2.8b}$$

To solve the linear homogeneous problem given by Eq. 2.5, the spatial and temporal variables were assumed to be periodic in time, such that, $\boldsymbol{\xi} = \widetilde{\boldsymbol{\xi}}\left(\mathbf{x}\right)e^{i\omega\, t}$ and $\mathbf{q} = \widetilde{\mathbf{q}}\left(\mathbf{x}\right)e^{i\omega\, t}$, and the linear solution is given by the eigenvalue problems:

$$\left(\omega\mathbf{I}-\mathbf{L}_{\xi}\right)\widetilde{\boldsymbol{\xi}} = \mathbf{0} \;\;;\;\; \left(\omega\mathbf{I}-\mathbf{L}_{q}\right)\widetilde{\mathbf{q}} = \mathbf{0}, \tag{2.9}$$

where $\mathbf{I}$ denotes the identity matrix. These two eigenvalue problems must be equivalent when $h_1 = \bar{h}_1$ and $h_2 = \bar{h}_2$, so that:

$$\widetilde{\mathbf{q}} = \mathbf{M}\widetilde{\boldsymbol{\xi}}, \tag{2.10}$$

where $\mathbf{M}$ is the diagonal matrix whose components are $\left[\epsilon_1 g, \epsilon_2 g, \bar{h}_1, \bar{h}_1, \bar{h}_2, \bar{h}_2\right]$. Moreover, each eigenvalue, k, yields a particular basin-scale wave with an associated eigenfunction, $\widetilde{\boldsymbol{\xi}}\left(\mathbf{x},k\right) = \widetilde{\boldsymbol{\xi}}^{(k)}$ and angular frequency $\omega^{(k)}$. The solution occurs in conjugate pairs with positive, $+k$, and negative, $-k$, modes, with the spatial structure and angular frequency having the property $\widetilde{\boldsymbol{\xi}}^{(-k)} = \widetilde{\boldsymbol{\xi}}^{*(+k)}$ and $\omega^{(-k)} = -\omega^{(+k)}$. Superscript $*$ denotes the complex conjugate.

The eigenfunctions form a complete orthonormal set of functions and so the primitive and volume flux variables maybe expressed as a linear combination of the eigenfunctions:

$$\boldsymbol{\xi} = \sum_{k=-\infty}^{+\infty} a_{\xi}^{(k)}\widetilde{\boldsymbol{\xi}}^{(k)} \;\;;\;\; \mathbf{q} = \sum_{k=-\infty}^{+\infty} a_{q}^{(k)}\widetilde{\mathbf{q}}^{(k)}, \tag{2.11}$$

where $a_{\xi}^{(k)}$ and $a_{q}^{(k)}$ are the complex amplitude of the k^{th} mode for $\boldsymbol{\xi}$ and $\mathbf{q}$ respectively. The complex amplitudes $a_{\xi}^{(k)}$ and $a_{q}^{(k)}$ may be computed from:

$$a_\xi^{(k)} = \frac{1}{e^{(k)}} \left\langle \widetilde{\mathbf{q}}^{(k)}, \boldsymbol{\xi} \right\rangle \;\; ; \;\; a_q^{(k)} = \frac{1}{e^{(k)}} \left\langle \widetilde{\boldsymbol{\xi}}^{(k)}, \mathbf{q} \right\rangle, \tag{2.12}$$

where $e^{(k)} = \left\langle \widetilde{\boldsymbol{\xi}}^{(k)}, \widetilde{\mathbf{q}}^{(j)} \right\rangle \delta_{k,j}$, and $\delta_{k,j}$ is the Kronecker delta (=1 for $j = k$ but 0 otherwise), and

$$\langle \mathbf{a}, \mathbf{b} \rangle = \int_A \mathbf{a}^* \cdot \mathbf{b} \, dA, \tag{2.13}$$

is the inner product between the vectors $\mathbf{a}$ and $\mathbf{b}$. Note that positive and negative complex amplitudes also form conjugate pairs, $a_\xi^{(-k)} = a_\xi^{*(+k)}$ and $a_q^{(-k)} = a_q^{*(+k)}$.

The problem is therefore reduced to define the temporal evolution of the complex amplitude of each mode. The governing equations for the complex amplitudes including the nonlinear interactions may be obtained by substituting Eq. 2.11 into Eq. 2.5, and taking the inner product $\widetilde{\boldsymbol{\xi}}^{(j)}$ and $\widetilde{\mathbf{q}}^{(j)}$ with both sides of Eq. 2.5a and 2.5b, respectively. The governing equation for the complex amplitude of the mode j then becomes:

$$e^{(j)} \frac{da_\xi^{(j)}}{dt} = i\omega^{(j)} e^{(j)} a_\xi^{(j)} + \sum_{l=-\infty}^{+\infty} \sum_{k=-\infty}^{+\infty} n_\xi(j,l,k) a_\xi^{(l)} a_\xi^{(k)} + \widetilde{f}_\xi \tag{2.14a}$$

and

$$e^{(j)} \frac{da_q^{(j)}}{dt} = i\omega^{(j)} e^{(j)} a_q^{(j)} + \sum_{l=-\infty}^{+\infty} \sum_{k=-\infty}^{+\infty} n_q(j,l,k) a_\xi^{(l)} a_q^{(k)} + \widetilde{f}_q \tag{2.14b}$$

where, following Shimizu *et al.* (2007), $\widetilde{f}_\xi^{(j)} = \left\langle \widetilde{\mathbf{q}}^{(j)}, \mathbf{f}_\xi \right\rangle$, $\widetilde{f}_q^{(j)} = \left\langle \widetilde{\boldsymbol{\xi}}^{(j)}, \mathbf{f}_q \right\rangle$ and $\left\langle \widetilde{\boldsymbol{\xi}}^{(j)}, \mathbf{L}_q \widetilde{\mathbf{q}}^{(k)} \right\rangle = \left\langle \widetilde{\mathbf{q}}^{(j)}, \mathbf{L}_\xi \widetilde{\boldsymbol{\xi}}^{(k)} \right\rangle = i\omega^{(j)} e^{(j)} \delta_{j,k}$. $n_\xi(j,l,k)$ and $n_q(j,l,k)$ are coefficients that describes the nonlinear interaction among the modes, and only depends on the spatial shape of the waves, defined as:

$$n_\xi(j,l,k) = \left\langle \widetilde{\mathbf{q}}^{(j)}, \mathbf{N}_\xi \left(\widetilde{\boldsymbol{\xi}}^{(l)} \right) \widetilde{\boldsymbol{\xi}}^{(k)} \right\rangle, \tag{2.15a}$$

and,

$$n_q(j,l,k) = \left\langle \widetilde{\boldsymbol{\xi}}^{(j)}, \mathbf{N}_q \left(\widetilde{\boldsymbol{\xi}}^{(l)} \right) \widetilde{\mathbf{q}}^{(k)} \right\rangle, \tag{2.15b}$$

These are coefficients that quantify how large the changes in the complex amplitude of the j^{th} mode are, due to the nonlinear interaction between the modes l and k. The two nonlinear coefficients are related to each other by:

$$n_q(j,l,k) = n_\xi^*(k,-l,j) \tag{2.16}$$

Spatial correlation

As discussed above, the eigenfunctions form an orthonormal base for the solution space of $\boldsymbol{\xi}$, and any vector in that space can be expressed as the linear combination of the eigenfunctions. From the definition of the nonlinear coefficient, $n_\xi(j,l,k)$, of Eq. 2.15a, the ratio $n_\xi(j,l,k)/e^{(j)}$ may be used to express the surface (in the mathematical sense) $\mathbf{N}_\xi\left(\widetilde{\boldsymbol{\xi}}^{(l)}\right)\widetilde{\boldsymbol{\xi}}^{(k)}$ in terms of the linear combination of the eigenfunctions $\widetilde{\boldsymbol{\xi}}$, such as:

$$\mathbf{N}_\xi\left(\widetilde{\boldsymbol{\xi}}^{(l)}\right)\widetilde{\boldsymbol{\xi}}^{(k)} = \sum_{j=-\infty}^{+\infty} \frac{n_\xi(j,l,k)}{e^{(j)}}\widetilde{\boldsymbol{\xi}}^{(j)} \tag{2.17}$$

Eq. 2.17 shows that the nonlinear interaction between a pair of modes (l and k), is coupled to a third mode (j) only if a correlation exists between the spatial structure of mode j and the spatial structure of $\mathbf{N}_\xi\left(\widetilde{\boldsymbol{\xi}}^{(l)}\right)\widetilde{\boldsymbol{\xi}}^{(k)}$. This is similar to the familiar triad interaction (Phillips, 1966; Hammack & Henderson, 1993), where an interaction occurs between three waves when the wave numbers (κ) satisfy the relationship $\kappa_l \pm \kappa_k = \kappa_j$; such a condition may be obtained by applying Eq. 2.15a to a flat-bottomed rectangular basin characterized by sinusoidal eigenfunctions.

Temporal modulation

In order to obtain an understanding of the nonlinear interactions on the evolution of the complex amplitudes, we scale Eq. 2.5a (Van Dyke, 1975). We choose the characteristic scales for the interfacial displacement as $\widetilde{\eta}_o$, the horizontal and vertical dimensions of the lake as $\widetilde{l}$ and $\widetilde{H}$, respectively, we scale the time with $\widetilde{\omega}^{-1}$, and then we introduce the following order one dimensionless variables: $t^{**} = t\widetilde{\omega}$, $\mathbf{x}^{**} = \mathbf{x}\widetilde{l}^{-1}$, $\bar{h}_i^{**} = \bar{h}_i\widetilde{H}^{-1}$ and $\eta_2^{**} = \eta_2\widetilde{\eta}_o^{-1}$. The superscript $**$ is used to designate scaled variable. In order to balance the terms in the volume conservation equations of the lower layer, the horizontal lower layer velocities must be of order $\left(\widetilde{\eta}_o\widetilde{\omega}\widetilde{l}\widetilde{H}^{-1}\right)$, and so the scaled horizontal velocities become $\mathbf{u}_2^{**} = \mathbf{u}_2\left(\widetilde{\eta}_o\widetilde{\omega}\widetilde{l}\widetilde{H}^{-1}\right)^{-1}$. The chosen scales also mean that $\eta_1^{**} << \eta_2^{**}$, which, from the upper layer volume conservation, implies that $\mathbf{u}_1$ also is $O\left(\widetilde{\eta}_o\widetilde{\omega}\widetilde{l}\widetilde{H}^{-1}\right)$. To allow the correct balance of the horizontal pressure gradient with Coriolis and local accelerations, it is also necessary that $\epsilon_2 g\widetilde{H}\left(\widetilde{\omega}\widetilde{l}^2\right)^{-1}$ is order one, and $\epsilon_1 g\widetilde{H}\left(\widetilde{\omega}\widetilde{l}^2\right)^{-1}$ is $O\left(\eta_1^{**}\right)^{-1}$. Introducing these scales into the momentum equations, and defining the small parameter $\delta = \widetilde{\eta}_o\widetilde{H}^{-1}$, Eq. 2.5a may finally be written, without considering the wind forcing term, in the form:

$$\frac{\partial \boldsymbol{\xi}^{**}}{\partial t} + i\mathbf{L}_{\xi}^{**}\boldsymbol{\xi}^{**} + i\delta\mathbf{N}_{\xi}^{**}\left(\boldsymbol{\xi}^{**}\right)\boldsymbol{\xi}^{**} = \mathbf{0} \tag{2.18}$$

With this scaling, the nonlinear terms in the amplitude equation (Eq. 2.14a) become $O\left(\delta\right)$. The simple case of three interacting waves (j, l and k) may now be analysed. Notice that this analysis should include positive and negative j, l and k waves to obtain real physical quantities. Defining $\mu^{**(j)}$, $\mu^{**(l)}$ and $\mu^{**(k)}$ as, for instance for mode j,

$$\mu^{**(j)} = \frac{n_{\xi}^{**}(j,l,k) + n_{\xi}^{**}(j,k,l)}{e^{**(j)}} \tag{2.19}$$

to be $O(1)$ as they are scaled, the scaled amplitude equations become:

$$\begin{aligned}
\frac{da_{\xi}^{**(j)}}{dt} &= i\omega^{**(j)}a_{\xi}^{**(j)} + i\delta\mu^{**(j)}a_{\xi}^{**(l)}a_{\xi}^{**(k)} \\
\frac{da_{\xi}^{**(l)}}{dt} &= i\omega^{**(l)}a_{\xi}^{**(l)} + i\delta\mu^{**(l)}a_{\xi}^{**(j)}a_{\xi}^{**(k)} \\
\frac{da_{\xi}^{**(k)}}{dt} &= i\omega^{**(k)}a_{\xi}^{**(k)} + i\delta\mu^{**(k)}a_{\xi}^{**(j)}a_{\xi}^{**(l)}
\end{aligned}, \tag{2.20}$$

where $a_{\xi}^{**(j)} = a_{\xi}^{(j)}\widetilde{a}^{-1}$ and $\widetilde{a}^{-1}$ is a characteristic complex amplitude scale and $\omega^{**(j)} = \omega^{(j)}\widetilde{\omega}^{-1}$. We now expand the variables as powers of δ, so that, for example for j, we get:

$$a_{\xi}^{**(j)} = a_{\xi}^{**(j,0)} + \delta a_{\xi}^{**(j,1)} + \delta^2 a_{\xi}^{**(j,2)} + \delta^3 a_{\xi}^{**(j,3)} \ldots \tag{2.21}$$

where $a_{\xi}^{**(j,m)}$ denotes the scaled complex amplitude for j and the solution order m. Replacing Eq. 2.21 in Eq. 2.20, we arrive at:

$$\frac{da_{\xi}^{**(j,m)}}{dt} = i\omega^{**(j)}a_{\xi}^{**(j,m)} + i\delta\mu^{**(j)}a_{\xi}^{**(l,\alpha)}a_{\xi}^{**(k,\beta)} \tag{2.22}$$

with α and β such that $\alpha + \beta = m - 1$. Although different scenarios may be analysed, depending on the choice of values for the scales $\widetilde{a}$ and $\widetilde{\omega}$ and the modes j, l and k; two particular cases are analysed in the next paragraphs:

- $\widetilde{\omega} = f$ and $\widetilde{a}$ is such that the scaled complex amplitudes are $O(1)$, with j, l and k different, but close to f; and

- $\widetilde{\omega} = f$ and $\widetilde{a}$ is such that $a_\xi^{**(l)}$, $a_\xi^{**(k)}$, $\omega^{**(l)}$ and $\omega^{**(k)}$ are $O(1)$, but $a_\xi^{**(j)}$ and $\omega^{**(k)}$ are $O(\delta)$.

The first case describes the nonlinear interaction among three large wind-excited gravity basin-scale waves, while the second case describes the excitation of topographic waves or gyres with angular frequencies much less than f, due to nonlinear interaction between two wind-generated gravity basin scale waves.

In order to simplify the notation, in the following analysis we drop the indexes $**$ and the integration limits are not explicitly shown.

Interaction of large wind-excited gravity basin-scale waves

The zeroth order solution of Eq. 2.22 is a pure rotation such that $a^{(j,0)} = exp\,(i\omega^j\,t)$. This may be placed back into in Eq. 2.22 in order to obtain the first order solution:

$$\frac{da_\xi^{(j,1)}}{dt} = i\omega^{(j)} a_\xi^{(j,1)} + i\mu^{(j)} e^{i\left(\omega^{(l)}+\omega^{(k)}\right)t} \tag{2.23}$$

Eq. 2.23 has the analytic solution given by:

$$a_\xi^{(j,1)}(t) = \frac{1}{1+\frac{\mu^{(j)}}{\omega^{(l)}+\omega^{(k)}-\omega^{(j)}}}\left[e^{i\omega^{(j)}\,t} + \frac{\mu^{(j)}}{\omega^{(l)}+\omega^{(k)}-\omega^{(j)}} e^{i\left(\omega^{(l)}+\omega^{(k)}\right)t}\right] \tag{2.24}$$

Eq. 2.24 is also valid for the first order solution of modes l and k. Therefore, the modulated amplitude of each mode formed by the interaction of a simple rotation with the natural angular frequency plus an oscillatory component with a forced frequency $\omega_f^{(j)} = \omega^{(l)}+\omega^{(k)}$ and amplitude linearly depending on the value of $\mu^{(j)}$, has a mathematical singularity at $\omega^{(j)} = \omega^{(l)}+\omega^{(k)}$. Repeating the same procedure we may obtain the second order solution, which is similar to Eq. 2.24, but with forcing frequencies $\omega_f^{(j)} = \left[\omega^{(l)}+\omega^{(k)}, \omega^{(j)}+2\omega^{(k)}, \omega^{(j)}+2\omega^{(l)}\right]$.

Topographic or geostrophic wave excitation

For the second analysed case, Eq. 2.20 reduces to:

$$\begin{aligned}
\frac{da_\xi^{(j)}}{dt} &= i\delta\omega^{(j)}a_\xi^{(j)} + i\mu^{(j)}a_\xi^{(l)}a_\xi^{(k)} \\
\frac{da_\xi^{(l)}}{dt} &= i\omega^{(l)}a_\xi^{(l)} + i\delta^2\mu^{(l)}a_\xi^{(j)}a_\xi^{(k)} \ , \\
\frac{da_\xi^{(k)}}{dt} &= i\omega^{(k)}a_\xi^{(k)} + i\delta^2\mu^{(k)}a_\xi^{(j)}a_\xi^{(l)}
\end{aligned} \tag{2.25}$$

The first consequence of this scaling is that the complex amplitudes of modes l and k are not modified by the nonlinear interactions with j until the second order, while the complex amplitude of j does not "feel", at first order, its own rotation, given that the timescale of the nonlinear processes was faster than the natural frequency of mode j.

Two possible combinations of l and k modes modify then the complex amplitude of j. The first combination is when l and k are different waves, and

$$a^{(j,0)} = \frac{\mu^{(j)}}{\omega^{(l)} + \omega^{(k)}} e^{i\left(\omega^{(l)}+\omega^{(k)}\right)t}, \tag{2.26}$$

which shows a similar behaviour than for the previous case analysed. However, the natural frequency of the slower waves does not appear in the solution because the nonlinear interaction between l and k is fast.

The second combination of l and k waves is when they are conjugate pairs ($\omega^{(l)} = -\omega^{(k)}$). In this case,

$$a^{(j,0)}(t) = \mu^{(j)}\, t, \tag{2.27}$$

which gives a direct excitation of slower waves due to the nonlinear interaction between pairs of gravitational waves, usually well excited by the wind blowing over the lake.

*Energy transfers**

The energy equation for the mode j is obtained by pre-multiply Eq. 2.14a by $a_q^{*(j)}$, the complex conjugate of Eq. 2.14b by $a_\xi^{*(j)}$ and then adding the resulting equations. This results in the energy equation for j, which may be written as:

*see footnote of pag. 31

$$\frac{dE^{(j)}}{dt} = \sum_{l=-\infty}^{+\infty} \sum_{k=-\infty}^{+\infty} \dot{F}(j,l,k) + \dot{W}^{(j)} \tag{2.28}$$

where

$$E^{(j)} = \frac{1}{2}\rho_o e^{(j)} \left(a_q^{(j)} a_\xi^{*(j)} + a_q^{*(j)} a_\xi^{(j)} \right), \tag{2.29}$$

is the total energy contained in the mode j.

$$\dot{W}^{(j)} = \rho_o \left(a_\xi^{*(j)} \widetilde{f}_q^{(j)} + a_\xi^{(j)} \widetilde{f}_q^{*(j)} + a_q^{*(j)} \widetilde{f}_\xi^{(j)} + a_q^{(j)} \widetilde{f}_\xi^{*(j)} \right) \tag{2.30}$$

is the energy flux exchanged between the mode j and the wind, and

$$\dot{F}(j,l,k) = i\rho_o Im \left(a_q^{*(j)} n_\xi(j,l,k) a_\xi^{(l)} a_\xi^{(k)} - a_\xi^{(j)} n_\xi^*(j,l,k) a_\xi^{*(l)} a_q^{*(k)} \right) \tag{2.31}$$

denotes the rate of changes of energy in mode j due to the nonlinear interaction between modes l and k. Taking the sum over the conjugate pairs of j, l and k and using the relationship between n_ξ and n_q given by Eq. 2.16, we obtain that net change in energy of the mode j due to the nonlinear interaction between l and k, which is given by:

$$\sum_{\pm j} \sum_{\pm l} \sum_{\pm k} \dot{F}(j,l,k) = \begin{pmatrix} a_q^{*(j)} \left(n_\xi(j,l,k) a_\xi^{(l)} a_\xi^{(k)} + n_\xi(j,-l,k) a_\xi^{*(l)} a_\xi^{(k)} \right) + \\ + a_q^{*(j)} \left(n_\xi(j,l,-k) a_\xi^{(l)} a_\xi^{*(k)} + n_\xi(j,-l,-k) a_\xi^{*(l)} a_\xi^{*(k)} \right) \\ - a_q^{*(k)} \left(n_\xi(k,l,j) a_\xi^{(l)} a_\xi^{(j)} + n_\xi(k,-l,j) a_\xi^{*(l)} a_\xi^{(j)} \right) \\ - a_q^{*(k)} \left(n_\xi(k,l,-j) a_\xi^{(l)} a_\xi^{*(j)} + n_\xi(k,-l,-j) a_\xi^{*(l)} a_\xi^{*(j)} \right) \end{pmatrix}. \tag{2.32}$$

There is a symmetry in the energy exchange such that the above flux is equal and opposite to the total changes in the energy of the mode k due to the nonlinear interaction between the modes l and j, and their respective conjugate pairs. Eq. 2.32 represents then, the net energy flux from the mode j to the mode k through the action of the mode l. Finally, the total energy flux from the mode j to the mode k via the total wave fields, $F_\xi(j,k)$, is equal to the sum of Eq. 2.32 from all the modes l:

$$F_\xi(j,k) = \sum_{l=-\infty}^{+\infty} \dot{F}\left(\pm j, l, \pm k\right). \tag{2.33}$$

Equations for solitary-type waves

The high-frequency waves were computed by solving the two layer equations (with non-hydrostatic accelerations) on a grid small enough to reproduce the solitary-type waves (Botelho & Imberger, 2008). For computational convenience, the surface mode was removed from the dynamics and the set of invicid governing equations were reduced to:

$$\frac{\partial h_2}{\partial t} + \frac{\partial u_2 h_2}{\partial x} + \frac{\partial v_2 h_2}{\partial y} = 0, \tag{2.34a}$$

for the lower layer volume conservation,

$$\frac{\partial u_2 h_2}{\partial t} + \frac{\partial u_2 u_2 h_2}{\partial x} + \frac{\partial v_2 u_2 h_2}{\partial y} - f v_2 h_2 + \frac{h_2}{H}\left(\frac{\partial}{\partial x}\left(u_2 u_2 h_2 \frac{H}{h_1}\right) + \frac{\partial}{\partial y}\left(u_2 v_2 h_2 \frac{H}{h_1}\right)\right) + \\ + c\frac{\partial \eta_2}{\partial x} = -u_{*x}u_*\frac{h_2}{H} + \frac{1}{3}\left(\frac{h_1}{H}\frac{\partial h_2^3 G_2}{\partial x} - \frac{h_2}{H}\frac{\partial h_1^3 G_1}{\partial x}\right), \tag{2.34b}$$

for conservation of x momentum and,

$$\frac{\partial v_2 h_2}{\partial t} + \frac{\partial u_2 v_2 h_2}{\partial x} + \frac{\partial v_2 v_2 h_2}{\partial y} + f u_2 h_2 + \frac{h_2}{H}\left(\frac{\partial}{\partial x}\left(u_2 v_2 h_2 \frac{H}{h_1}\right) + \frac{\partial}{\partial y}\left(v_2 v_2 h_2 \frac{H}{h_1}\right)\right) + \\ + c\frac{\partial \eta_2}{\partial y} = -u_{*y}u_*\frac{h_2}{H} + \frac{1}{3}\left(\frac{h_1}{H}\frac{\partial h_2^3 G_2}{\partial y} - \frac{h_2}{H}\frac{\partial h_1^3 G_1}{\partial y}\right), \tag{2.34c}$$

for the conservation of y momentum. In Eq. 2.34, h_2, u_2 and v_2 denote the lower layer instantaneous thickness and horizontal velocities in x and y, respectively; H is the spatially varying total water depth and $h_1 = H - h_2$ is the upper layer instantaneous thickness, $c = \sqrt{\epsilon_2 g h_1 h_2 H^{-1}}$ and $\eta_2 = h_2 + z_b$ is the interface elevation where z_b denotes the bottom elevation. The wind shear velocity components in x and y directions are designated by u_{*x} and u_{*y}, respectively, and $u_*^2 = u_{*x}^2 + u_{*y}^2$. The operators G_1 and G_2 were defined, following Choi & Camassa (1999), as:

$$\begin{aligned} G_1 &= -\frac{\partial}{\partial t}\nabla\cdot\mathbf{u}_1 + u_2\frac{h_2}{h_1}\frac{\partial}{\partial x}\nabla\cdot\mathbf{u}_1 + v_2\frac{h_2}{h_1}\frac{\partial}{\partial y}\nabla\cdot\mathbf{u}_1 - (\nabla\cdot\mathbf{u}_1)^2 \\ G_2 &= -\frac{\partial}{\partial t}\nabla\cdot\mathbf{u}_2 + u_2\frac{\partial}{\partial x}\nabla\cdot\mathbf{u}_2 + v_2\frac{\partial}{\partial y}\nabla\cdot\mathbf{u}_2 - (\nabla\cdot\mathbf{u}_2)^2 \end{aligned} \tag{2.35}$$

Consistent with the above assumptions, we may assume (Helfrich, 2007):

$$\mathbf{u}_1 h_1 + \mathbf{u}_2 h_2 = 0 \tag{2.36}$$

To see this, the complete two layer equations (de la Fuente *et al.*, 2008) were simplified by assuming a rigid lid approximation for the free surface that gives Eq. 2.36 for relating the upper and lower layer velocities in close domains (Helfrich, 2007). With the rigid lid assumption, the surface displacement is replaced by a surface pressure distribution on the lid, which then in turn interacts with the momentum equations.

The Godunov-type numerical scheme, described by de la Fuente *et al.* (2008), was used to solve the equations (similar numerical schemes and applications can also be found in Toro 1997). In shallow areas, where there is no interface ($h_2 = 0$) or there is full upwelling ($h_1 = 0$), the traditional free surface shallow water equations (e.g. Toro, 1997) were solved neglecting the horizontal pressure gradient. The wetting-drying problem was catered for by establishing a minimum layer thickness ($= 10\ cm$) that was taken as the cut off in the transition from wet to dry.

Simulations setup

All simulations were carried out for a typical stratification with $\Delta\rho$ of 0.5655 kgm^{-3} and a surface layer depth $\bar{h}_1$ of 20 m. The wind record from S5 was corrected to a height of 10 m using a simple neutral boundary layer correction and then this was used to compute the wind shear stress acting over the water surface using a drag coefficient of 1.34×10^{-3}.

The simulations were started about 2 hours before the recorded wind event on day 294.05, (see **Fig. 2.1D** and **Fig. 2.2A**) and continued for three days using three codes: linear and nonlinear hydrostatic, and fully nonlinear nonhydrostatic 2-layer configurations. Linear and nonlinear codes are based on the modal analysis, while the called nonhydrostatic code solves the hyperbolic governing equations. The three days duration was chosen as this was the time it took for the rear front, generated near the southern boundary to reach the north-west end of the lake.

For the modal analysis simulations we used 400 conjugate pairs modes with the lower period cutoff of 3.8 h. The eigenvalue problem was discretized following Shimizu *et al.* (2007) in a staggered mesh of square elements with sides 600 m long. The computations involved manipulating a cubic matrix $n_\xi(j,l,k)$ and the computational time limited the grid size, for instance, $n_\xi(j,l,k)$ in this application has about 256 million of nonzero elements. As the nonlinear analysis requires positive layer thickness, the lake bathymetry was slightly adjusted such as not to obtain negative lower layer thickness, by deepening the bottom elevation in shallow areas down to 40 m below the surface. Further, in order to observe the evolution of the nonlinear wave steepening without wind interference, the wind stress was set to zero after a time $t = 1.5\ d$.

For the full non-hydrostatic analysis, a smaller grid was required in order to allow the waves to reach permanent form (Botelho & Imberger, 2008) and thus we used a regular mesh of square elements with sides 30 m long, and the wind was allowed to continue to the end of the simulation period. It must also be recalled that the purpose of these simulations was to

understand the evolution of the high frequency waves and that the rigid lid approximation prevents non-gravitational waves, such as topographic or geostrophic waves, to develop.

Results

Validation

The comparison between the field measurements and simulation results is shown in **Fig. 2.3**. **Fig. 2.3A** shows the timeseries of the rate of wind power input to the lake, while **Fig. 2.3B** shows the timeseries of the total wind energy entering the lake compared to the energy, locked up in the internal motions, as computed using the nonhydrostatic model. The difference between these lines (grey area in **Fig. 2.3B**) corresponds to the numerical diffusion in the nonhydrostatic model; equivalent to about 10% of the total energy input by the wind after 3 days of simulation. **Fig. 2.3C** to **F** compare the timeseries of the interface displacement computed by the nonlinear (light solid line) and nonhydrostatic models (dark solid line) with the measured thermocline depth (grey line), for S5 (**Fig. 2.3C**), S11 (**Fig. 2.3D**), S3 (**Fig. 2.3E**) and S6 (**Fig. 2.3F**). Vertical dashed lines show the time when the wind forcing was turned off for the nonlinear simulations.

Given the constraints imposed by the computational time that limited the grid size, the interface displacements from the nonlinear model were computed neglecting the last 60 modes, effectively increasing the timescale cut off from 3.8 hours to 5.6 hours. This was necessary as it was observed that the higher wave number modes were unstable and contained unrealistic energy levels.

Comparison between the measured timeseries and those predicted by all three models is excellent, but with a noticeable improvement for the nonlinear and nonhydrostatic models, at the high wave number end. Two differences should, however, be highlighted; the simulated front velocities by both models are slower than those observed in the measurements, and the simulated amplitudes are larger than those of the measurements (dark and light solid lines in **Figs. 2.3C** to **F**).

These differences, most likely, find their origin in the assumption of a constant density anomaly. Second, Appt *et al.* (2004) established the importance of considering a heterogeneous wind distribution in Lake Constance in order to improve all the simulations results. These two aspects could be incorporated in the present analysis to improve the results of the simulations, however, we chose not to consider them, as the focus of this paper is to elucidate the effect of a nonhydrostatic pressure field on nonlinear steepening and dispersion of internal waves.

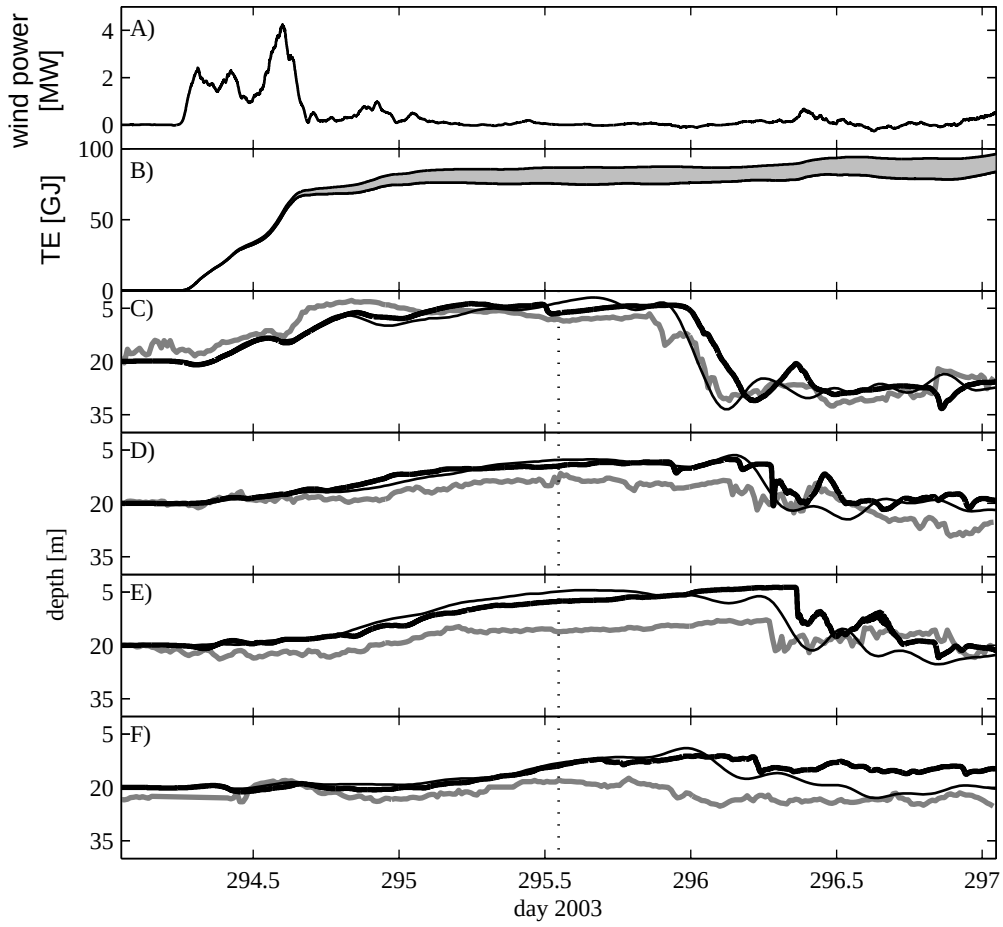

Figure 2.3: (A) Nonhydrostatic computed timeseries of the wind power. (B) Total energy and total wind-given energy computed by nonhydrostatic simulations, grey area shows numerical diffusion. (D-F) Measured thermocline depth (grey lines), and interface displacement computed by nonlinear model (light solid line) and nonhydrostatic model (dark solid line) for S5, S11, S3 and S6, respectively. Vertical dotted line mark time when wind forcing was cut in nonlinear simulations.

Wave steepening as precursor of solitary-type waves

Kelvin wave

In **Fig. 2.3** a Kelvin wave is identified in the field data, which steepens before degenerating into solitary waves. This is analogous to what was documented by de la Fuente *et al.* (2008) for the case of a two-layer stratification in a circular basin. The Kelvin wave detected is a subinertial wave that had one crest (horizontal mode 1) and flow velocities parallel to the shore (H1 or K1, $\omega^{(1)} = 0.15f$, or period of 4.5 d).

The simulations show (see **Fig. 2.4A**) how the parent Kelvin wave transferred energy to other basin-scale waves; the solid dark line shows the energy resulting from the interaction with the wind, while the grey areas show the energy transferred to other gravitational waves

(light grey) and gyres (dark grey). The white area below the grey areas is, therefore, the total Kelvin wave energy. The energy fluxes were computed using Eq. 2.33 and the shaded and dotted lines in **Fig. 2.4A** are the total energy in all basin-scale waves and the total energy in all the modes, respectively. Here, the term gravitational waves refers to the cyclonic and anticyclonic wave modes (Antenucci *et al.*, 2000; Antenucci & Imberger, 2001*a*), while the term "gyre" is used for topographic wave modes that have low frequencies and appear as gyres in the flow velocity (Shimizu *et al.*, 2007). The sum of both classes gives the 400 basin scale waves used in the analysis. The shape of the gravitational waves in Lake Constance has been discussed in detail by Wang *et al.* (2000), and in elliptical and circular basins by Antenucci & Imberger (2001*a*) and Stocker & Imberger (2003), respectively.

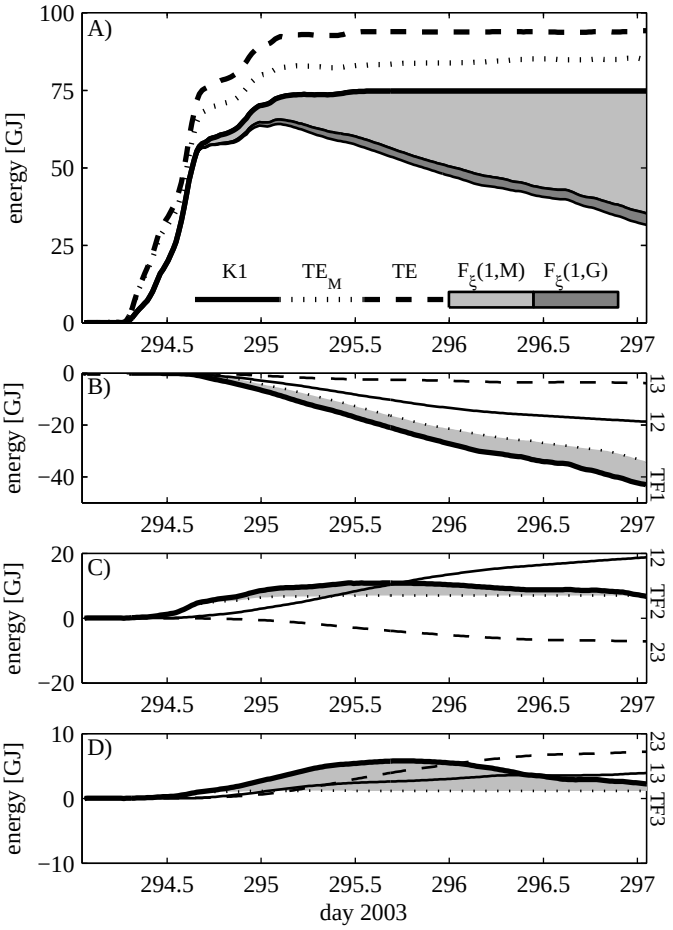

Figure 2.4: (A) Timeseries of computed modal energy by nonlinear model: total energy (dashed line), total energy in the 400 modes (dotted line), total wind-given energy to Kelvin wave (dark solid line), energy radiated to other gravitational waves (light grey area) and gyres (dark grey area). (B-D) nonlinear energy transfer to Kelvin, H2 and H3 waves. Interacting pairs are indicated by number right-hand axis (from-to), TF1 denote transfer from Kelvin wave to all the basin-scale waves, and dotted line to first 12 wave modes,TF2 and 3 denote total energy in H2 and H3 and dotted line is the wind-given energy. Gray area indicates the net rate of change of the energy due to nonlinear interactions. Notice that dotted lines have different meaning for B and C-D.

Fifty percent of the wind energy used to generate the parent Kelvin wave was, after about 2

days, radiated down scale to other faster and smaller gravitational modes that contribute to the steepening of the rear front. The energy in the faster modes was, therefore, larger than that due to the direct wind forcing. The smaller basin-scale waves also act as a bypass in this energy transfer between larger down to the smaller waves, taking energy from the larger scale waves and transferring it in to the smaller scale waves.

To illustrate these aspects, **Fig. 2.4B** to **D** show the timeseries of the cumulated energy fluxes (Eq. 2.33) among the three first modes. **Fig. 2.4B** shows the cumulated energy transfer from the Kelvin wave to all the gravitational and gyre modes (dark line), the cumulated energy transfer to H2 and H3 (azimuthal Kelvin 2 and 3, solid light and dashed lines, respectively), and the total energy radiated to the first 12 azimuthal Kelvin wave modes (dotted line). The grey area in that figure represents the energy radiated to all of the other basin-scale waves. The energy radiated to the first 12 azimuthal Kelvin wave modes represents about 75% of the total energy radiated from the Kelvin wave; about 60% and 10% of it is radiated to H2 and H3, respectively (**Fig. 2.4B**). The energy radiated from K1 to H2 and H3 is, consequently, plotted in **Fig. 2.4C** and **D** with opposite sign (solid light lines in both figures), as it is the reciprocal energy transfer between H2 and H3 (dashed lines in **Fig. 2.4C** and **D**).

As a consequence of this down scale energy transfer, where the waves get energy from larger waves, and release it down to smaller waves, the total energy contained in H2 and H3 is larger than the direct energy input from the wind to those modes, but smaller than the contribution from H1, and H1 and H2, respectively. The total energy in H2 and H3 is plotted with dark lines in **Fig. 2.4C** and **D**, respectively, while the total energy input from the wind is shown in the same figures with dotted lines. Grey areas in **Fig. 2.4C** and **D** are, therefore, the net energy transferred from-to other basin-scale waves.

Multi-steepening dynamics

The energy transfer from the Kelvin wave to shorter basin-scale waves explains the rear front and the subsequent excitation of solitary-type waves. Nevertheless, the nonhydrostatic simulation showed a rich wave activity reflected in more than one steepening of the interface displacement and degeneration into solitary-type waves. **Fig. 2.5B** shows the temporal evolution of longitudinal profiles of the interface displacement along the axis defined in the dashed line of **Fig. 2.1A**. **Fig. 2.5B** represents the temporal evolution of interface displacement. In this figure, the horizontal axis is the distance measured from the north-west end of the lake. To reference these profiles in space and in time, **Fig. 2.5A** shows the bathymetry along the same longitudinal axis, where the triangles on its upper axis identify LDS S3, S11 and S5. **Fig. 2.5C** shows the timeseries of the wind stress.

The gradual steepening of the simulated Kelvin wave is tracked from the end of the wind event, arriving to the northern end of the lake by the end of the simulation. The diagonal dashed line delimited by triangles in **Fig. 2.5B** shows the position of the main front. Nevertheless, several other fronts with smaller amplitude are identified travelling along the entire lake in all directions. For example, the dashed line limited by circles in **Fig. 2.5B** track the position of

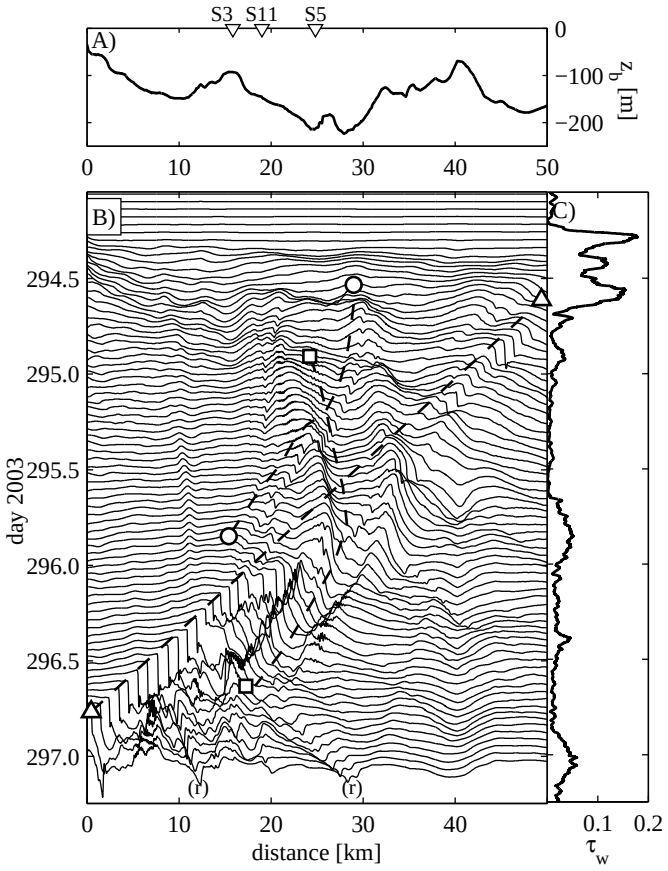

Figure 2.5: (A) bottom elevation along the axis defined in **Fig. 2.1B**. (B) Temporal evolution of longitudinal profiles of the interface displacement for axis identified in **Fig. 2.1A**. Dashed lines and (r) marks are used for the text. (C) timeseries of the wind stress.

a vertical front that, on its early stage ($294.5 < t < 295$) is locked at about 30 km from the north end, and then travels in the same direction as the main front (anticlockwise rotation), but with smaller velocity. Finally, it disappears at the Mainau Sill (LDS S3, **Fig. 2.5A**).

A similar behaviour is found by following the dashed line delimited by squares in **Fig. 2.5B**, which tracks one local maximum interface displacement that begins travelling in the direction opposite to that of the Kelvin wave, and changes direction after interacting with the main front. This local maximum, as well as others in **Fig. 2.5B**, are also seen in the nonlinear simulations (light solid lines in **Fig. 2.3C** to **F**), and correspond to the interfacial displacement coming from the superposition of several basin scale waves exited for producing the main steepening. However, these local maximum are not detected in the field measurements except for the data taken in S5 (see **Fig. 2.3C**), and the explanation for this difference between measurements and simulations is discussed in following sections.

Finally, in Lake Überlingen, the narrow area of Lake Constance between km 0 and 15 of **Fig. 2.5B**, the wave activity is increased by morphological conditions such as Mainau Sill and

the reduction of the cross section area. These factors act together to produce, for example, reflected waves that travel back to the main basin, like the two waves marked by (r) in the lower axis of **Fig. 2.5B**.

Gyres excitation

The simulations show that about the 10% of the energy radiated from the Kelvin waves is transferred to gyre waves (**Fig. 2.4A**), whose natural angular frequency is small with respect to the natural angular frequency of the gravitational wind-exited waves. The gyre modes are characterized by having a small amount of potential energy with respect to their kinetic energy, and arise from the acceleration-Coriolis terms balance in case of geostrophic waves, of by topographic effects. Shimizu *et al.* (2007) showed that a homogeneous wind does not excite the geostrophic modes and this criterion can be used to differentiate between geostrophic or topographic waves. The linear simulations, however, always produced the excitation of these waves with small amplitude, and it is unclear whether this is because they correspond to topographic waves or is related with numerical issues.

Fig. 2.6A shows the timeseries of the energy contained in K1 (solid dark line), three gyres with natural period of 61, 38 and 7.5 days (dashed lines with coloured circles) and the energy contained the complete set gyre modes (dotted line). The pseudo-spectrum of the energy computed by linear (grey dots) and nonlinear (solid line) models, corresponding to the time marked with (B) in the upper horizontal axis of **Fig. 2.6A**, is potted in **Fig. 2.6B**. The angular frequencies in the horizontal axis are the natural angular frequencies of each basin-scale wave. The three studied gyres (dashed lines in **Fig. 2.6A**) are identified in the frequency domain in the upper horizontal axis of **Fig. 2.6B** as (G1), (G2), and (G2). For reference, other modes are also identified in the upper horizontal axis of **Fig. 2.6B**. The energy contained on each gyres is about two or three orders of magnitude smaller than the energy contained in the wind-exited waves (K1, H2, etc., **Fig. 2.6A** and **B**), however, the total energy contained in all of the gyre waves represents about 10% of the total wind energy, and is mostly kinetic energy.

Linear results show that the gyres excitation due to the wind blowing can be neglected for waves with $\omega << f$. In fact, the energy of the gyre waves grows with $\omega^{3.25}$ up to about $\omega f^{-1} \approx 0.1$ (linear fit in log-log scale of **Fig. 2.6B**), and the energy of waves with $\omega f^{-1} \approx 0.1$ is about 8 orders of magnitude less than the energy of K1. The explanation for this is based on the short wind duration (12 hours) with respect to the timescale associated with the natural frequency of these waves. The impact of a 12 hours wind on a 68 days wave ($\omega f^{-1} \approx 0.1$), is equivalent to a wind duration of about 45 minutes on K1 with 4.5 days of natural period in terms of the total energy transfer per period. On the contrary, nonlinear results predict that the gyres energy is a couple of orders of magnitude larger than that predicted in the linear case. Also, in the nonlinear simulations, the relationship between frequency and energy is not as clear as for the linear results, the energy having a rather constant value in the range $\omega f^{-1} < 0.1$, instead of the energy decay for lower frequencies obtained in the linear case (**Fig. 2.6B**). These differences between linear and nonlinear results for very slow waves are due to

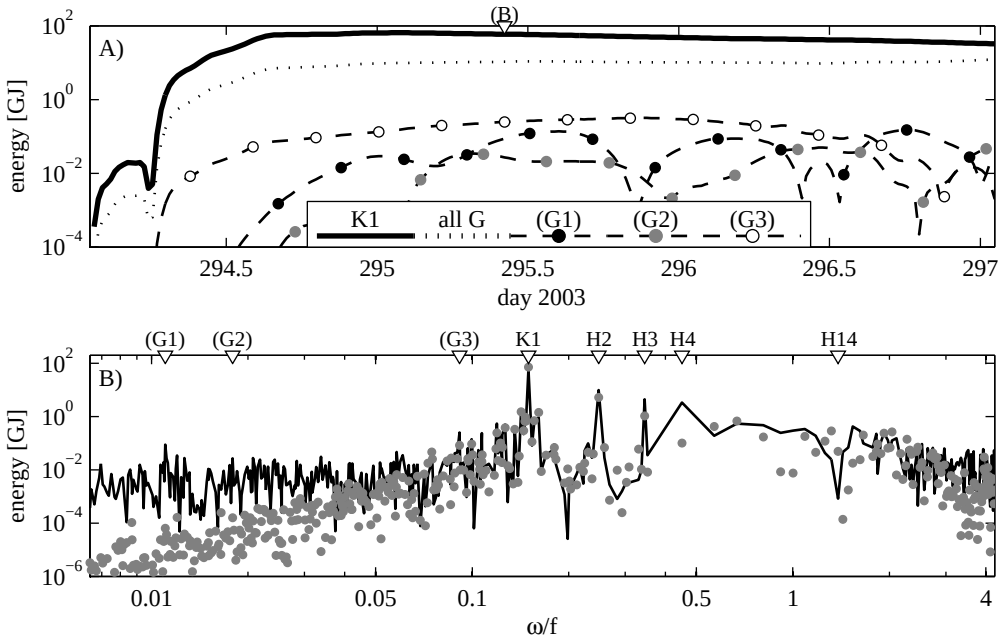

Figure 2.6: (A) Computed timeseries of the energy in specific basin-scale waves. (B) pseudo spectrum for energy contained in basin-scale waves computed by linear model (grey circles) and nonlinear model (solid line), for time (B) marked in (A).

the nonlinear interaction between pairs of gravitational waves. A quasi periodic oscillation of the energy in the selected gyre waves is shown in **Fig. 2.6A**, whose period is small compared with the natural period of the studied gyres, and therefore, cannot be related with nonlinear interactions between pairs of gyre waves.

Kelvin-Poincaré interactions

The fast excitation of high-frequency waves in the southern perimeter of the lake is seen from the nonhydrostatic simulations at early times. **Fig. 2.7A** to **C** show the computed gradient of the interface in the area A1 of **Fig. 2.1A** at three different times during the wind event (indicated in **Fig. 2.7D**), where the generation of a solitary-type wave packages is captured.

The fast excitation quality of the solitary-type waves is remarked as they are generated by the steepening of the Kelvin waves only about 1.5 days after the appearance of the latter waves (see **Fig. 2.5**), and the explanation of this is based on the Kelvin-Poincaré interaction, whose forcing frequency is larger than the forcing frequency of the Kelvin-Kelvin interaction. Thus, down-scale energy transfer due to Kelvin-Poincaré interaction is faster than the Kelvin-Kelvin energy transfer. In fact, the ratio between T_s and T_i of Eq. 2.2 is 0.5, and if T_i is estimated as the Kelvin period (de la Fuente *et al.*, 2008), the timescale of front formation results to be about 2 days, which fits the timescale of formation of solitary-type waves due to the Kelvin wave steepening predicted by the nonhydrostatic model. Here we denote Poincaré

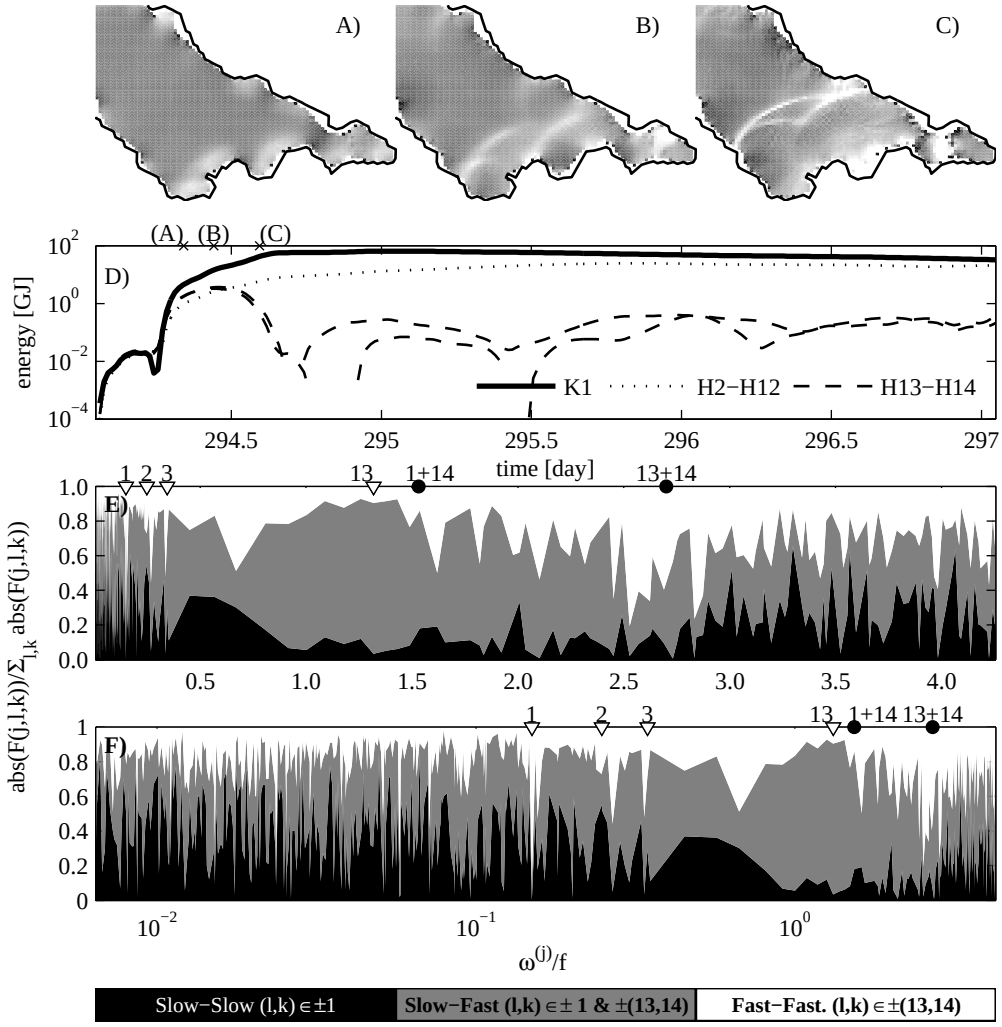

Figure 2.7: (A-C) Frames of the gradient of the interface for marked times in upper axis of (D). (D) Timeseries of the energy in specific basin-scale waves. (E-F) Modulus of normalized energy fluxes computed based on Eq. 2.31, as function of the natural frequency of basin-scale waves, due to interaction between pairs of waves. (E-F) show the same values in different x-scale.

waves the first two modes that present similar rotating flow velocities in the central area of the lake (H13 and H14, $\omega^{(13)} = 1.32f$ and $\omega^{(14)} = 1.38f$, respectively), but they present 13 and 14 peaks in the interface displacement, and not just one as in flat circular basins (Stocker & Imberger, 2003).

Fig. 2.7D shows the timeseries of the energy in K1 (dark solid line), in the two Poincaré waves (H13 and H14, dashed line), and the total energy contained in modes H2 to H12. The wind excitation of the Poincaré waves is reproduced in linear and nonlinear simulations. Because of the natural periods of modes H13 and H14 (0.51 and 0.49 days, respectively) are comparable with the wind duration, the excitation and later cancellation of these waves is readily explained in terms of energy exchanges between the wind and the waves (Shimizu *et al.*, 2007; de la Fuente *et al.*, 2008).

At time (B) of **Fig. 2.7D**, the rate of change of the energy in all of the basin-scale waves due to the nonlinear interactions among H1, H13 and H14 were computed based on Eq. 2.31, considering positive and negatives waves (i.e. l and k equal to $\pm(1, 13, 14)$). These values were grouped into three classes denoted slow-slow, fast-slow and fast-fast. The slow-slow class groups the rate of change of the energy due to the K1-K1 interaction, the fast-slow class contains the rate of change of the energy due to the interactions K1-H13 and K1-K14, and the fast-fast class contains the H13-H13, H13-H14 and H14-H14 interactions. The absolute value of these rates of change normalized by the sum of the absolute values of them is shown in **Fig. 2.7E** and **F**, as a function of the natural frequency of all the basin-scale modes (i.e. j in terms of Eq. 2.31). Those figures show the same plot in different scales (arithmetic and logarithmic). The value of the natural frequency for the first three modes (K1, H2 and H3) and the first order forced frequencies (see analysis for Eq. 2.23) are shown in the upper horizontal axis of **Fig. 2.7E** and **F**.

The fast-fast interactions (white colour in **Fig. 2.7E** and **F**) dominate the rate of change of the energy associated with waves with natural frequency close to the forced frequency $\omega^{(13)} + \omega^{(14)}$. Similarly, the fast-slow interactions (grey colour in **Fig. 2.7E** and **F**) dominate the rate of change of energy of waves with natural frequencies closer to $\omega^{(1)} + \omega^{(13)} \approx \omega^{(13)}$, and the slow-slow interactions dominate in natural frequencies closer to $2\omega^{(1)} \approx \omega^{(2)}$ (black colour in **Fig. 2.7E** and **F**). The fast-fast interactions also dominate the rate of transfer of energy for basin-scale waves with natural frequencies closer to K1, however, it must be noticed that in this analysis the energy transfer between K1 and H2, that dominates the Kelvin nonlinear dynamics, is not considered for plotting **Fig. 2.7**.

Besides this, the noisy behaviour shown in **Fig. 2.7E** and **F** indicates that, because of the spatial correlation requirements to determine the energy exchange in the nonlinear analysis, no all of the waves are equally modified by the interaction between two basin-scale waves.

High-frequency waves at the front area

The occurrence of high-frequency waves in the front area and its implication on vertical mixing is discussed as follows. **Fig. 2.8** summarizes the main aspects that are discussed in this section: each column was constructed based on field measurements and numerical results at S5, S11 and S3, left, central and right column, respectively. Each column shows in the first row, vertical profiles of the buoyancy frequency in grey scale computed from field measurements, the estimated interface location by searching per profile the maximum value of N (solid light line) and the interface displacement computed using the nonhydrostatic model (dashed line). Timeseries of the interface depth computed based on measurements were filtered with a moving average technique in a 15 minutes window.

In the second row of each column of **Fig. 2.8**, the computed interfacial pseudo-shear velocity (solid line) and the wind shear velocity (dashed line) are plotted, defining, arbitrarily, the pseudo-interfacial shear velocity as the absolute value of the difference between the upper and lower layer velocity vectors. Third and fourth rows show the wavelet amplitude computed

for the timeseries of the measured vertically integrated potential energy, and the range of analysed periods, indicated in the vertical axis. The results of the wavelet analysis were divided in two groups, because of visualization purposes: between 5 and 15 minutes and between 1 and 3.5 minutes (shown in the third and fourth rows, respectively). The dashed line in the third and fourth rows represents the maximum measured value of the buoyancy frequency, which also was filtered by a moving average every 15 minutes. The fifth row in **Fig. 2.8**, shows the same plots as in the third row, but constructed based on the potential energy simulated with the nonhydrostatic model. Numbers between round brackets in **Fig. 2.8** are used for the analysis presented in the following paragraphs, and lastly, the time of the simulations was adjusted by adding a constant value to each station (between 1 and 2 hours), in order to obtain the same front location than in measurements.

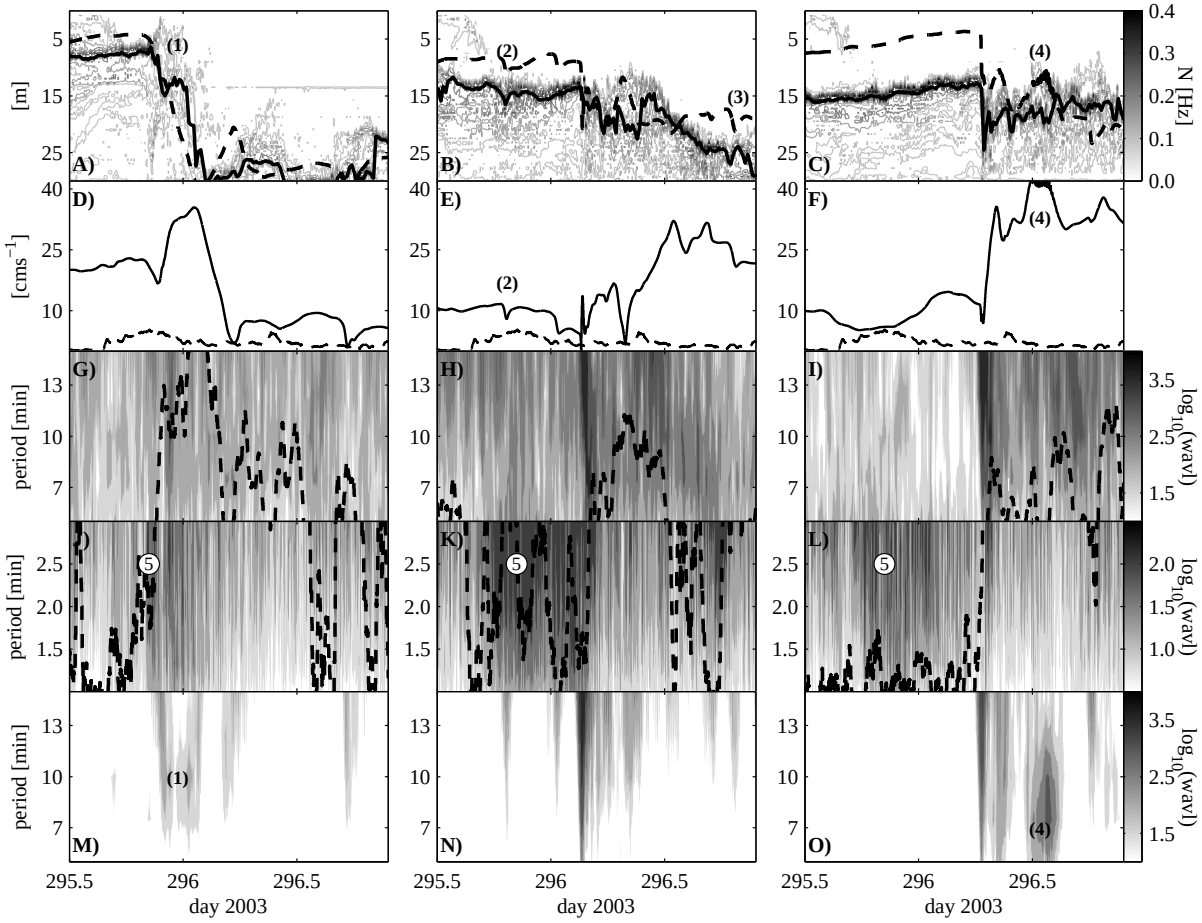

Figure 2.8: Each column show results from S5, S11 and S3, respectively. Upper row show bouyancy frequency (grey scale), computed nonhydrostatic interface displacement (dashed lines) and measured interface displacement (light solid line). Row 2, computed timeseries of shear velocity (solid line) and wind shear velocity (dashed line). Row 3 and 4, wavelet amplitude of the measured potential energy for two period regime, and maximum bouyancy frequency (dashed line). Lower row show the same than row 3 but based on nonhydrostatic simulations.

Although the solitary-type wave train behind the vertical front is well reproduced in the

simulations, with similar amplitude as that observed in the measurements (see **Fig. 2.8N** and **O** and the corresponding panel in the third row), three other examples are presented for validating the nonhydrostatic simulation of the high-frequency waves. First, measurements in S5 show the generation of solitary-type waves at a mid depth of the front (point (1) in **Fig. 2.8A**). The nonhydrostatic simulation shows a similar behaviour but with much less intensity, which can be seeing in the wavelet amplitude of the simulated potential energy (point (1) in **Fig. 2.8M**) that presents a coherent excitation of waves with a period of about 10 minutes. Second, the generation of several vertical fronts was discussed in previous sections. In particular, the front marked between white circles in **Fig. 2.5B** is identified as point (2) in **Fig. 2.8B**, with good agreement between measurements (solid light line) and simulation (dashed line). Third, point (3) in **Fig. 2.8B** marks one of the reflected waves discussed with regards **Fig. 2.5**, and the good correspondence with measurements is also seen.

Several local maxima of the simulated interface displacement (no nonhydrostatic waves), are identified behind the vertical front (**Fig. 2.8A**) and are due to the superposition of several basin-scale waves, but these maxima do not have a clear correspondence with measurements (for instance, point (4) in **Fig. 2.8C**). It is postulated that this difference is due to the erosion of these waves associated with shear instabilities, something that the models used in the present analysis cannot account for. The analysis of the numerical results for S3 (third column) shows the excitation of a localized wave package after one of these local maxima, pointed by (4) in **Fig. 2.8C**, **F** and **O**. This wave package is excited by local supercritical conditions associated to local flow conditions, being the problem similar to that of the transcritical flows analysed by Grimshaw & Smyth (1986) and Melville & Helfrich (1987). In contrast, high flow velocities due to supercritical conditions in viscous flow produces shear instabilities that vertically mix the water column (e.g. Carpenter *et al.*, 2007), which would explain why these waves are not observed in the field measurements. These arguments are complemented by analysing the wavelet amplitude in **Fig. 2.8I**, which shows the presence of excited high frequency waves behind the front. A solitary-type wave train placed behind, and excited by, the front cannot entirely explain **Fig. 2.8I** since it has a limited number of waves and thus, limited length in time (7 solitary-type waves in about 1.5 hours for S3 measurements), being difficult to relate the long term measurements of high-frequency waves of **Fig. 2.8I**, with the nonhydrostatic dynamics at the front position.

The interfacial pseudo-shear velocity plotted with solid lines in **Fig. 2.8D** to **F** can be used to estimate the regions where shear instabilities could produce localized vertical mixing. A arbitrarily reference value of 20 cms^{-1} is defined with this aim, and it is require to remark that this value is only for reference because analysis is incomplete since the excitation of shear instabilities also depends on the viscous layer thickness (e.g. Horn *et al.*, 2001). **Fig. 2.9** shows, in the left column, frames in the area A2 (**Fig. 2.1A**) of the gradient of the interface displacement used to identify the solitary-type waves, and in the right column, both the simulated velocity field of the upper layer and the area where the shear velocity is larger than 20 cms^{-1} (shaded in grey). In **Fig. 2.9**, a circle in the northern perimeter of the lake indicates the front position and the waves indicated with an arrow in **Fig. 2.9C** constitute an example of the supercritical flows areas. Therefore, nonlinear dynamics that explains the

steepening of the Kelvin wave and the subsequently degeneration in solitary-type waves also produces localized high flow velocities behind the front, that induces shear instabilities and localized vertical mixing areas. **Fig. 2.9E** shows the presence of transverse and reflected waves, which could be explained on the basis of front-bathymetry interactions, similar to those marked by (3) in **Fig. 2.8B**.

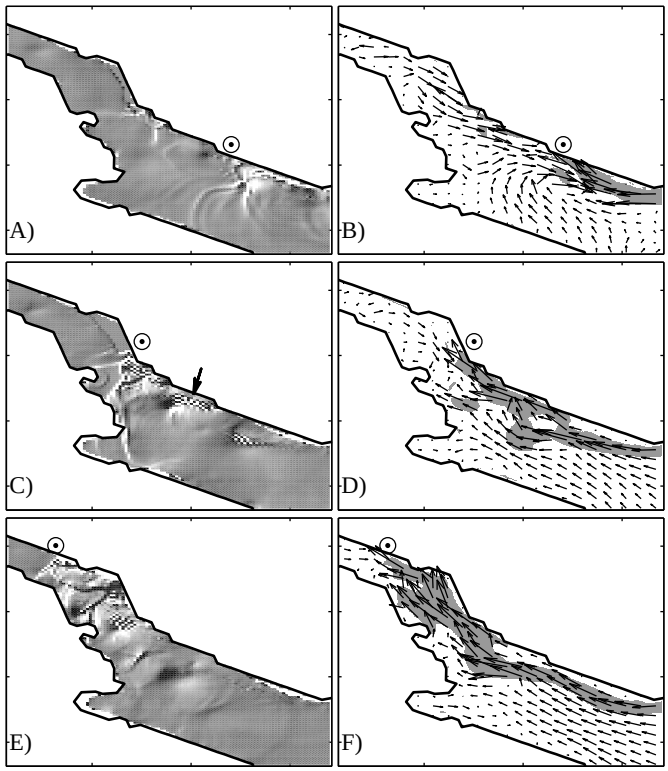

Figure 2.9: Frames of the gradients of the interface displacement (left-hand column) and upper layer flow velocity (right-hand column). Grey regions in right-hand column denote areas with high values of shear velocity.

Finally, comparison between the wind shear velocity in the second row (dashed line) and regions marked as (5) in **Fig. 2.8J**, **K** and **L**, highlight the presence of wind excited high-frequency waves with characteristic period of about 2 minutes (Antenucci & Imberger, 2001*b*; Gómez-Giraldo *et al.*, 2008). Moreover, the waves excited by interfacial shear behind the front have a characteristic period of about 10 minutes, and an incorrect analysis of these results would lead to the wrong conclusion that different mechanisms (wind shear and interfacial shear) excite waves with different characteristic period. However, observed temporal changes in the buoyancy frequency (dashed line in **Fig. 2.8G** to **L**) show that the link between excitation mechanism and characteristic period does not seem to exist as the buoyancy frequency during the second wind event (see points (5) in fourth row and dashed line in second row) was larger than the buoyancy frequency behind the front.

Energy partitioning

Based on the reasonably accurate representation of the solitary-type waves of the nonhydrostatic simulations, the available potential energy contained in the high-frequency waves is estimated from the simulations following two methods: by filtering in space the available potential energy, or by filtering in space the interface displacement to estimate then the total available potential energy contained in the high-frequency waves. The spatial filter used with this aim corresponds to averaging the numerical results for interface displacement obtained in the 30 m numerical mesh over a coarse grid of 630 m, and to linearly interpolate the averaged results back to the 30 m mesh. The difference between these two surfaces indicates, then, the available potential energy or interface displacement contained on waves shorter than 630 m. The same procedure can be used to estimate the kinetic energy but the obtained results are influenced by the lake bathymetry, and do not gives the correct energy contained in the high-frequency waves. Finally, this spatial filter is equivalent to filtering waves with period larger than about 30 minutes, travelling at $c_o = 30\ cms^{-1}$ with $\bar{h}_2 = 147$ m.

Fig. 2.10A shows timeseries of the total available potential and kinetic energy partitioning computed based on nonhydrostatic simulations (light grey and dark grey, respectively), and the wind given energy (dashed line). **Fig. 2.10B** shows the timeseries of available potential energy in the high-frequency waves estimated by filtering the potential energy (solid line) and by filtering the interface displacement (dashed line).

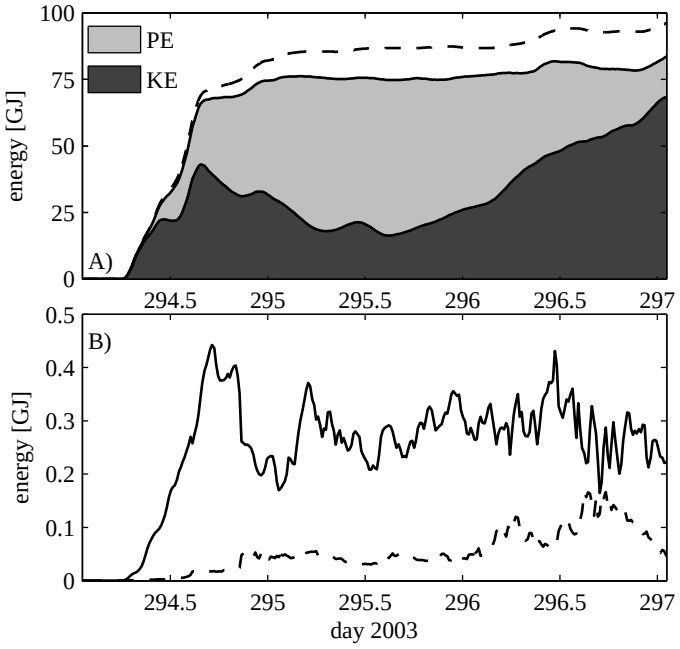

Figure 2.10: (A) Timeseries of total kinetic and available potential energies. (B) Timeseries of potential energy contained in solitary-type waves, estimated by filtering the available potential energy (solid line) and by filtering the interface displacement (dashed line).

It was found (**Fig. 2.4A**) that in this system the energy radiated from the Kelvin wave

K1 down to the other gravitational waves represents about 50% of the total wind-given energy. However, **Fig. 2.10B** shows that the energy contained in the solitary-type waves is less than 1% of the total wind-given energy. The apparent contradiction between **Fig. 2.4A** and **2.10B** is explained in the analogy between the modal analysis and the Fourier transform of a step function, which shows that some of the energy radiated from the Kelvin wave has gone to basin-scale waves that simply draw the steepening (Boegman *et al.*, 2005*b*; de la Fuente *et al.*, 2008), and do not really belong to the range of high-frequency waves.

Fig. 2.10A shows the gradual radiation from available potential energy to kinetic energy after about $t = 295.5$, and by the end of the nonhydrostatic simulations, when the front arrives to the north end of the lake, the potential energy represents about the 15% of the total energy. This description fits the free oscillation pattern of the 1D problem in a closed rectangular channel (Horn *et al.*, 2001), and cannot be related with the excitation of purely kinetic energy gyre waves, because the nonhydrostatic model cannot deal with these waves.

Discussion

LDS measurements in **Fig. 2.2** showed the occurrence of an incident wave to Lake Überlingen of about 15 m of amplitude, however it is difficult to identify the reflected wave in the temperature records. This shows the dissipation of a large amount of the basin-scale wave energy in about 2 days. Unfortunately, the lack of spatial resolution of LDS measurements precludes estimating the energy contained in the residual basin-scale wave field as Shimizu & Imberger (2008) did.

Different damping mechanisms that act to dissipate the energy contained in the internal wave field were discussed in the introduction, and the direct interpretation of them leads to the conclusion that nonlinear phenomena that transfer energy from the basin-scale waves down to the solitary-type wave scales dominates the wave dynamics in Lake Constance. Subsequently, solitary-type wave breaking in shallow areas of the northern basin of the lake should dissipate the energy given by the wind (Vlasenko & Hutter, 2002; Boegman *et al.*, 2005*a*).

However, the energy contained in the simulated solitary-type waves does not support the described energy path. At laboratory scale the energy of the solitary-type waves is about 10% of the total available potential energy (Boegman *et al.*, 2005*a*). For a small circular flat basin, de la Fuente *et al.* (2008) showed that the energy of the solitary-type waves is about 25% of the total energy. On the other hand, Gómez-Giraldo (2007) estimated the energy in the high-frequency waves in Lake Constance, including the shear instabilities, in about 5% of the total wind-given energy. These values cannot entirely explain the measured dynamics shown in **Fig. 2.2**, and this argument is reinforced if it is considered that between 10 and 75% of the energy in the solitary-type waves is actually dissipated by breaking (Boegman *et al.*, 2005*a*), and the remanent energy is reflected as long waves. Arguments, such as the continuous solitary-type waves emergence and their subsequent breaking, can help to deal with the contradiction between the results presented here and the conceptual model discussed in the introduction,

however, that argument neglects the fact that the solitary-type waves emerge only after a characteristic time, usually large.

Fig. 2.10A support the argument that bottom friction is the damping mechanism that primarily accounts for the dissipation of the energy contained on the basin-scale waves in Lake Constance. Nonlinear wave dynamics produces localized events such as wave steepening and the subsequent generation of solitary-type waves and high flow velocity areas. Consequently, bottom friction damping acts in localized areas of the lake too, not showing the whole basin feature described by Shimizu & Imberger (2008) for a shallow linear lake.

Finally, throughout the present analysis the background potential energy have been considered constant. The background potential energy is the potential energy of the system at rest that do not induce movement (Antenucci *et al.*, 2000). Nevertheless, LDS measurements show that the characteristic density step varies in about 3% per day, which is equivalent to a difference between the background potential energy at the beginning and at the end of the simulations of about 30 GJ, while the total wind-given energy is of about 90 GJ. Therefore the basin-scale dynamics in a variable background potential energy should be included in future analyses, to test whether the interpretation of the energy paths proposed here, in terms of the importance of bottom friction with respect to energy dissipation in solitary-type waves, is reasonable for large and deep lakes, or it is just a coincidence or wrong interpretation of the results presented here.

References

Antenucci, J. & Imberger, J. 2001*a* Energetics of long internal gravity waves in large lakes. *Limnol. Oceanogr.* **46**, 1760 – 1773.

Antenucci, J. & Imberger, J. 2001*b* On internal waves near the high-frequency limit in an enclosed basin. *J. Geophys. Res.* **106**, 22465 – 22474.

Antenucci, J., Imberger, J. & Saggio, A. 2000 Seasonal evolution of the basin-scale internal wave field in a large stratified lake. *Limnol. Oceanogr.* **45**, 1621 – 1638.

Appt, J., Imberger, J. & Kobus, H. 2004 Basin-scale motion in stratified upper lake constance. *Limnol. Oceanogr.* **49**, 919 – 933.

Baines, P. G. 1998 *Topographic effects in stratified flows.* Cambridge University Press.

Boegman, L., Imberger, J., Ivey, G. & Antenucci, J. 2003 High-frequency internal waves in large stratified lakes. *Limnol. Oceanogr.* **48**, 895 – 919.

Boegman, L., Ivey, G. & Imberger, J. 2005*a* The degradation of internal waves in lakes with sloping topography. *Limnol. Oceanogr.* **50**, 1620 – 1637.

Boegman, L., Ivey, G. & Imberger, J. 2005*b* The energetics of large-scale internal wave degeneration in lakes. *J. Fluid. Mech.* **531**, 159 – 180.

Botelho, D. & Imberger, J. 2008 Downscaling model resolution to illuminate the internal wave field in a small stratified lake. *J. Hydr. Res.* **133**, 1206 – 1218.

Carpenter, J. R., Lawrence, G. A. & Smyth, W. D. 2007 Evolution and mixing of asymmetric holmboe instabilities. *J. Fluid. Mech.* **582**, 103 – 132.

Choi, W. & Camassa, R. 1999 Fully nonlinear internal waves in two-fluid system. *J. Fluid. Mech.* **396**, 1 – 36.

Csanady, G.T. 1968 Motions in a model great lake due to suddenly imposed wind. *J. Geophys. Res.* **73**, 6435–6447.

Farmer, D. M 1978 Observations of long nonlinear internal waves in a lake. *J. Phys. Oceanogr.* **8**, 63 – 73.

Fischer, H., List, R., Imberger, J. & Brooks, N. 1979 *Mixing in Island and Coastal Waters.* Academic Press.

de la Fuente, A., Shimizu, K., Imberger, J. & Niño, Y. 2008 The evolution of internal waves in a rotating, stratified, circular basin and the influence of weakly nonlinear and nonhydrostatic accelerations. *Limnol. Oceanogr.* **53**, 2738 – 2748.

Gómez-Giraldo, E. A. 2007 *Observation of energy flux mechanisms associated with internal waves.*. PhD thesis University of Western Australia.

Gómez-Giraldo, E. A., Imberger, J., Antenucci, J. & Yeates, P. 2008 Wind-shear-generated high-frequency internal waves as precursors to mixing in a stratified lake. *Limnol. Oceanogr.* **53**, 354 – 367.

Grimshaw, R. H. J. & Smyth, N. 1986 Resonant flow of a stratified fluid over topography. *J. Fluid. Mech.* **169**, 429 – 464.

Hammack, J. L. & Henderson, D. M. 1993 Resonant interactions among surface water waves. *Annu. Rev. Fluid Mech.* **25**, 55 – 97.

Helfrich, K. 2007 Decay and return of inertial solitary waves with rotation. *Phys. Fluids.* **19**, 026601, doi: 10.1063/1.2472509.

Helfrich, K. & Melville, W. K. 1986 On long nonlinear internal waves over slope-shelf topography. *J. Fluid. Mech.* **167**, 285 – 308.

Horn, D.A., Imberger, J. & Ivey, G. 2001 The degradation of large-scale interfacial gravity waves in lakes. *J. Fluid. Mech.* **434**, 181 – 207.

Horn, W., Mortimer, C.H. & Schwab, D. J. 1986 Wind-induced internal seiches in lake zurich observed and modeled. *Limnol. Oceanogr.* **31**, 1232 – 1254.

Imberger, J. & Hamblin, P. 1982 Dynamics of lakes, reservoirs, and cooling ponds. *Annu. Rev. Fluid Mech.* **14**, 153 – 187.

Kocsis, O., Mathis, B., Gloor, M., Schurter, M. & Wüest, A. 1998 Enhanced mixing in narrows:

A case study at the mainau sill (lake constance). *Aquat. Sci.* **60**, 236 – 252.

Lorke, A., Peeters, F. & Bäuerle, E. 2006 High-frequency internal waves in the litoral zone of large lake. *Limnol. Oceanogr.* pp. 1935 – 1936.

Marti, C. J. & Imberger, J. 2006 Dynamics of the benthic boundary layer in a strong forced stratified lake. *Hydrobiologia* **568**, 217 – 233.

Melville, W. K. & Helfrich, K. 1987 Transcritical two-layer flow over topography. *J. Fluid. Mech.* **178**, 31 – 52.

Melville, W. K., Tomasson, G. G. & Renouard, D. P. 1989 On the stability of kelvin waves. *J. Fluid. Mech.* **206**, 1 – 23.

Miles, J. W. 1980 Solitary waves. *Annu. Rev. Fluid Mech.* **12**, 11 – 43.

Mortimer, C.H. 1952 Water movement in lakes during summer stratification; evidence from the distribution of temperature in windermere. *Phil. Trans. R. Soc. Lond. B* **236**, 355 – 398.

Peeters, F., Straile, D., Lorke, A. & Ollinger, D. 2007 Turbulent mixing and phytoplankton spring bloom development in a deep lake. *Limnol. Oceanogr.* **52**, 286 – 298.

Phillips, O. M. 1966 The dynamics of the upper ocean. .

Shimizu, K. & Imberger, J. 2008 Energetics and damping of basin-scale internal waves in a strongly stratified lake. *Limnol. Oceanogr.* **53**, 1574 – 1588.

Shimizu, K., Imberger, J. & Kumagai, M. 2007 Horizontal structure and excitation of primary motion in a strongly stratified lake. *Limnol. Oceanogr.* **52**, 2641 – 2655.

Stocker, R. & Imberger, J. 2003 Energy partitioning and horizontal dispersion in a stratified rotating lake. *J. Phys. Oceanogr.* **33**, 512 – 529.

Thompson, R. & Imberger, J. 1980 Response of a numerical model of a stratified lake to wind stress. IIth International Symposium of Stratified Flows.

Thorpe, S. A. & Hall, J. 1974 Evidence of kelvin-helmholtz billows in loch ness. *Limnol. Oceanogr.* pp. 973 – 976.

Toro, E.F. 1997 *Riemann Solvers and Numerical Methods for Fluid Dynamics.*. Springer Verlag, New York.

Van Dyke, M. 1975 *Perturbation Methods in Fluid Mechanics.*. Academic Press.

Vlasenko, V. & Hutter, K. 2002 Transformation and disintegration of strongly nonlinear internal waves by topography in stratified lakes. *Ann. Geophys.* **20**, 2087 – 2103.

Wang, Y., Hutter, K. & Bäuerle, E. 2000 Wind-induced baroclinic response of lake constance. *Ann. Geophys.* **18**, 1488 – 1501.

Wüest, A. & Lorke, A. 2003 Small-scale hydrodynamics in lakes. *Annu. Rev. Fluid Mech.* **35**, 373–412.

Wüest, A., Piepke, G. & Van Senden, D. 2000 Turbulent kinetic energy balance as a tool for estimating vertical diffusivity in wind-forced stratified waters. *Limnol. Oceanogr.* **45**, 1388 – 1400.

Concluding remarks

Within timescales of days, stratified lakes dynamics is governed by mechanical energy exchanges between the wind and the lake that excite the basin-scale waves in the lake. Under a linear approach, the shape of the basin-scale waves shows coherent dynamics in the whole basin, and the excitation of a particular basin-scale depends on its upper layer flow velocity and the relative wave phase with respect to the wind. These requirements produce that one basin-scale wave may be excited or cancelled by the wind action, depending on whether the wind does work on the waves, or the flow does work against the wind.

The linear solution for the initial value problem gives pure rotation of the waves without changes of its energy. In contrast, the wind forced problem shows the periodic wind-excitation or cancellation of the basin-scale waves within one natural period of the waves. This is a common feature in rotating and nonrotating basins; however, the natural frequency of the rotating basin-scale waves are not entire multiple of the fundamental mode frequency, and then, the flow in rotating basins is characterized by the periodic emergence of several local maxima of the interface displacement when pair of waves are in phase.

Nonetheless, any linear perturbation becomes essentially nonlinear after some time. The time when the flow turns nonlinear is characterized by the steepening formation time. The simplest way to understand this time is by analysing the spatial changes of the wave celerity, which is no longer homogeneous when nonlinear terms are included in the analysis, and the steepening formation time arises from imposing that faster regions of the wave reach the slower regions. It was shown that for closed basins, the ratio between the steepening formation time and the internal period, describes how fast the nonlinearities emerge with respect to the timescale that characterizes, for example, the energy exchanges with the wind, or the damping timescale, which also can be characterized by the internal period.

On the other hand, the analysis of the evolution of basin-scale waves showed that Kelvin waves evolve through radiating energy down to its higher azimuthal modes, which produces wave steepening and subsequent emergence of quasi-permanent solitary-type waves, showing a dynamics similar than that for nonrotating basins. In contrast, the evolution of Poincaré waves showed the periodic energy radiation to-from other basin-scale waves with a period of about 1.5 times the natural period of the Poincaré waves. This different dynamics showed that the principal damping mechanism is basin-scale waves dependent: while the Kelvin wave constantly radiates energy to faster and smaller modes arriving down to the nonhydrostatic flow scales, energy in Poincaré waves can only be dissipated by bottom friction. Furthermore, when both Kelvin and Poincaré waves are equally important, the coupled dynamics is characterized by the superposition of the parent waves dynamics, plus the nonlinear interaction between them, which produces the excitation of smaller waves.

These general features are helpful to explain the measured dynamics in Lake Constance: first,

the wind excites the basin-scale waves and, because of the Earth rotation, the maximum interfacial displacement is located in a rotated direction with respect to the wind direction. The energy in the Kelvin wave contains most of the total wind-given energy, and the evolution of this wave is well described by its steepening, due to radiation to higher modes, and subsequent emergence of solitary-type waves. Second, Kelvin-Poincaré interactions are also presented in Lake Constance. The Poincaré waves are also excited by the wind; however, the wind duration is of about the natural period of these waves, and the periodic wind-excitation and subsequent wind-cancellation explains the Poincaré waves dynamics. While the energy on Poincaré waves exists, Kelvin-Poincaré interactions radiate energy down to smaller scales of the flow, resulting in the excitation of a solitary-type wave train.

The essentially nonlinear and nonhydrostatic dynamics in Lake Constance modifies the whole basin coherent structure of the linear basin-scale waves, into a flow characterized by localized events of: wave steepening, large flow velocity, and, eventually, transcritical flows. These general features provide the essential elements to sketch the role of each damping mechanism of the basin-scale waves and its consequences on vertical mixing: i) large flow velocity areas were related with shear instability or transcritical flows in the lake interior that produce localized mixing. ii) Solitary-type wave excitation and breaking were identified as an important mechanism that induces localized mixing; however, the energy contained on the solitary-type waves estimated from the simulations does not support their effectiveness in dissipating the energy input from the wind. It was speculated then that, even for a highly nonlinear flow, the energy dissipation in the lake would be mainly due to bottom friction, while nonlinearities of the flow induce mostly localized vertical mixing and rather small energy dissipation compared with the corresponding input from the wind.

Appendixes

By N-Layers, a 2D multilayers model for natural stratified flows.[†]

Abstract

A numerical model has been developed for studying the hydrodynamics of natural stratified flows, considering the coupling of 2, 3, or more, vertically homogeneous layers of horizontally variable thickness. In each layer, 2-D, layer-averaged versions of density-coupled continuity, mass, and momentum transport equations, including Coriolis force terms, are applied. Vertical coupling among neighbour layers is achieved using the kinematic boundary condition and hydrostatic pressure distribution. The system of coupled equations is solved numerically, using an adaptation of the finite volume MUSCL-Hancock method. The numerical model is able to capture linear and nonlinear internal waves and allows for a much better resolution of picnoclines than fixed grids used in traditional 3D modelling approaches. Validation of the numerical model is presented and discussed, comparing numerical results with analytical solutions and experimental results of benchmark tests, including estimating periods of internal waves, internal response due to surface stress, and shape of salt wedge.

Introduction

First conceptual models for understanding the dynamics of a stratified water body vertically subdivided it in two or three layers (Monismith, 1985). At present, several numerical models that successfully resolve the vertical structure of stratified water bodies have been developed in 1D (e.g., DYRESM, Spigel & Imberger, 1980), 2D (e.g., CE-QUAL W2, Cole & Wells, 2003) o 3D (e.g., ELCOM, Hodges *et al.*, 2000). The existence of these powerful models may suggest that a conceptual division of the water column in 2 or 3 layers is obsolete. Nonetheless, recent experimental and theoretical studies, focused on understanding the internal dynamics of stratified water bodies, have used a 2-layer conceptual model for testing hypotheses or developing theory (e.g. Antenucci & Imberger, 2001; Horn *et al.*, 2002). From this point of view multi-layer models can provide insight on physical processes occurring in natural systems and they are an alternative simulation tool to 1D and fully 3D models. In this paper a novel numerical model is presented, named *by n-Layers*, which solves the dynamics of n vertically coupled layers in an irregular 2D mesh, including bathymetry. The numerical scheme is based on the MUSCL-Hancock method for hyperbolic equations (e.g. Bradford *et al.*, 1997; Loose *et al.*, 2005). Applications to six benchmark problems are presented, with the aim of validating different aspects of the numerical model in 2 and 3 layers.

[†]de la Fuente, A., Niño, Y., Muñoz, R. and Frederick, R., 2006. By N-Layers, a 2D multilayers model for natural stratified flows. *VI International Symposium on Stratified Flow.* Perth, Australia.

Governing equations and numerical method

By integrating the Reynolds averaged equations between $z = z_{i+1}$ and $z = z_i$ (see **Fig. A1**), considering boundary layer and hydrostatic pressure approximations, the governing equations for the i^{th} layer, with $i = 1 \dots n$, are obtained. These equations are written in conservative form as:

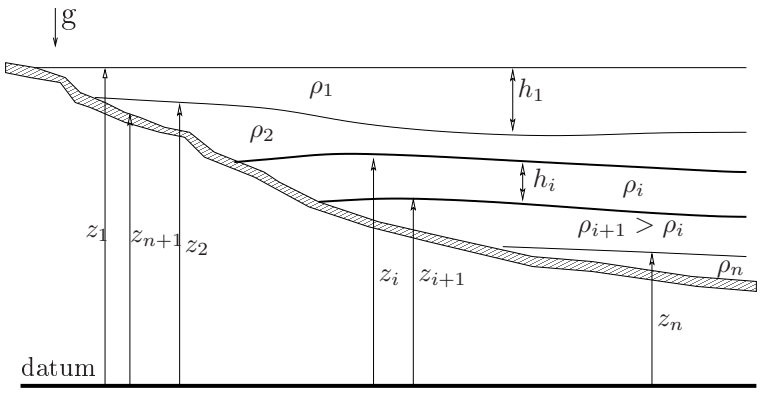

Figure A1: Schematic of water body with n layers of variable thickness.

$$\frac{\partial \vec{U_i}}{\partial t} + \frac{\partial \vec{F_i^x}}{\partial x} + \frac{\partial \vec{F_i^y}}{\partial y} = \vec{H_i} \tag{A1}$$

With

$$\vec{U_i} = [h_i, u_i h_i, v_i h_i]^T \tag{A2a}$$

$$\vec{F_i^x} = \begin{bmatrix} u_i h_i \\ u_i\, u_i h_i + g\frac{\rho_i}{\rho_o}\frac{h_i^2}{2} + h_i\frac{p_i^{sup}}{\rho_o} \\ u_i\, v_i h_i \end{bmatrix} \quad ; \quad \vec{F_i^y} = \begin{bmatrix} v_i h_i \\ v_i\, u_i h_i \\ v_i\, v_i h_i + g\frac{\rho_i}{\rho_o}\frac{h_i^2}{2} + h_i\frac{p_i^{sup}}{\rho_o} \end{bmatrix} \tag{A2b}$$

$$\vec{H_i} = \frac{1}{\rho_o}\begin{bmatrix} 0 \\ p_i^{sup}\frac{\partial z_i}{\partial x} - (p_i^{sup} + \rho_i g h_i)\frac{\partial z_{i+1}}{\partial x} + \tau_{xz}(z_i) - \tau_{xz}(z_{i+1}) + \rho_o f\, v_i h_i \\ p_i^{sup}\frac{\partial z_i}{\partial y} - (p_i^{sup} + \rho_i g h_i)\frac{\partial z_{i+1}}{\partial y} + \tau_{yz}(z_i) - \tau_{yz}(z_{i+1}) - \rho_o f\, u_i h_i \end{bmatrix} \tag{A2c}$$

Where ρ_i, u_i and v_i are the layer averaged density and velocities in x and y directions, respectively. $\vec{U_i}$ denotes the vectors of the so called conservative variables, $\vec{F_i^x}$ and $\vec{F_i^y}$ denote the vectors of volume and momentum fluxes in x and y directions, respectively, and $\vec{H_i}$ denotes the source terms vectors. z_i denotes the interfaces elevations, where z_1 denotes the free surface elevation and z_{n+1} the bottom elevation. τ_i and τ_{i+1} are the interfacial shear stresses, f the Coriolis parameter and p_i^{sup} the pressure at the top layer interface ($z = z_i$), which is, according to the hydrostatic pressure law, equal to,

$$p_i^{sup} = \begin{cases} 0 & \text{para } i = 1 \\ \sum_{j=1}^{i-1} \rho_j g h_j & \text{para } i > 1 \end{cases} \tag{A3}$$

Finally, the n layers dynamics is represented by a set of $3 \times n$ equations, written in general form as:

$$\frac{\partial \vec{U}}{\partial t} + \frac{\partial \vec{F}_x}{\partial x} + \frac{\partial \vec{F}_y}{\partial y} = \vec{H} \tag{A4}$$

Numerical Schema

The numerical model developed to solve Eq. A4 is based on MUSCL-Hancock method for hyperbolic equations, with a predictor step for momentum and volume transport equations, based upon equations (A1), and a corrector step, which integrates the k^{th} equation of (A4) over the finite volume cells. The latter procedure yields that temporal changes of U are due to fluxes perpendicular to cell faces c ($F_{k,\perp}(c)$) and the source terms. For more details see Bradford *et al.* (1997) and Loose *et al.* (2005).

To solve the advective fluxes at cell faces ($F_{k,\perp}(c)$), MUSCL-Hancock method uses an extrapolation of primitive variables (h_i, u_i, v_i) from nodes to these faces. With this extrapolation, two characteristic values of U, and so of $F_{k,\perp}(c)$, are obtained: internal values U_k^{int} and $F_{k,\perp}^{int}$, which come from P to c extrapolation, and external values, U_k^{ext} and $F_{k,\perp}^{ext}$, which come from neighbour node C to face c extrapolation. Using Nujic's (Nujic, 1995) modified Lax-Friedrichs approximation for the Jacobian matrix, the advective fluxes at face c are:

$$F_{k,\perp}(c) = \frac{1}{2}\left(F_{k,\perp}^{int} + F_{k,\perp}^{ext} - \kappa_c \left(U_k^{ext} - U_k^{int}\right)\right) \tag{A5}$$

where $\kappa_c = \max|\hat{\lambda}_i|$. Here, $\lambda_i =$ are the eigenvalues of the Jacobian of $\vec{F}_{\perp,i} = (\vec{F}_i^x, \vec{F}_i^y) \cdot \hat{n}_c$, equal to:

$$\lambda_i = \left[u_{i\perp}, u_{i\perp} \pm \sqrt{p_i^{sup} + g\frac{\rho_i}{\rho_o} h_i}\right] \tag{A6}$$

where $u_{i\perp}$ is the flow velocity perpendicular to face c. It is assumed, for simplicity, that the hyperbolic character of the governing equations for the i^{th} layer is represented only with these 3 governing equations, instead of the entire system of $3 \times n$ equations.

Results

Six different modelling exercises are presented here, with the aim of validating the numerical model developed. They cover different problems in stratified flows. Exercise (i) considers the response of a 2-layer stratified basin to surface shear stress. **Fig. A2A**. shows a comparison between the interfacial slope predicted by the model and the corresponding theoretical value expressed in terms of the inverse of the Richardson number of the flow (more details in Spigel & Imberger, 1980). For exercise (ii) the spectral energy associated with free internal seiches in a 2-layer stratified basin computed with the model was used to establish dominant frequencies. Those frequencies were compared in **Fig. A2B**. with corresponding normal mode oscillation frequencies (Spigel & Imberger, 1980). An arrested salt wedge was considered for exercise (iii). **Fig. A2C**. compares the wedge shape predicted by the model with the theoretical solution given by (Schijf & Schonfeld, 1953). Exercise (iv) aims at validating the simulated dynamics of a rotating basin. **Fig. A2D**. shows frequency spectral packs associated to Kelvin and Poincarï¿½ waves predicted by the model, together with results of the dispersion relation found analytically by Antenucci & Imberger (2001), in terms of the Burger number. To validate the ability of the model to capture nonlinear behavior, the experiment of Horn *et al.* (2002) was simulated (exercise v). Measured time series of interface elevations of the soliton generated in the laboratory channel are compared with model equivalent results in **Fig. A2E**. Finally, in exercise vi) the internal dynamics of a 3-layers basin simulated with the model was compared with theoretical predictions by (Monismith, 1985), who showed that values of the parameter $\delta = \frac{\beta_2}{\beta_3}$ define whether the basin response is mode 1 or 2. β_2 and β_3 are defined as:

$$\beta_2 = \sqrt{\frac{g\Delta\rho_{12}h_1}{\rho_o}} \;\; ; \;\; \beta_3 = \sqrt{g\frac{\Delta\rho_{23}}{\rho_o}\frac{h_2h_3}{(h_1+h_2+h_3)}} \tag{A7}$$

The numerical exercise considers that the 3-layer water body was perturbed by the application of a surface shear stress of short duration. For each layer, the temporal mean value of the spatial standard deviation of layer thickness (σ_i) was calculated, and the normalized value of σ_i, defined as: $\overline{\sigma_{h_i}} = \frac{\sigma_i}{\sum_{j=1}^{3}\sigma_j}$, is interpreted as the relative importance of the i^{th} layer on the dynamics of the water body. If $\overline{\sigma_{h_i}}$ is close to 0, this layer behaves more as a interface than as a layer, and the opposite is true for large values of this parameter. Results of the simulations obtained for different values of the surface shear stress, layers thickness, and densities of the intermediate layer are presented in **Fig. A2F**.

Discussion and Conclusions

The exercises presented here successfully validate the proposed model on most important topics on internal dynamics of stratified water bodies. It is concluded that this model is useful for understanding the large-scale dynamics of such water bodies. The exercises were selected as to cover the main forcing agents of these water bodies.

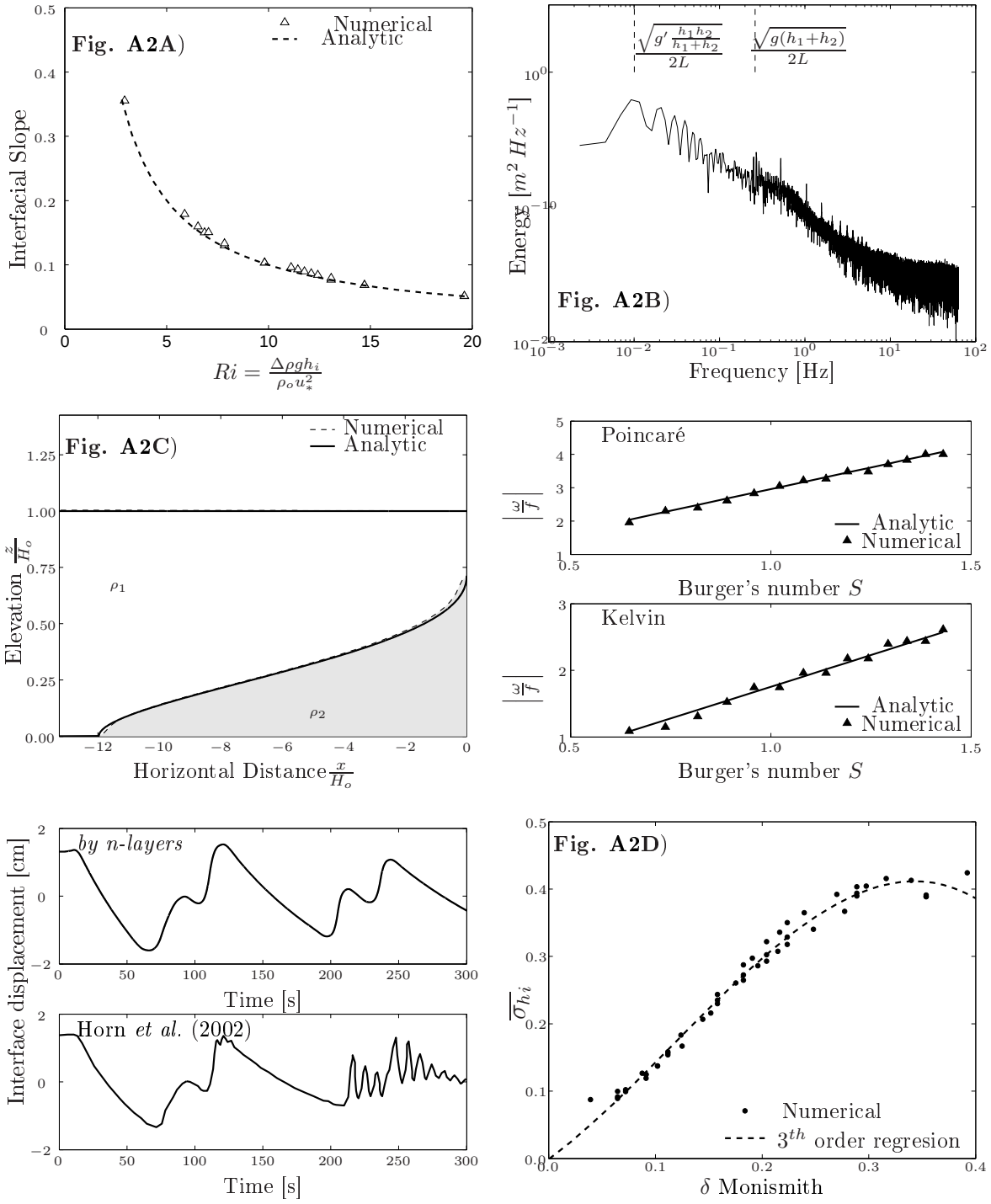

Figure A2: Numerical exercises for validating different aspects of *by n-layers* model. (A) Interfacial steady response to a surface shear stress, (B) seiching spectral dynamics in a 2-layers water body, (C) arrested salt wedge, (D) rotating basin dynamics, (E) internal non-linear wave dynamics, and (F) hydrodynamics of a 3-layers basin.

The ability of the model to handle open boundaries and the influence of water flows in the

stratification was tested in the salt wedge exercise. The simulated wedge profile is very close to the theoretical one given by (Schijf & Schonfeld, 1953). Some negligible differences exist in the region of high horizontal gradients (**Fig. A2C**).

Wind induced surface shear stress over a stratified lake is balanced by a horizontal pressure gradient. The resulting steady state condition is well represented by the model (**Fig. A2A**). When wind stops, free internal oscillation of the water volume sets in. The simulated spectra of this seiching motion shows that most of the energy is contained around the theoretical normal oscillation modes (**Fig. A2B**).

In the case of a large water body, where earth rotation affects the internal dynamics, Kelvin and Poincaré waves are generated, which contain most of the energy. This behaviour was well represented by the model, and the theoretical dispersion relationship for these rotating waves is accurately reproduced numerically (**Fig. A2D**).

In the exercise aimed at validating the non-linear wave dynamics predicted by the model, a good agreement with experimental results was obtained but only for the long-waves. The higher frequency waves observed experimentally are not represented by the numerical simulations (**Fig. A2E**). This may be related with the inability of the model to reproduce 3D effects, particularly related with non-hydrostatic processes. Also the filtering out of the higher frequency waves by the model seem to be related with the properties of the numerical scheme, which tend to eliminate instabilities about sharp fronts. Despite this, the model does a very good job in reproducing most of the energy of the internal waves, as the long waves represent about 90% of the entire spectrum.

Finally, the simulation of 3-layers dynamics shows that Monismith's δ is indeed the parameter that governs the internal response. For values of δ close to 0, the intermediate layer is not involved in the internal force balance, and mode 1 response occurs. For larger values of δ the importance of this layer on the internal dynamics increases, and a mode 2 response takes place (**Fig. A2F**).

The results presented suggest that *by n-layers* is a useful tool for understanding the long internal dynamics of a natural stratified water body, which may be conceptually simulated in 2 or 3 layers.

References

Antenucci, J. & Imberger, J. 2001 Energetics of long internal gravity waves in large lakes. *Limnol. Oceanogr.* **46**, 1760 – 1773.

Bradford, S., Katopodes, N. & Parker, G. 1997 Characteristic analysis of turbid underflows. *J. Hydr. Eng.* **123**, 420 – 431.

Cole, T. & Wells, S. 2003 *CE-QUAL-W2: A Two-Dimensional, Laterally Averaged, Hydrodynamic and Water Quality Model, Version 3.1.*. Department of Civil and Environmental Engineering. Portland State University.

Hodges, B., Imberger, J., Saggio, A. & Winters, K. B. 2000 Modeling basin-scale waves in stratified lakes. *Limnol. Oceanogr.* **45**, 1603–1620.

Horn, D.A., Imberger, J., Ivey, G. & Redekopp, L.G. 2002 A weakly nonlinear model for long internal waves in closed basins. *J. Fluid. Mech.* **467**, 269 – 287.

Loose, B., Niño, Y. & Escauriaza, C. 2005 Finite volume modeling of variable density shallow-water equations for a well-mixed estyary: application to the río maipo estuary in central chile. *J. Hydr. Res.* **43**, 339 – 350.

Monismith, S.G. 1985 Wind-forced motion in stratified lakes and their effect on mixed-layer shear. *Limnol. Oceanogr.* **30**, 771 – 783.

Nujic, M. 1995 Efficient implementation of non-oscillatory scheames for the computation of free-surface flows. *J. Hydr. Res.* **33**, 101 – 111.

Schijf, J.B. & Schonfeld, J.C. 1953 Theoretical considerations on the motion of salt and fresh water. *Proceedings Minnesota International Hydraulics Convention, Minneapolis, Minnesota.* .

Spigel, R. & Imberger, J. 1980 The classification of mixed-layer dynamics in lakes of small to medium size. *J. Phys. Oceanogr.* **10**, 1104 – 1121.

Weakly nonhydrostatic numerical scheme.[†]

Governing equations

The three hydrostatic governing equations are written as:

$$\frac{\partial U_i}{\partial t} + \frac{\partial F_i^x}{\partial x} + \frac{\partial F_i^y}{\partial y} = H_i \tag{B1}$$

where

$$U_i = [h_i, u_i h_i, v_i h_i]^T \tag{B2a}$$

$$F_i^x = \begin{pmatrix} u_i h_i \\ u_i u_i h_i \\ u_i v_i h_i \end{pmatrix} \quad , \quad F_i^y = \begin{pmatrix} v_i h_i \\ v_i u_i h_i \\ v_i v_i h_i \end{pmatrix}, \tag{B2b}$$

and

$$F_i^x = \begin{pmatrix} 0 \\ -h_i g \sum_{j=1}^{i} \epsilon_j \frac{\partial z_j}{\partial x} + \frac{\tau_i^x}{\rho_o} - \frac{\tau_{i+1}^x}{\rho_o} + f v_i h_i \\ -h_i g \sum_{j=1}^{i} \epsilon_j \frac{\partial z_j}{\partial y} + \frac{\tau_i^y}{\rho_o} - \frac{\tau_{i+1}^y}{\rho_o} - f u_i h_i \end{pmatrix}. \tag{B2c}$$

The nonhydrostatic terms in the momentum equations for each layer may be included as follows:

$$\frac{\partial \vec{u}_i h_i}{\partial t} = B_i \nabla \left(\frac{\partial}{\partial t} \left(\nabla \cdot \vec{u}_i h_i \right) \right) + A, \tag{B3}$$

where

$$B_i = \begin{cases} \frac{h_1^2}{6} & i = 1 \\ \frac{h_2^2}{3} + \frac{h_1 h_2}{2} & i = 2 \end{cases}, \tag{B4}$$

[†]Web Appendix: de la Fuente, A., Shimizu, K., Imberger, J., Niño, Y. 2008. The evolution of internal waves in a rotating, stratified, circular basin and the influence of weakly nonlinear and nonhydrostatic accelerations. *Limnol. Oceanogr.* **53**: 2738 - 2748

Nonlinear equation solver

The numerical model proposed for solving Eqs. B1 and B2a, is based on the MUSCL-Hancock method for hyperbolic equations, originally developed for 1-layer problem. The governing equations are written in the conservative form and are integrated using an irregular quadrilateral element. More details of this method may be found in (Bradford *et al.*, 1997; Loose *et al.*, 2005), and the references within these articles.

In the following, Patankar's notation (Patankar, 1980) is introduced to generalize the numerical scheme to irregular quadrilateral elements. The node under consideration is called P, and the four neighbouring cells will be called N, W, S, and E, which are generically called C. The lower letters $c = n, w, s, e$ denotes the faces between nodes P and N, W, S, and E, respectively. The area of an element, the length of the sides and normal vectors to the sides are called Ω, L_c, and $\hat{n}_c = (\hat{n}_c^x, \hat{n}_c^x)$, respectively, and the element-specific axis ξ and η are defined as the axis oriented along the WE and SN directions.

Each time step is divided into four steps: i) computation of the horizontal gradients, ii) predictor step, iii) computation of the mass and momentum fluxes, and iv) computation of the source or sink terms.

i) The horizontal gradients of each unknown primitive variables (h_i, u_i, v_i) are computed as, for example, for h_i:

$$\begin{aligned} \frac{\partial h_i}{\partial x} &= \frac{\partial h_i}{\partial \xi}\frac{\partial \xi}{\partial x} + \frac{\partial h_i}{\partial \eta}\frac{\partial \eta}{\partial x} = \frac{\overline{\Delta^\xi h_i}}{\Delta \xi}\xi_x + \frac{\overline{\Delta^\eta h_i}}{\Delta \eta}\eta_x \\ \frac{\partial h_i}{\partial y} &= \frac{\partial h_i}{\partial \xi}\frac{\partial \xi}{\partial y} + \frac{\partial h_i}{\partial \eta}\frac{\partial \eta}{\partial y} = \frac{\overline{\Delta^\xi h_i}}{\Delta \xi}\xi_y + \frac{\overline{\Delta^\eta h_i}}{\Delta \eta}\eta_y \end{aligned} \tag{B5}$$

where ξ_x, η_x, ξ_y, η_x, $\Delta\xi$ and $\Delta\eta$ are computed based on the cell geometry, and $\overline{\Delta^\xi h_i}$ and $\overline{\Delta^\eta h_i}$ are the cell average differentiation of h_i along ξ and η, respectively, computed as,

$$\overline{\Delta^\xi h_i} = SuperBee(h_{iE} - h_{iP}, h_{iP} - h_{iW}) \tag{B6}$$

$$\overline{\Delta^\eta h_i} = SuperBee(h_{iN} - h_{iP}, h_{iP} - h_{iS}) \tag{B7}$$

where $SuperBee$ denotes the SuperBee limiter function:

$$SuperBee(a,b) = \begin{cases} sign(a)\min\left(max(|a|,|b|), \beta\min\left(|a|,|b|\right)\right) & ab > 0 \\ 0 & ab < 0 \end{cases} \tag{B8}$$

The over bar refers to the cell average differentiation. The parameter β ($1 \leq \beta \leq 2$) can be used to control the numerical dissipation: $\beta \geq 1$ produces artificial steepening that counteract against numerical diffusion. Hence β was chosen as large as possible to minimize numerical dissipation.

ii) The predictor step computes the primitive variables for $t = t + \Delta t/2$ by the direct discretization of the governing equations using the horizontal gradients computed in step i). For instance, the volume conservation equation of the *ith* layer is computed in the predictor step as:

$$h_i^{t+\Delta t/2} = h_i^t - \frac{\Delta t}{2}\left(u_i^\xi \frac{\overline{\Delta^\xi h_i}}{\Delta\xi} + u_i^\eta \frac{\overline{\Delta^\eta h_i}}{\Delta\eta} + h_i^t\left(\frac{\overline{\Delta^\xi u_i}}{\Delta\xi}\xi_x + \frac{\overline{\Delta^\xi v_i}}{\Delta\xi}\xi_y + \frac{\overline{\Delta^\eta u_i}}{\Delta\eta}\eta_x + \frac{\overline{\Delta^\eta v_i}}{\Delta\eta}\eta_y\right)\right) \tag{B9}$$

where $u_i^\xi = u_i\xi_x + v_i\xi_y$ and $u_i^\eta = u_i\eta_x + v_i\eta_y$ are the flow velocities in ξ and η, respectively.

iii) Mass and momentum fluxes are computed by integrating and descritizing the governing equations, Eq. B1:

$$\frac{U_i^{t+1} - U_i^t}{\Delta t} + \frac{1}{\Omega}\sum_c \vec{F}_{i_c}^{t+\Delta t/2} \cdot \hat{n}_c L_c = H_i^{t+\Delta t/2} \tag{B10}$$

where $\vec{F}_{i_c}^{t+\Delta t/2} = (F_i^x, F_i^y)_c^{t+\Delta t/2}$ denotes the vector containing the pseudo-fluxes F_i^x and F_i^y of Eq. B2a evaluated at the side c of the computational cell by using the predicted variables in step ii). Note that hereafter the superindex $t + \Delta t/2$ in $\vec{F}_{i_c}^{t+\Delta t/2}$ is dropped for simplifying the notation. Before computing Eq. B10, the primitive variables are interpolated from the nodes P and C to the faces c, such as, for example for h_i

$$\begin{aligned} h_{i_e} &= h_{i_P} + 0.5\overline{\Delta^\xi h_i} \\ h_{i_w} &= h_{i_P} - 0.5\overline{\Delta^\xi h_i} \\ h_{i_n} &= h_{i_P} + 0.5\overline{\Delta^\eta h_i} \\ h_{i_s} &= h_{i_P} - 0.5\overline{\Delta^\eta h_i} \end{aligned} \tag{B11}$$

By applying the same interpolation to all the computational cells, two interpolated values of U and F are obtained at one generic cell face c: the interpolation was made from P to c (C to c) is called internal (external) interpolation. Finally, to compute $\vec{F}_{i_c}$, the Nujic's simplification was adopted (Nujic, 1995), which calculate the perpendicular λ_i to the faces as

$$\lambda_i = |\hat{u}_{i_{\perp c}}| + \sqrt{\frac{\hat{P}_i^{top}}{\rho_o} + \frac{\rho_i}{\rho_o} g\hat{h}_i} \tag{B12}$$

where

$$|\hat{u}_{i_{\perp c}}| = abs\left(\hat{u}_{i_c}\hat{n}_c^x + \hat{v}_{i_c}\hat{n}_c^y\right), \tag{B13}$$

and

$$\begin{aligned}
\hat{h}_i &= \sqrt{h_i^{int} h_i^{ext}} \\
\hat{u}_i &= \frac{u_i^{int}\sqrt{h_i^{int}} + u_i^{ext}\sqrt{h_i^{ext}}}{h_i^{int} + h_i^{ext}} \\
\hat{v}_i &= \frac{v_i^{int}\sqrt{h_i^{int}} + v_i^{ext}\sqrt{h_i^{ext}}}{h_i^{int} + h_i^{ext}}
\end{aligned} \tag{B14}$$

The stability criteria impose a time step Δt to be smaller than the time a surface wave travels the distance between P and the faces c.

iv) The horizontal gradient of pressure in the vector H_i are computed as,

$$\begin{aligned}
gh_1\frac{\partial z_1}{\partial x} &\approx gh_1\frac{1}{\Omega}\sum_c z_{1_c}\hat{n}_c^x L_c \\
gh_1\frac{\partial z_1}{\partial y} &\approx gh_1\frac{1}{\Omega}\sum_c z_{1_c}\hat{n}_c^y L_c
\end{aligned} \tag{B15}$$

for the upper layer, and

$$\begin{aligned}
gh_2\left(\frac{\partial z_1}{\partial x} + \epsilon_2\frac{\partial z_2}{\partial x}\right) &\approx gh_2\frac{1}{\Omega}\sum_c \left(z_{1_c} + \epsilon_2 z_{2_c}\right)\hat{n}_c^x L_c \\
gh_2\left(\frac{\partial z_1}{\partial y} + \epsilon_2\frac{\partial z_2}{\partial y}\right) &\approx gh_2\frac{1}{\Omega}\sum_c \left(z_{1_c} + \epsilon_2 z_{2_c}\right)\hat{n}_c^y L_c
\end{aligned} \tag{B16}$$

for the second layer, and $z_{1_c} = \hat{h}_{1_c} + \hat{h}_{2_c}$ and $z_{2_c} = \hat{h}_{2_c}$ for flat basins. The Coriolis term and the shear stresses are directly evaluated with the flow velocities at $t = t + \Delta t/2$.

Nonhydrostatic term

Rearranging the nonhydrostatic terms, Eq. B3 may be expressed as

$$\begin{aligned}\frac{\partial u_i h_i}{\partial t} &= B_i \nabla_H \cdot \left(\frac{\partial^2 \vec{u}_i h_i}{\partial x \partial t} \right) + A_i^x \\ \frac{\partial v_i h_i}{\partial t} &= B_i \nabla_H \cdot \left(\frac{\partial^2 \vec{u}_i h_i}{\partial y \partial t} \right) + A_i^y\end{aligned} \tag{B17}$$

where ∇_H is the horizontal gradient operator. By integrating Eq. B17 over a computational cell, it is reduces to:

$$\begin{aligned}a_i^x &= \frac{B_i}{\Omega} \sum_c \frac{\partial}{\partial x} \left(a_i^x \hat{n}_i^x + a_i^x \hat{n}_i^y \right)_c L_c + A_i^x \\ a_i^y &= \frac{B_i}{\Omega} \sum_c \frac{\partial}{\partial y} \left(a_i^y \hat{n}_i^x + a_i^y \hat{n}_i^y \right)_c L_c + A_i^y,\end{aligned} \tag{B18}$$

where $a_i^x = \frac{\partial u_i h_i}{\partial t}$ and $a_i^y = \frac{\partial v_i h_i}{\partial t}$. The rotated axis at the face c are defined such that ξ_c point to the neighbouring node C, and η_c is taken anticlockwise perpendicular to ξ_c. Therefore, the discretized horizontal derivatives in x and y directions becomes, for example for x:

$$\frac{\partial}{\partial x} \left(a_i^x \hat{n}_i^x + a_i^x \hat{n}_i^y \right)_c = \frac{\Delta^\xi \left(a_i^x \hat{n}_i^x + a_i^x \hat{n}_i^y \right)}{\Delta \xi_c} \frac{\partial \xi_c}{\partial x} + \frac{\Delta^\eta \left(a_i^y \hat{n}_i^x + a_i^y \hat{n}_i^y \right)}{\Delta \eta_c} \frac{\partial \xi_c}{\partial x} \tag{B19}$$

Δ^ξ and Δ^η denote the discrete differentiation of $(a_i^x \hat{n}_i^x + a_i^y \hat{n}_i^y)$ in ξ_c and η_c, respectively (note that they are different from $\overline{\Delta^\xi}$ and $\overline{\Delta^\eta}$, which are computed by the *SuperBee* function (Eqs. B6-B8). They are computed by direct discritization as, for example for Δ^ξ:

$$\Delta^\xi \left(a_i^x \hat{n}_i^x + a_i^x \hat{n}_i^y \right) = \left(a_i^x \hat{n}_i^x + a_i^x \hat{n}_i^y \right)_C - \left(a_i^x \hat{n}_i^x + a_i^x \hat{n}_i^y \right)_P \tag{B20}$$

and Δ^η is done by using the values at the vertex that defines the cell. For example, at the face e, these vertex are called se and ne, and $(a^x \hat{n}_c^x + a^y \hat{n}_c^y)_{se}$ is computed as the mean algebraic value among the nodes that share the vertex, for example nodes P, E, S and NE for the value at se. Finally, Eq. B17 is reduces to the matrix form to be solved for $a = \left(\frac{\partial u_1 h_1}{\partial t}, \frac{\partial u_2 h_2}{\partial t}, \frac{\partial v_1 h_1}{\partial t}, \frac{\partial v_2 h_2}{\partial t} \right)^T$

$$(I - M)\, a = A \tag{B21}$$

where I is the identity matrix, and M includes the discretized terms multipled to a^x and a^y in Eq. B18, and $A = (A_1^x, A_2^x, A_1^y, A_2^y)^T$. More details of the treatment of this kind of equation for non-regular grids are discussed in chapter 8 of Ferziger & Peric (2002).

References

Bradford, S., Katopodes, N. & Parker, G. 1997 Characteristic analysis of turbid underflows. *J. Hydr. Eng.* **123**, 420 – 431.

Ferziger, J.H. & Peric, M. 2002 *Computational Methods for Fluid Dynamics.*. Springer.

Loose, B., Niño, Y. & Escauriaza, C. 2005 Finite volume modeling of variable density shallow-water equations for a well-mixed estyary: application to the río maipo estuary in central chile. *J. Hydr. Res.* **43**, 339 – 350.

Nujic, M. 1995 Efficient implementation of non-oscillatory scheames for the computation of free-surface flows. *J. Hydr. Res.* **33**, 101 – 111.

Patankar, S. 1980 *Numerical Heath Transfer and Fluid Flow.*. Hemisphere Publishing Corporation.